NASA CONTRACTOR REPORT

NASA CR-907

NASA CR-907

PERFORMANCE OF MULTILAYER INSULATION SYSTEMS FOR TEMPERATURES TO 700° K

by George R. Cunnington, Jr., Carl A. Zierman, Arnold I. Funai, and Alfred Lindahn

Prepared by
LOCKHEED AIRCRAFT CORPORATION
Palo Alto, Calif.
for Ames Research Center

NATIONAL AERONAUTICS AND SPACE ADMINISTRATION • WASHINGTON, D. C. • OCTOBER 1967

NASA CR-907

PERFORMANCE OF MULTILAYER INSULATION SYSTEMS FOR TEMPERATURES TO 700° K

By George R. Cunnington, Jr., Carl A. Zierman,
Arnold I. Funai, and Alfred Lindahn

Prepared under Contract No. NAS 2-2441 by
LOCKHEED AIRCRAFT CORPORATION
Palo Alto, Calif.

for Ames Research Center

NATIONAL AERONAUTICS AND SPACE ADMINISTRATION

For sale by the Clearinghouse for Federal Scientific and Technical Information
Springfield, Virginia 22151 – CFSTI price $3.00

FOREWORD

This document was prepared by the Thermophysics section of the Aerospace Sciences Laboratory, Lockheed Palo Alto Research Laboratory, Lockheed Missiles & Space Company, for the Ames Research Center of the National Aeronautics and Space Administration as the final report of the research activities carried out under Contract NAS 2-2441, from October 1964 through May 1967.

CONTENTS

ILLUSTRATIONS

Figure Page

TABLES

Section 1

SUMMARY

Multilayer insulations which will operate in the 300° to 700°K temperature range are being considered for use as portions of the thermal control systems on advanced spacecraft for near-solar missions. The high operating temperatures necessitated the evaluation of new materials and composites. Also, as this type of insulation has highly anisotropic thermal properties, the multidimensional heat transfer properties of the materials must be characterized.

An analytical treatment is derived for evaluating the one-dimensional heat transfer through multilayer insulations. Experimental verification of the influence of the significant properties of the components of the system on overall thermal conductivity is reported. Data on the thermal conductivity of a number of multilayer insulations over the temperature range of 300° to 700°K are presented. Analytical models are developed for study of the effects of exposed edges, joints, and penetrations on the heat transfer in this type of insulation and comparison is made with experimental data for a cylindrical system.

Section 2

INTRODUCTION

A prime consideration in the temperature control of spacecraft is the use of highly efficient thermal insulations. As an example, spacecraft on a near-solar mission such as 0.2 to 0.1 AU will utilize low α_s/ϵ coatings in conjunction with insulation to achieve proper temperature control of the vehicle. Equilibrium surface temperatures for two typical geometries in spacecraft configurations versus AU values from 0.1 to 1.0 and for solar absorptance to infrared emittance (α_s/ϵ) ratios from 0.05 to 0.20 are shown in Figure 1. Temperature ranges from approximately 200° to 850°K for the flat surface and 150° to 600°K for the spinning surface. A review of the status of spacecraft thermal control technology (ref. 1) shows that the lowest value of α_s/ϵ currently available in a stable coating is 0.06. This dictates an insulation suitable for use in the 300° to 700°K range. Even with active thermal control systems, as illustrated in Figure 2, considerations of solar and internal component thermal loads require the use on some portions of the vehicle of an insulation having a thermal conductivity on the order of 1×10^{-5} W/cm °K. The only practical type of insulation which meets this thermal requirement is the multilayer construction.

The significant advances in thermal insulation for cryogenic containers or normal spacecraft electronic subsystem packages are attributed to multilayer insulation technology as described in refs. 2 and 3. However, relatively few data and little practical experience have been reported for insulations in the temperature range from 400° to 700°K. Multilayer insulations have been made up of a vacuum-deposited, aluminum-coated polyester film or thin aluminum foil radiation shields separated by a variety of spacer materials. These materials are used to maintain an effective separation between shields without adding a significant heat transport path to the system. Polyester film, however, does not withstand a temperature environment above 425°K while the aluminum foil increases both the insulation weight and the multidimensional heat-transfer problems.

In addition to the thermal conductivity and density considerations, the insulation must exhibit minimum anisotropic thermal characteristics for specific applications. In areas where penetrations, attachments, or joints are prevalent for functional or structural purposes, a minimum value of conductance in the direction parallel to the layers is desired to reduce heat transfer along the insulation layers. As an example, energy incident upon the edges of the openings in the instrument section insulation blanket, shown in Figure 2, is transferred along the inner layers into the vehicle interior by both direct radiation from the inner layer and radiation from the insulation edge. This results in a degradation of at least one order of magnitude in the thermal performance of the insulation.

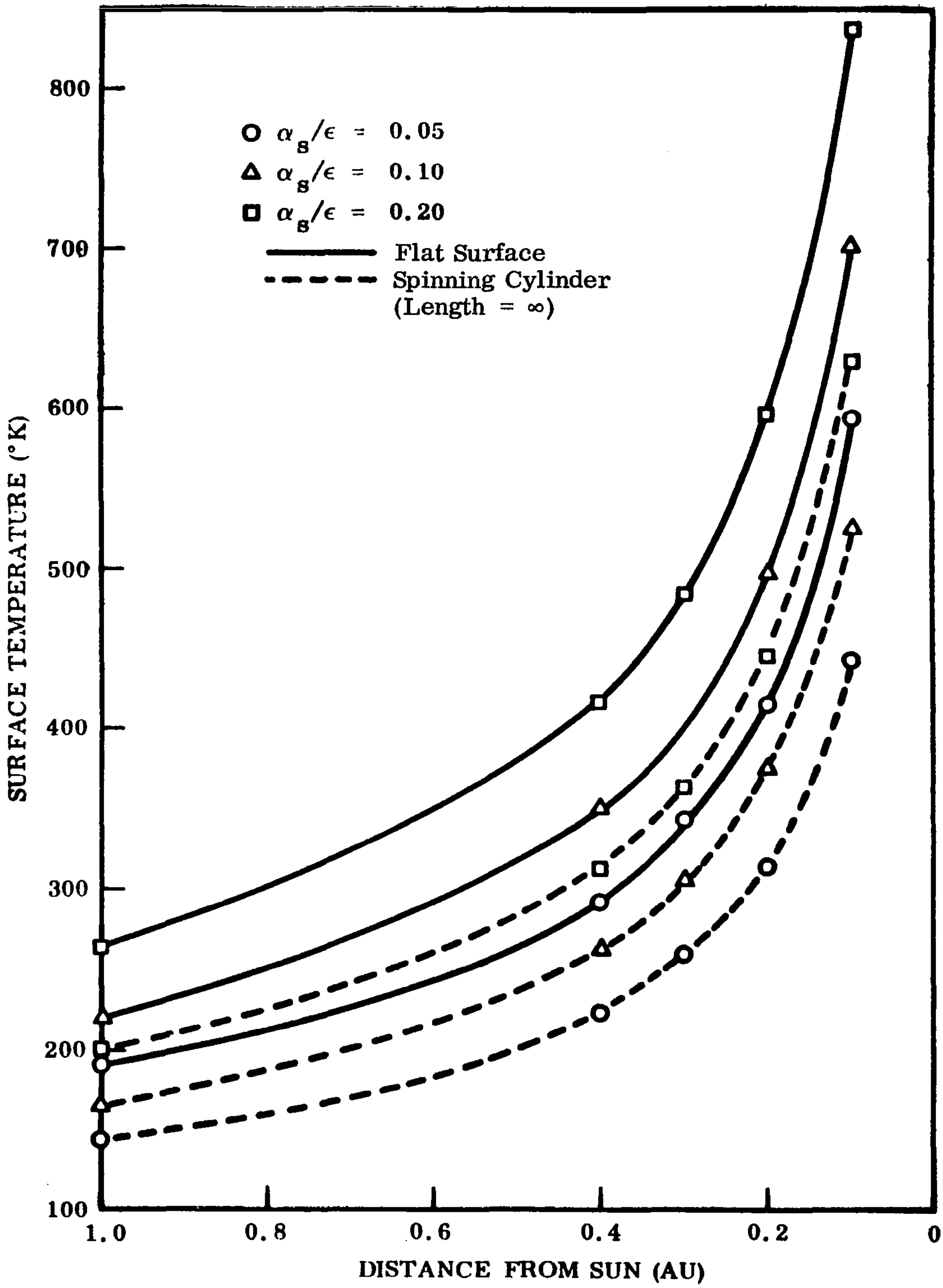

Figure 1 Equilibrium Surface Temperature of Flat and Spinning Cylindrical Surfaces as a Function of AU and α_S/ϵ Ratio

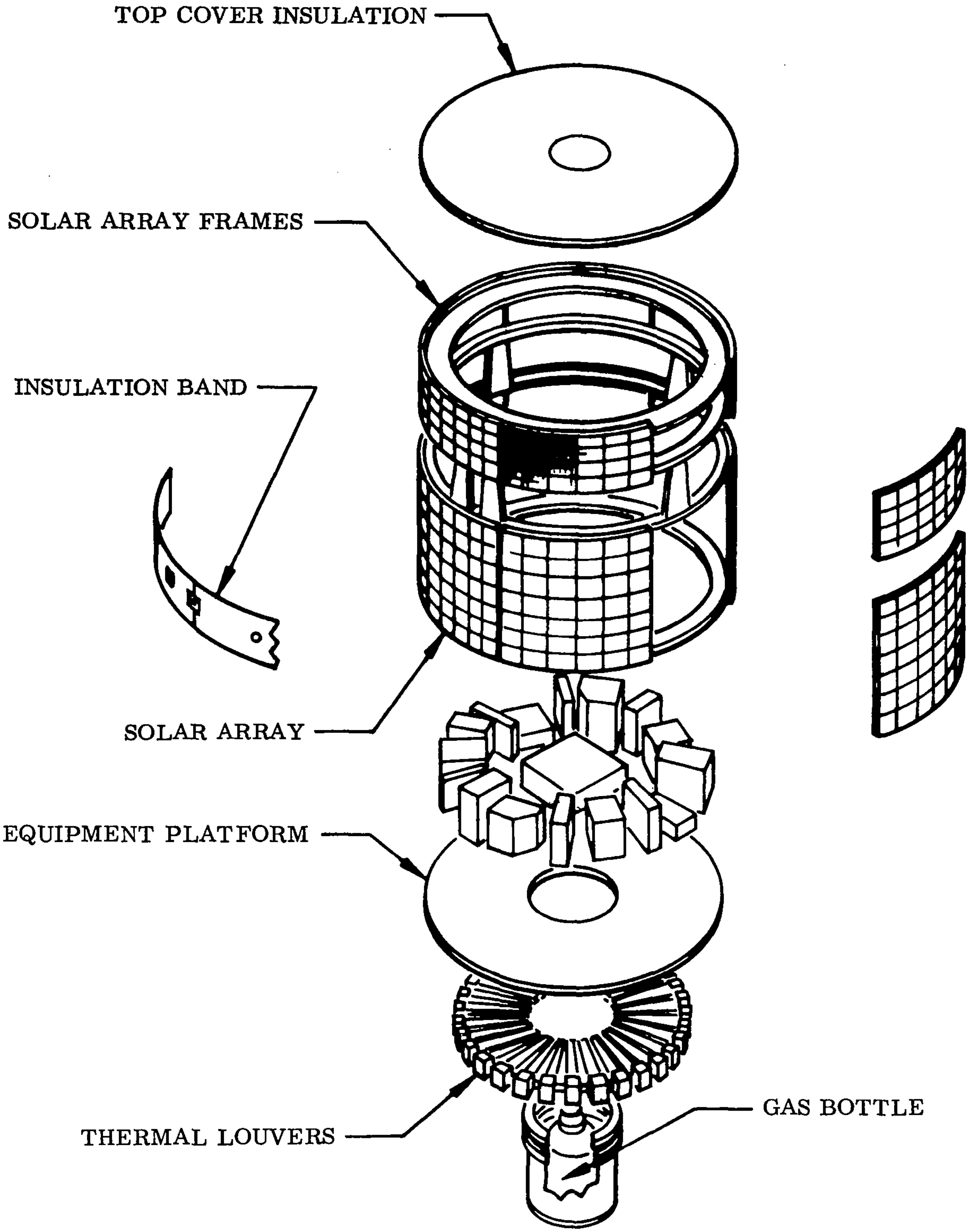

Figure 2 Typical Spacecraft Thermal Control Components

The intent of this study is to provide design data on low thermal conductivity insulations suitable for the elevated temperature and vacuum environment, and analytical predictions of the effects of multidimensional heat transfer on the overall thermal performance of the system. A brief analysis of the one-dimensional heat transfer in multilayer systems is presented together with data on the properties and thermal performance of a number of insulations. Three analytical models are described for studying the multidimensional heat transfer in anisotropic insulations. These are for slab, disc, and cylindrical configurations. Results of parametric studies of the effects of penetrations, exposed edges, and joints on the overall insulation performance are reported, and comparisons are made between the analysis and experimental data for a cylindrical system.

Section 3
NOMENCLATURE

Å	Angstrom
A	area
a	absorption cross section
C	constant
D	fiber diameter
E	modulus of elasticity
ΔH	latent heat of vaporization
I	current
k	thermal conductivity
L	cell dimension
ℓ	length
N	number of radiation shields
$\bar{n}$	index of refraction
n	exponent
P	power
Q	heat input
q	heat flux
s	scattering cross section
R	radius or electrical resistance
t'	total true thickness of spacer
t	thickness of insulation

T	absolute temperature
V	voltage
$\dot{v}$	volume flow rate
x	intermediary length
X	distance
α_s	solar absorptance
α	accommodation coefficient
β_o	material constant
δ	solid fraction
ϵ_T	total hemispherical emittance
μ	Poisson's ratio or micron
λ	mean free path
ρ	density
σ	Stefan-Boltzmann constant
σ_o	material constant
τ	transmittance

Superscripts:

$*$	denotes two-dimensional effect distance

Subscripts:

C	cold
c	calorimeter
e	effective
g	gas
m	mean

s	solid
H	hot
P	penetration
$\parallel$	parallel
$\perp$	normal
1D	one dimensional

Section 4

ANALYTICAL STUDIES

A major consideration in the development of elevated temperature multilayer insulation design data is the evaluation of the heat-transfer parameters which govern the performance of this type of system. These are the thermophysical properties of the components, and the physical arrangement of the components to form the insulation system. For the initial phase, an analytical model was prepared to study the influence of the thermal and optical properties of shield and spacer materials upon the thermal conductivity of multilayer insulations. This provides the basic information necessary for insulation optimization for conditions of one-dimensional heat transfer. For a number of applications, however, multidimensional effects must be considered because of the anisotropic thermal properties of multilayer insulations, i.e., thermal conductivity parallel to the layers two to three orders of magnitude greater than that normal to the layers. Three analytical models were formulated to study the degradation in thermal performance caused by the multidimensional heat transfer resulting from exposed edges and discontinuities in the form of joints or penetrations in the insulation blanket.

4.1 ONE-DIMENSIONAL HEAT TRANSFER

Heat transfer in multilayer insulations is in the general case by conduction, convection, and radiation. For space applications, the convection mechanism may be neglected as the gas phase is at a greatly reduced pressure. The heat-transport processes which are to be considered are conduction through the solid and gaseous phases of the insulation and radiation. The radiation becomes the dominant mechanism as temperature increases, whereas conduction determines the lower limit of thermal conductivity if radiative transport is effectively suppressed.

Rigorous treatment of the heat-transfer problem in insulations is very complex. The interactions between mechanisms of radiation and conduction must be considered because of the perturbation of the temperature gradient due to the presence of a scattering and absorbing medium. However, for multilayer insulation having a very small separation between radiation shields, an approximate model may be developed by treating the mechanisms independently. The total heat transfer through such a system then is expressed as the summation of the heat transferred by the individual mechanisms.

$$q_{\text{total}} = q_{\text{radiation}} + q_{\text{gas conduction}} + q_{\text{solid conduction}} \tag{1}$$

Evaluation of the individual heat fluxes serves to illustrate the importance of the mechanisms and how they may be reduced to result in an optimum system.

4.1.1 Gaseous Conduction

From considerations of kinetic theory, the thermal conductivity of a gas is a function of density and the mean free path of the gas molecules.

$$K_g \propto \rho C_v \lambda \tag{2}$$

Over a wide pressure range, the thermal conductivity of a free or unrestricted gas is nearly independent of pressure as the changes in density are negated by the increase in mean free path. However, for a restricted gas, as is the case for that contained within the void structure of a multilayer system, reduction in pressure results in the characteristic dimension of the cell or void space becoming much smaller than the gas mean free path. Consequently, thermal conductivity decreases in proportion to pressure as the effective path length, λ, is now that of the cell rather than the mean free path of the gas. Although conduction through the gas phase is small in evacuated systems composed of micron-size fibers, it should be examined as together with solid phase conduction it represents the lower limit of effective thermal conductivity if radiation transfer is eliminated.

From probability considerations, Verschoor (ref. 4) arrived at a mean free path for the contained gas as

$$\lambda' = \lambda \left(\frac{L_s}{L_s + \lambda} \right) \tag{3}$$

and the effective thermal conductivity of the restricted gas phase is

$$k_g = \alpha k_g^* \left(\frac{L_s}{L_s + \lambda} \right) \tag{4}$$

The accommodation coefficient, α, which is the ratio of the actual-to-equilibrium energy transfer is assumed to be 1 for this case. This occurs when the impinging gas molecules are absorbed on the surface and then reevaporated at the temperature of the surface. The same effect is obtained on a very rough surface where most of the molecules would hit the surface a number of times before escaping.

Using simplifying assumptions for fibers (ref. 4), the path length for molecule-to fiber collision is

$$L_s = 0.785 \frac{D_f}{(1 - \delta)} \tag{5}$$

Considering the interstitial gas as air at a pressure of 10^{-4} Torr, the effective gas phase thermal conductivity for a multilayer system using a micron-size fiber spacer material is 2×10^{-8} W/cm °K. Similarly for a system composed only of radiation shields (i.e., no continuous spacer layers) at a layer density of 40 layers/cm, the gas conductivity is approximately 1×10^{-7} W/cm °K. As this conductivity term is at least one order of magnitude less than typical system overall conductivities, gaseous conduction was considered negligible for the present analysis.

4.1.2 Solid Conduction

Heat conduction through the solid phase of fibrous and particulate systems has been shown by several investigators (refs. 5, 6, 7) to be a function of the thermal conductivity and mechanical properties of the fibers, the unit load on each fiber contact, the number of fibers, packing geometry, and the temperature difference per unit thickness. Wang (ref. 5) developed an expression for a specific packing geometry which illustrates the effect of the individual fiber mat parameters.

$$q_s = \frac{16}{\pi} (1 - \delta^2) k_s \left[\frac{1}{\ln\left(\frac{8\pi R^2}{Ac}\right) + \frac{\pi}{2(1 - \delta)}} \right] \frac{\Delta T}{\Delta X} \tag{6}$$

where

$$Ac = \frac{\pi}{4} R^2 \left[\frac{(1 - \mu^2)}{E(1 - \delta)^2} \times 3\pi^2 C \right]^{2/3}$$

The random orientation of the fibers, local variations in compression and loading, and the thermal resistance at each contact point or area (which is probably the controlling resistance for the mechanism) make a solution for solid phase conduction unrealistic for most fiber systems. However, a conductivity attributed to the solid phase may be semiempirically expressed in terms of a density, thermal conductivity of the solid material, and fiber diameter as

$$k_s \propto C(1 - \delta) K_s D_f^n \tag{7}$$

Evaluation of this heat-transport mechanism is accomplished by reduction of the experimental data to the form of a constant times the product of bulk density and specimen mean temperature.

4.1.3 Radiation Conduction

Numerous treatments of radiation transfer through powders and fibers have appeared in the literature (refs. 8, 9, 10, 11). Combination of the equations to include scattering and absorption and multiple reflective shields results in the following equation by Glaser et al. (ref. 12).

$$q_{\text{radiation}} = \frac{\bar{n}^2 \sigma \left(T_H^4 - T_C^4\right) At}{(a + 2s)\, \frac{t'}{2} + (N - 1)\left(\frac{2}{\epsilon} - 1\right)} \tag{8}$$

Equation (8) shows the importance of the optical properties of both spacer and shield materials, the number of shields, and the boundary temperatures.

For a multilayer system with nonabsorbing and nonscattering spacers, the radiant conductivity function becomes

$$K_r = \frac{\sigma \left(T_H^2 + T_C^2\right)(T_H + T_C)t}{(N - 1)\left(\frac{2}{\epsilon} - 1\right)} \tag{9}$$

Similarly, for a multilayer system with spacer layers having an appreciable optical density the conductivity is approximated by

$$K_r = \frac{\bar{n}^2 \sigma \left(T_H^2 + T_C^2\right)(T_H + T_C)t}{(a + 2s)\, \frac{t'}{2} + (N - 1)\left(\frac{2}{\epsilon} - 1\right)} \tag{10}$$

The latter form is also applicable to insulations without multiple radiation shield; in which case $(N - 1)(2/\epsilon - 1)$ represents the properties of the insulation boundaries.

4.1.4 Analytical Model

The theoretical treatments of Viskanta (ref. 13) and Folweiler (ref. 14) provide the most exact solutions of heat transfer considering simultaneous solid conduction and radiation. The equations are very complex, however, and the uncertainties in the optical and thermal properties of the component materials do not justify the use of the more rigorous form. Therefore, a relatively simple approximate solution is used which combines the separate mechanisms in the following manner:

$$k_e = C(1 - \delta)k_s D_f^n + \frac{\bar{n}^2 \sigma \left(T_H^2 + T_C^2\right)(T_H + T_C)t}{(a + 2s)\frac{t}{2} + (N - 1)\left(\frac{2}{\epsilon} - 1\right)} \qquad (11)$$

Figure 3 illustrates the importance of several of the heat-transfer parameters on the thermal conductivity of a multilayer insulation.

4.2 MULTIDIMENSIONAL HEAT TRANSFER

Three computer programs were developed for the study of multidimensional heat transfer of highly anisotropic multilayer insulation systems. The three models are a slab, a disc, and a cylinder. The slab model is used to analyze a plane surface of unit width. The radial model is employed to study a 1-rad segment of a plane surface with axisymmetric heat transfer about the centerline. The cylindrical model is for the analysis of insulation systems in the form of a hollow cylinder, and it includes the three-dimension effects encountered with the presence of both penetrations and exposed edges. The symmetry of the first two models limits their analysis to two-dimensional heat transfer, which is utilized for evaluating the influence of a single perturbation such as a penetration.

The computer programs were written in THERMOTRAN language which is a Lockheed Missiles & Space Company proprietary development. THERMOTRAN is a thermodynamics-procedure-oriented programming language for the description and solution of problems in steady state and transient heat transfer. The models were derived specifically to provide the thermal analyst with a tool to study the heat leaks through multilayer insulations resulting from penetrations such as longitudinal struts, circular observation ports, booms and apertures, joints in the insulation, and the edges of the system. All studies for this analysis were carried out only for the case of steady state heat transfer. This was based upon the proposed use of the insulation systems on a spacecraft exposed to quasi-equilibrium thermal conditions. Since multilayer systems are anisotropic with regard to thermal conductivity, the models can accept different values for conductivity in the two principal directions. Also, a different value of thermal conductivity may be used for the intermediary insulation, which for this study is assumed to be isotropic.

4.2.1 Slab and Radial Models

The basic nodal network and node numbering system for the slab and radial models are similar. Therefore, a complete description of the radial model is given with references to the slab model only when differences occur. The network and numbering system for the radial model are shown in Figure 4. The network consists of a 1-rad segment (unit width for slab) with an array of 40 nodal volumes, with 8 columns along the radius, each 5 nodes deep. The two columns of nodes at the left edge are used to simulate the intermediary insulation, and the remaining nodes to simulate the multilayer insulation. When an intermediary is not used, all nodes represent the multilayer insulation. Row widths and thicknesses may differ, although the thicknesses of adjacent nodes within the same row are similar.

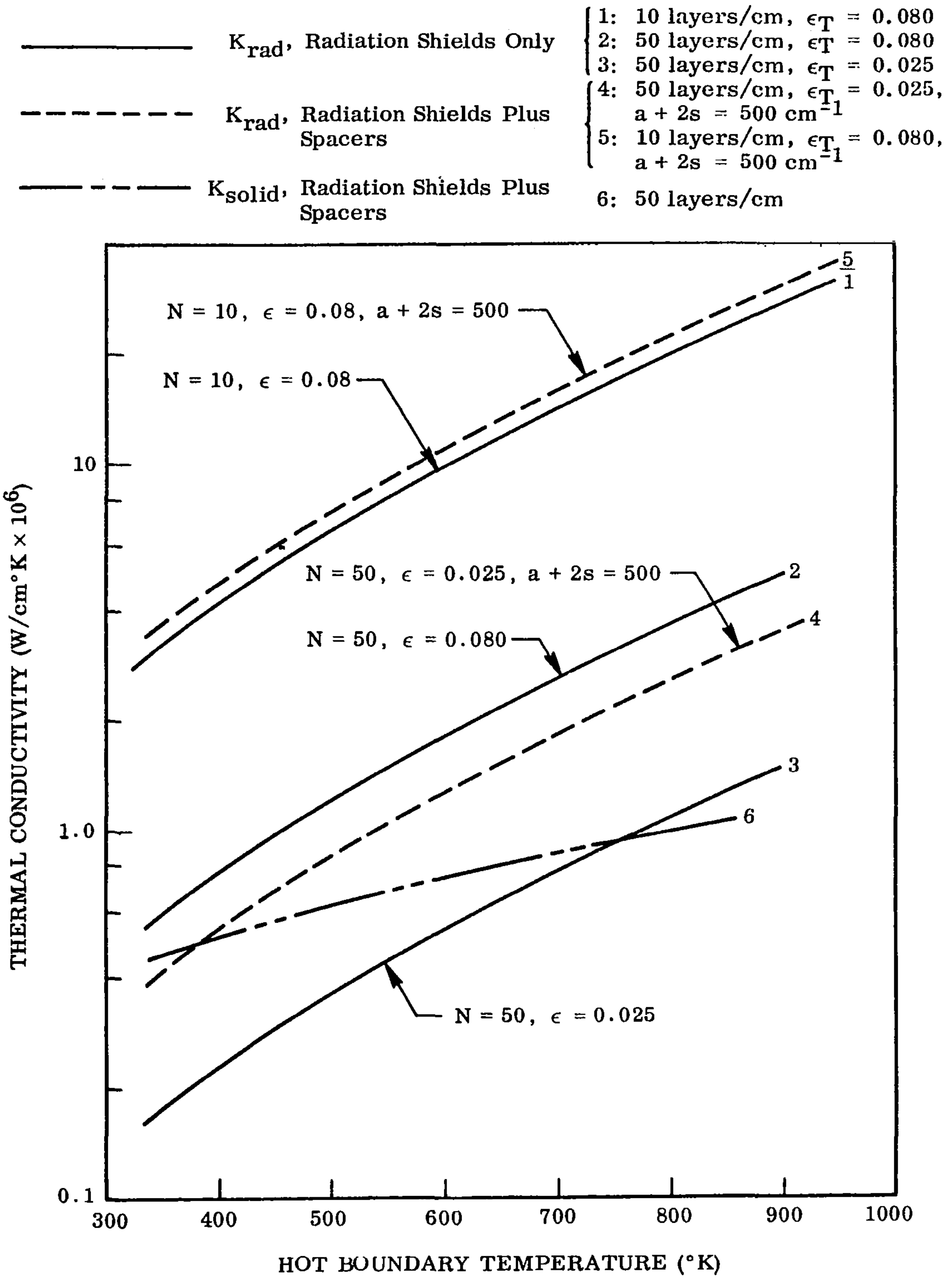

Figure 3 Effects of Thermal Properties of Shields and Spacers on Radiation and Solid Conductivities

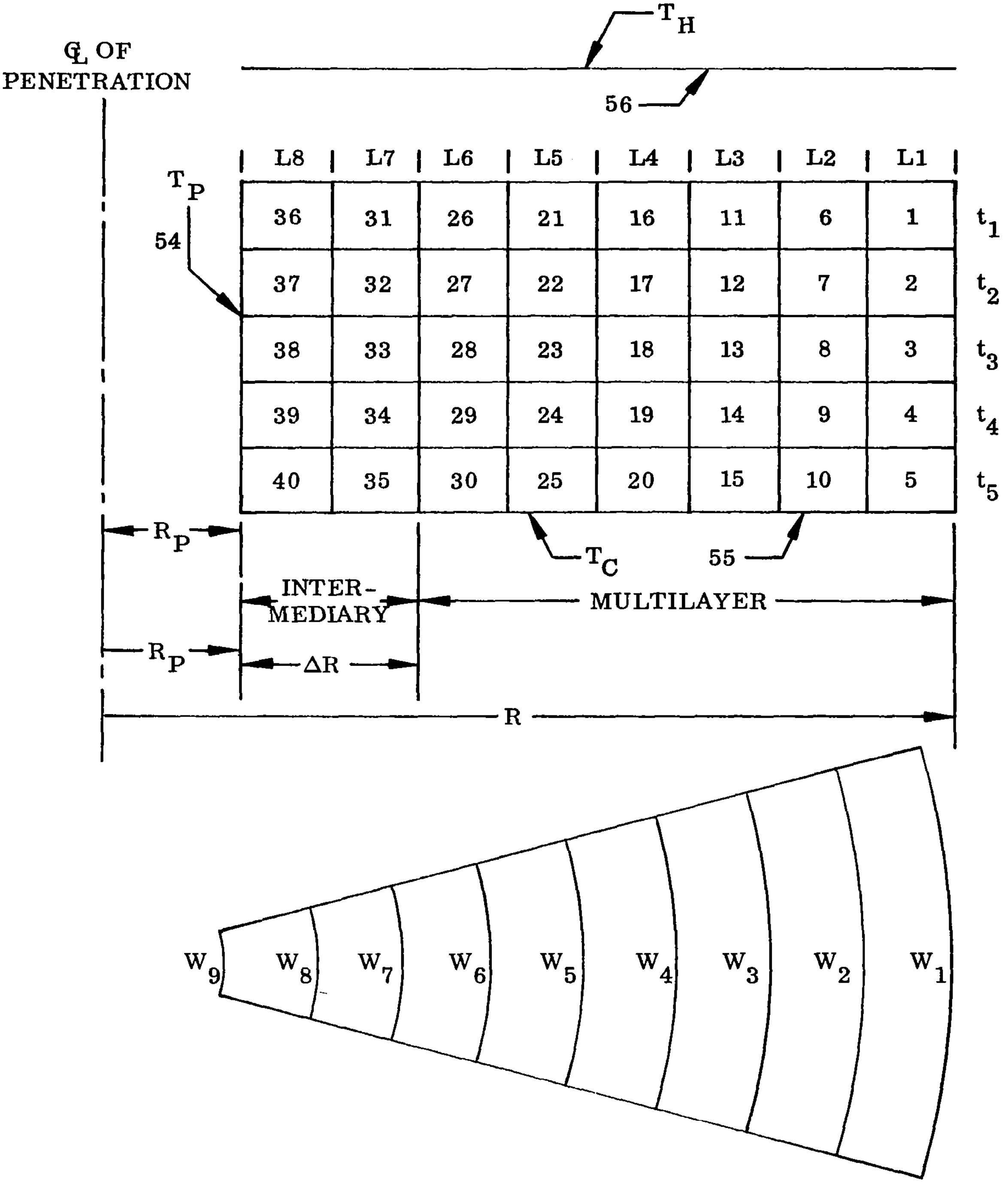

Figure 4 Basic Nodal Network and Nomenclature, Radial Model

Along the radius of the penetration, R_p, a uniform sink or source temperature is provided (left-edge boundary for slab). Energy exchange between this sink or source and the intermediary insulation can occur by either thermal radiation or conduction. The top and bottom surfaces of the radial insulation segment are maintained at uniform temperatures for heat source and sink, respectively. The right-hand boundary of the multilayer insulation is adiabatic, and the radius defining this boundary is chosen to be sufficiently large to satisfy this condition.

Figure 5 shows the thermal network with resistor assignments and dummy nodal points. In addition, a parallel thermal network is depicted which consists of one row of five nodes and represents the one-dimensional heat flow condition computed for each problem. The sink-source conditions on opposite sides of the insulation, as used in the two-dimensional array, are also applied here.

For the radial model the resulting temperature profile is used to define the radius location where the two-dimensional temperature profile attains a fixed percentage of the one-dimensional profile. The numerical value of the percentage approach criteria for temperature is supplied as an input to the computer. The output is the effective radius, as depicted in Figure 6, and the net heat flow to the sink within this effective radius. For the two-dimensional problem using the slab model, the ratio of local heat flow to that of heat flow for the one-dimensional case is determined as a function of length. When this ratio approaches within 2% of one-dimensional heat flow, the effective length is determined and the net heat flow up to that length calculated. Figure 7 illustrates the computation of the effective length for this heat-flow ratio criterion.

The input parameters and selection of range of parameters for the slab and radial models studies are as follows:

• $K_{\parallel}$	thermal conductivity parallel to alternate layers; 1.7×10^{-4}, 1.7×10^{-3}, 1.7×10^{-2} W/cm °K
• $K_{\perp}$	thermal conductivity perpendicular to alternate layers; 8.7×10^{-6}, 1.7×10^{-5}, 3.5×10^{-5} W/cm °K
• K_{IN}	thermal conductivity of the intermediary insulation; 6.9×10^{-5} W/cm °K
• ϵ_P	emittance of penetration wall or strut: 0.01, 0.1, 0.5, 1.0
• T_H	temperature of the hot boundary of insulation; 475°K, 590°K, 700°K
• x, ΔR	width of the intermediary insulation; 0 to 5 cm
• R_P	radius of penetration (radial model only); 0.15 to 2.54 cm
• T_C	temperature of cold boundary of insulation (insulated surface); 295°K

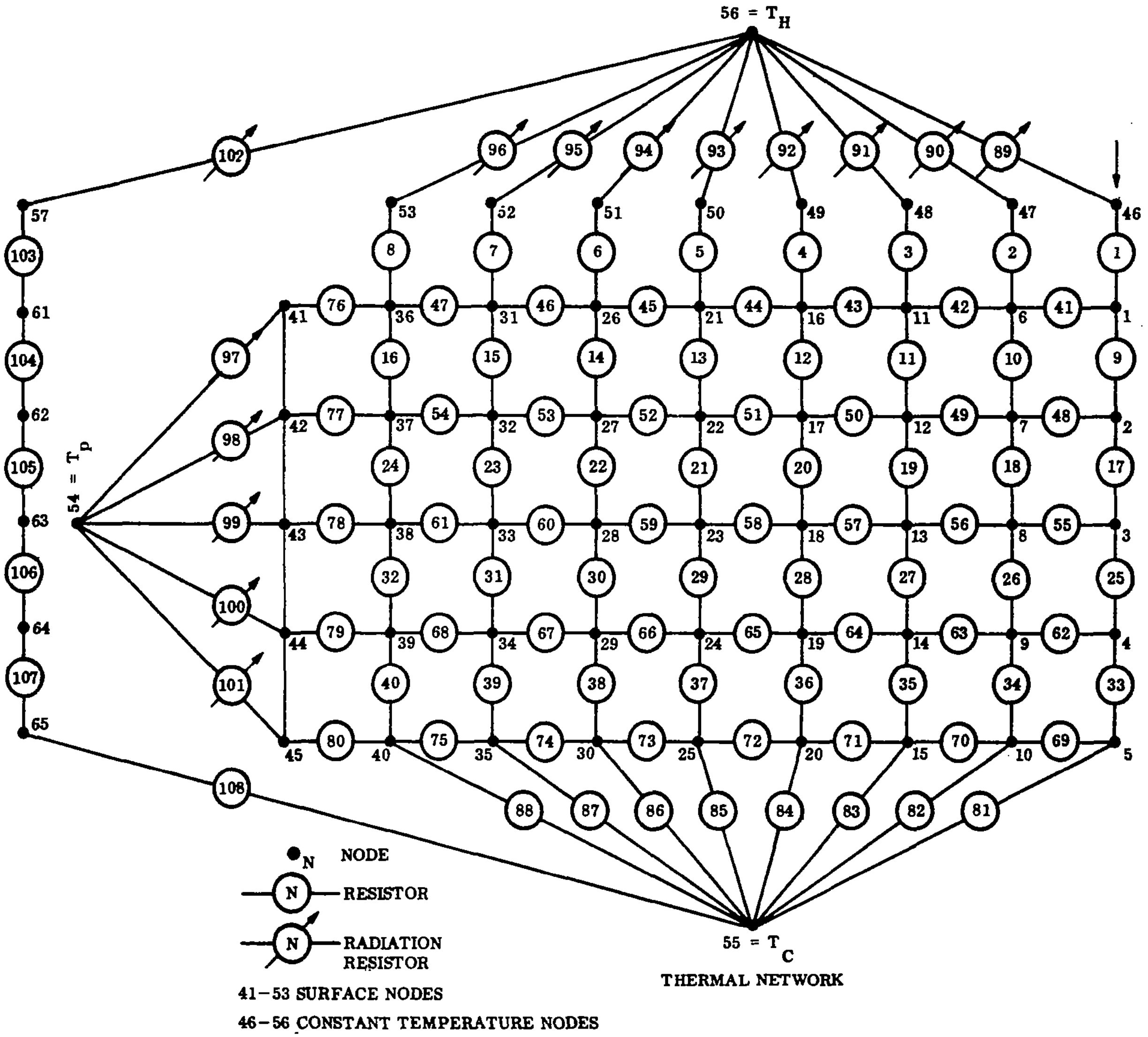

Figure 5 Thermal Network, Showing Resistor Assignments

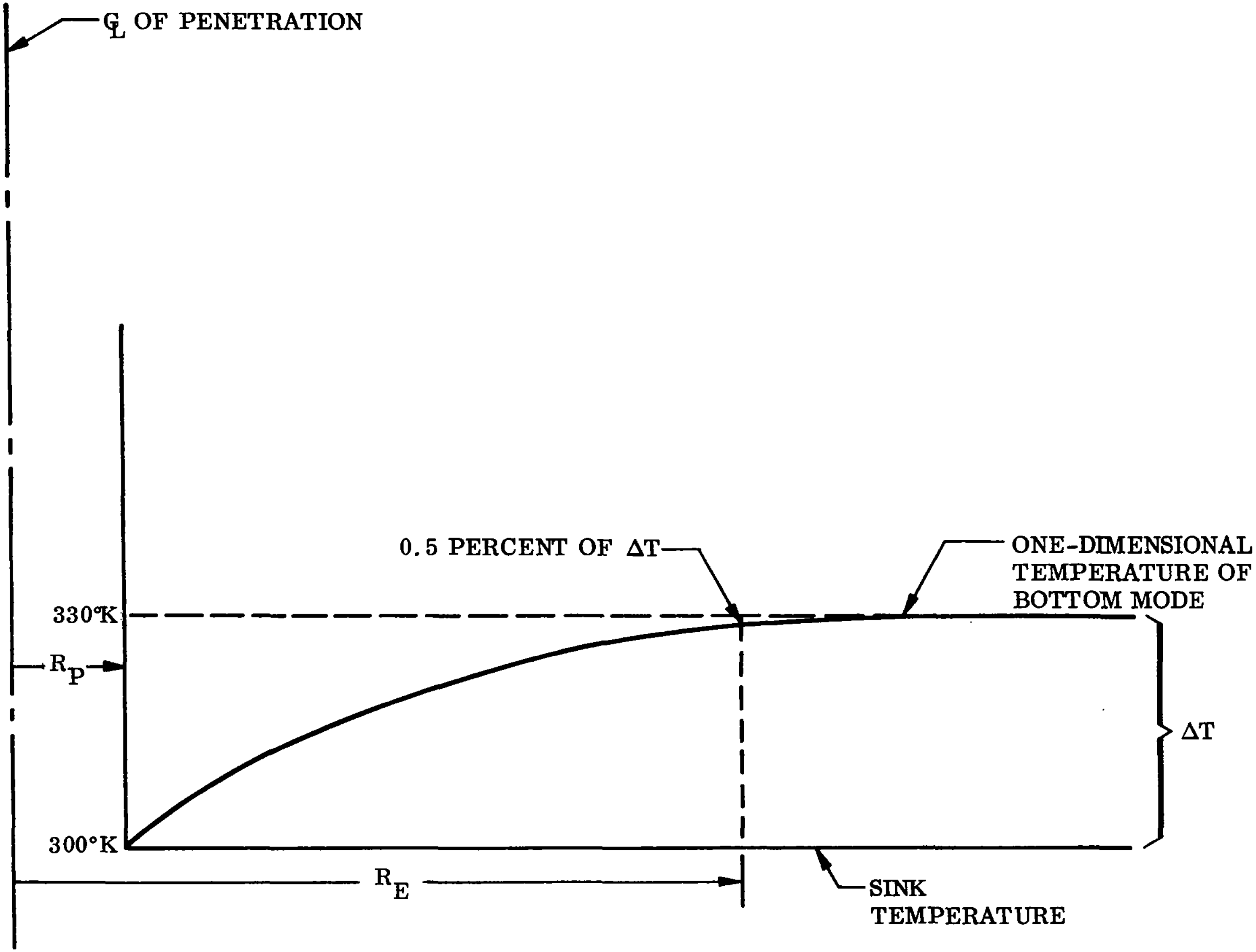

Figure 6 Temperature Profile in Bottom Nodes of Sector

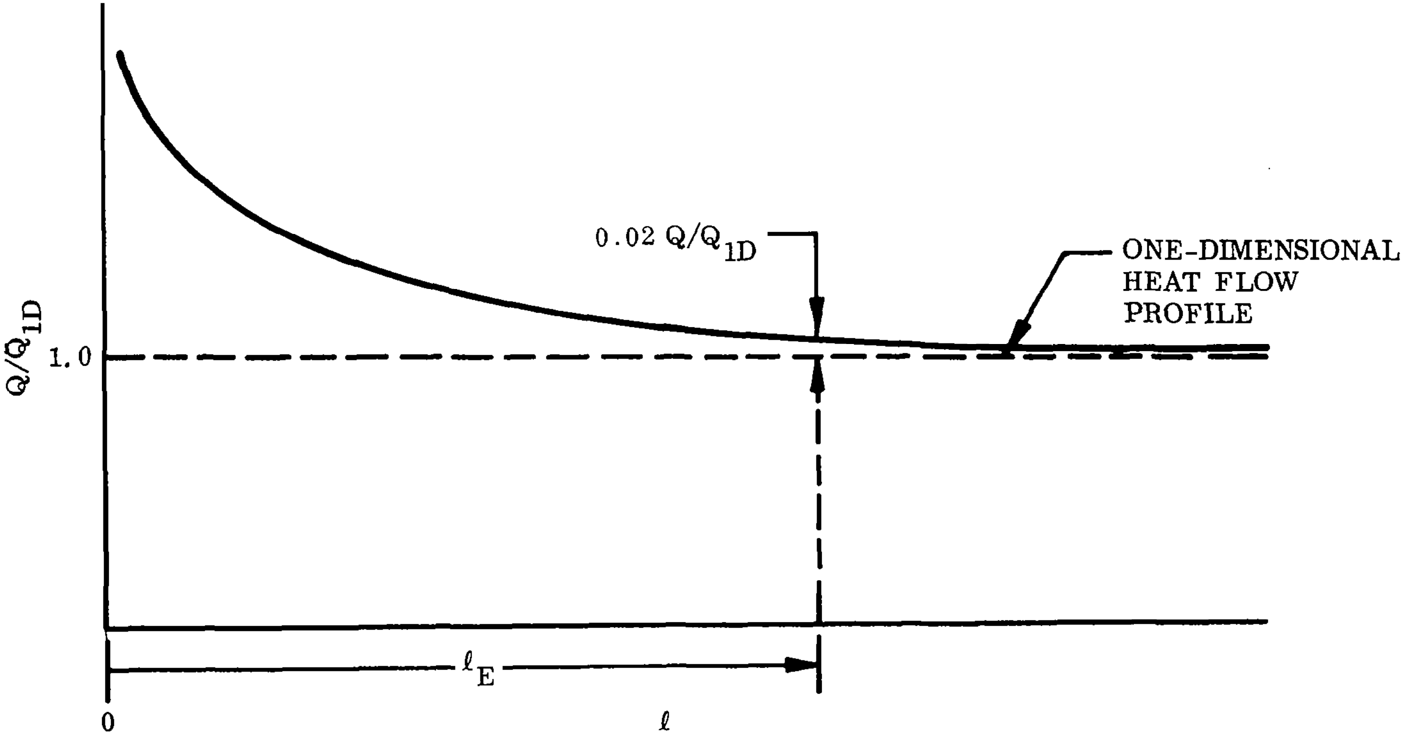

Figure 7 Heat Flow Profile in Bottom Nodes of Sector

The slab model is used to analyze the following three effects: a butt-type joint between the edge of the insulation and a portion of the spacecraft structure; overlapping of alternate layers of insulation at a joint; and an edge of the insulation exposed to a low temperature sink. The radial model is used for analysis of the two-dimensional effects of penetrations such as supports and apertures in the insulation. Two penetration cases are considered. One is a uniform temperature penetration, and the other for a linear temperature gradient along the wall of the penetrating member.

Butt joint. – The analysis is of the heat transfer in the region of a butt-type joint of the multilayer insulation with an isothermal boundary which is normal to the layers. This is representative of a structural strut or mounting bracket attached to the internal skin of the spacecraft (cold boundary). This longitudinal strut is assumed to penetrate the entire thickness of the multilayer insulation and is also assumed to be an isothermal extension of the cold boundary. An isotropic intermediary insulation is used to isolate the strut from the high parallel thermal conductivity of the anisotropic multilayer insulation. Figure 8 illustrates the position of the longitudinal strut in relation to the intermediary insulation, the multilayer insulation, and the cold boundary. The heat transfer between the strut and edge of the insulation is via radiation. The computer program calculated the temperature distribution throughout the insulation and the heat rates from the nodes at the boundary of the insulation for the steady state condition. The primary result for the butt joint study is the effect of the intermediary length (x) on the net heat transfer to the insulated surface and the strut. This is represented by the effective length ℓ_E and the ratio $Q_{\ell E}/Q_{1D}$, as shown in Figure 8. To determine the optimum system composed of a combination of multilayer and intermediary insulation, an additional length parameter ℓ^* is defined:

$$\ell^* = \ell_E \left(\frac{Q_{\ell E}}{Q_{1D}} - 1 \right) \tag{12}$$

The length ℓ^* is used to calculate the total heat into an insulation system of length ℓ:

$$Q_\ell = Q_{1D}(\ell^* + \ell) \tag{13}$$

The optimum insulation system is determined for the case when ℓ^* is a minimum. Plotted in Figures 9 through 12 are curves of x versus ℓ^* for several parameters that influence the heat transfer in the butt joint case.

The effect of the emittance of the strut ($\epsilon = 0.1$ to 1.0) on ℓ^* for two values of $K_{\|}$ is shown in Figures 9 and 10. Only for the larger value of $K_{\|}$ it is necessary to add an intermediary insulation between the strut and the multilayer insulation to reduce the overall heat transfer. For an emittance of 0.1 (Figure 10), ℓ^* is a minimum for an intermediary length x of approximately 1.0 cm. Likewise, for

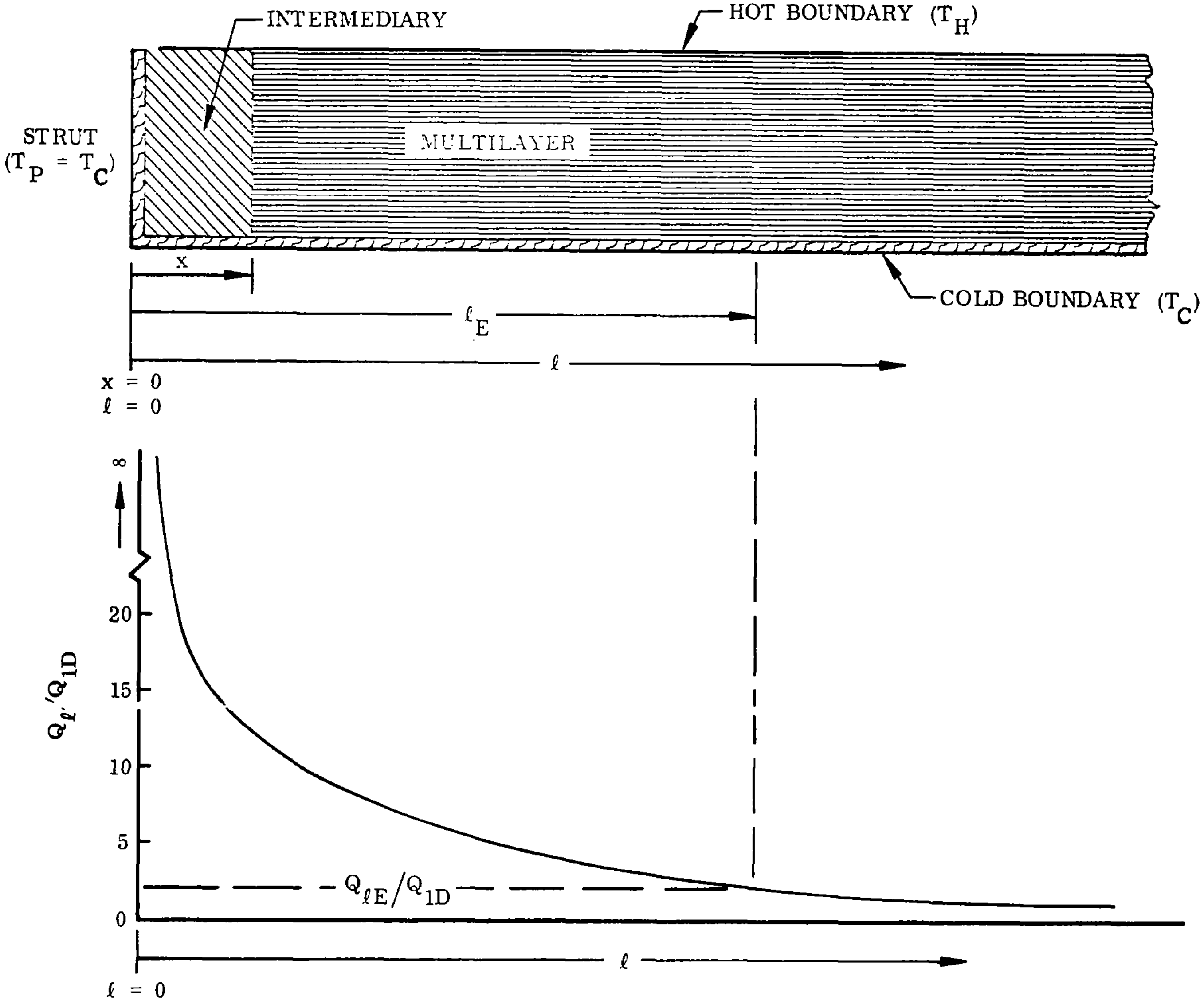

Figure 8 Strut Penetration

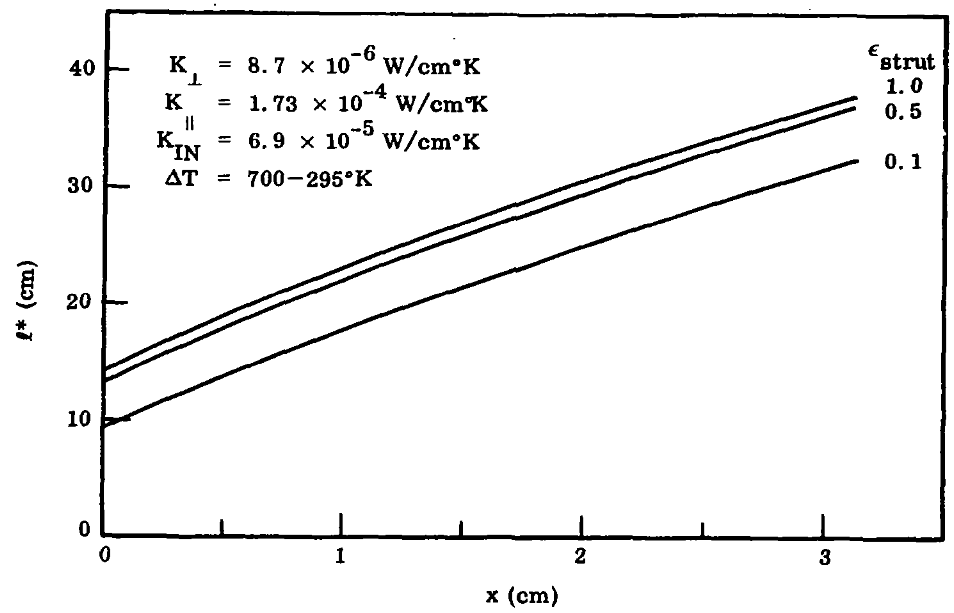

Figure 9 Influence of Strut Emittance on ℓ^* Versus x : $K_{\parallel}$ = 1.73 × 10^{-4} W/cm °K

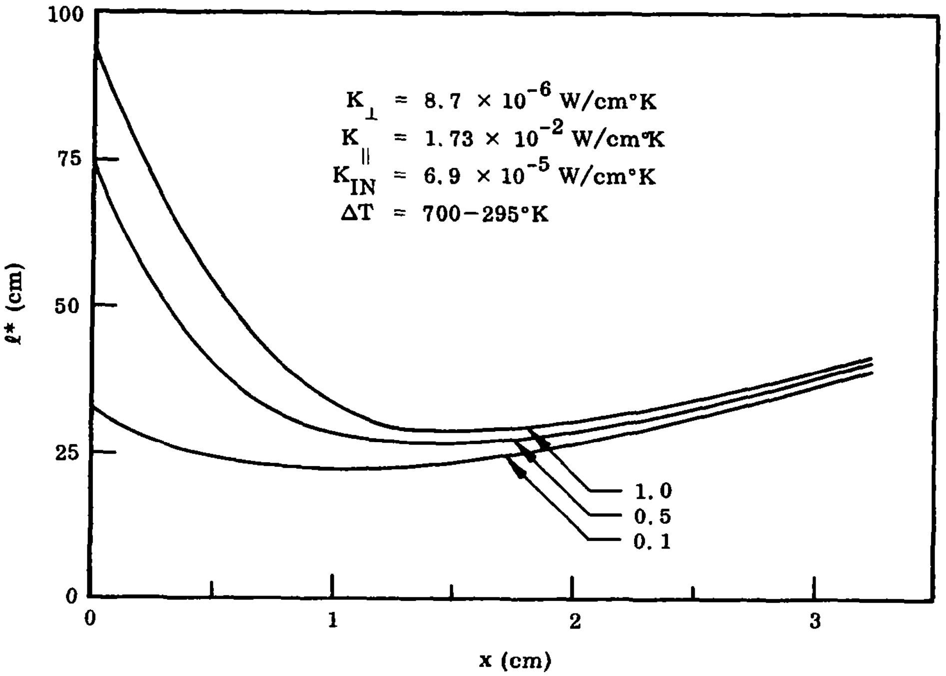

Figure 10 Influence of Strut Emittance on ℓ^* Versus x : $K_{\parallel}$ = 1.73 × 10^{-2} W/cm °K

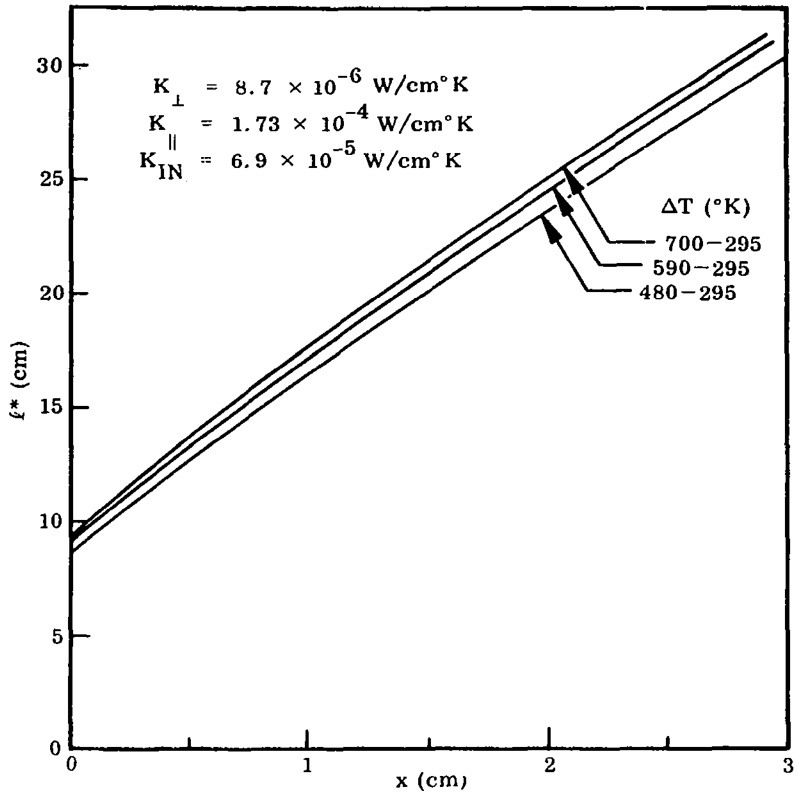

Figure 11 Influence of Hot Boundary Temperature on ℓ^* Versus x

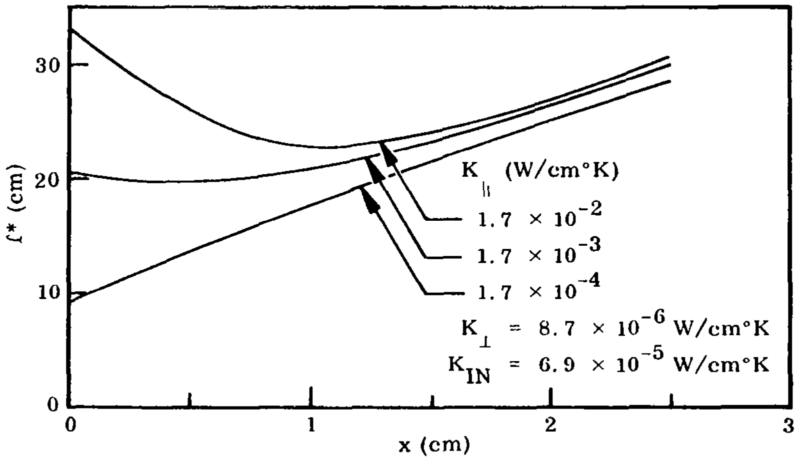

Figure 12 Influence of Parallel Conductivity, $K_{\parallel}$, on ℓ^* Versus x

emittances of 0.5 and 1.0, the optimum value of x is between 1.2 and 1.6 cm. Figures 11 and 12 show the influence on ℓ^* versus x of the parameters $T_{\|}$ and $K_{\|}$.

For the cases studied in the butt-joint analysis, only when $K_{\|}$ is equal to or greater than 1.7×10^{-2} W/cm °K is it necessary to use an intermediary insulation, and then a thickness of 1.2 cm is adequate to minimize the overall heat transfer. A multilayer insulation system using either aluminum or copper shields would have a parallel conductivity, $K_{\|}$, greater than or equal to 1.7×10^{-2} W/cm °K.

Overlap joint. – The overlapping of alternate layers of a multilayer insulation will cause a local increase in the density which will change the thermal conductivity of the insulation system in that region, and thus cause a perturbation in the one-dimensional heat transfer. The significant parameters in this analysis are length of overlap of alternate layers of insulation and the corresponding increase of heat transfer over that of a continuous multilayer system. Because shield materials such as metallized organic films come in limited sizes, it may be necessary to lap the shields of multilayer insulation for large areas of application. The effect on ℓ^* of the length of overlap of the shields is shown in Figure 13. It can be seen that it is far better to overlap the shield than to underlap it (i.e., opening in shield at joint). The effect of overlapping of the multilayer insulation is of little consequence to performance although the underlapping of shields is very detrimental to the thermal performance and should be avoided.

Edge rejection. – Because in some spacecraft applications an edge of the insulation system may radiate to a lower temperature heat sink or may receive additional energy, such as that from the sun reflected by an adjacent surface, a study was made of the effect of this additional heat-transfer path on insulation system performance. The information available was not sufficient for the case of reflected energy onto the edge, so the study was limited to use of the edge as a means of rejecting heat from the insulation system. Limited data for the case of heat addition are reported in ref. 15. The analysis of edge rejection also considers the addition of an intermediary of length x between the multilayer insulation and the edge. The physical situation is depicted by Figure 14.

The influence of $K_{\|}$ on the plot of ℓ^* versus x is shown in Figure 15. In Figure 16 ℓ^* is plotted for no intermediary. The negative values of ℓ^* in Figures 15 and 16 represent the decrease in heat transfer below that of the one-dimensional case. For example, an insulation system with $K_{\|}$ equal to 1.7×10^{-2} W/cm °K and no intermediary has an ℓ^* of -47 cm. For a multilayer insulation with edge rejection, the net heat transfer would be zero for the first 47 cm of length and one-dimensional for the remainder of the area.

This effect of the edge can be a benefit in a case such as rejecting heat from a penetration or boom and thereby reduce the total heat flux into the spacecraft by using a properly designed composite insulation system. However, it may also be detrimental to insulation performance, since it can lead to undesirable temperature gradients in the system as well as being a major source of heat addition to or rejection from the insulated component.

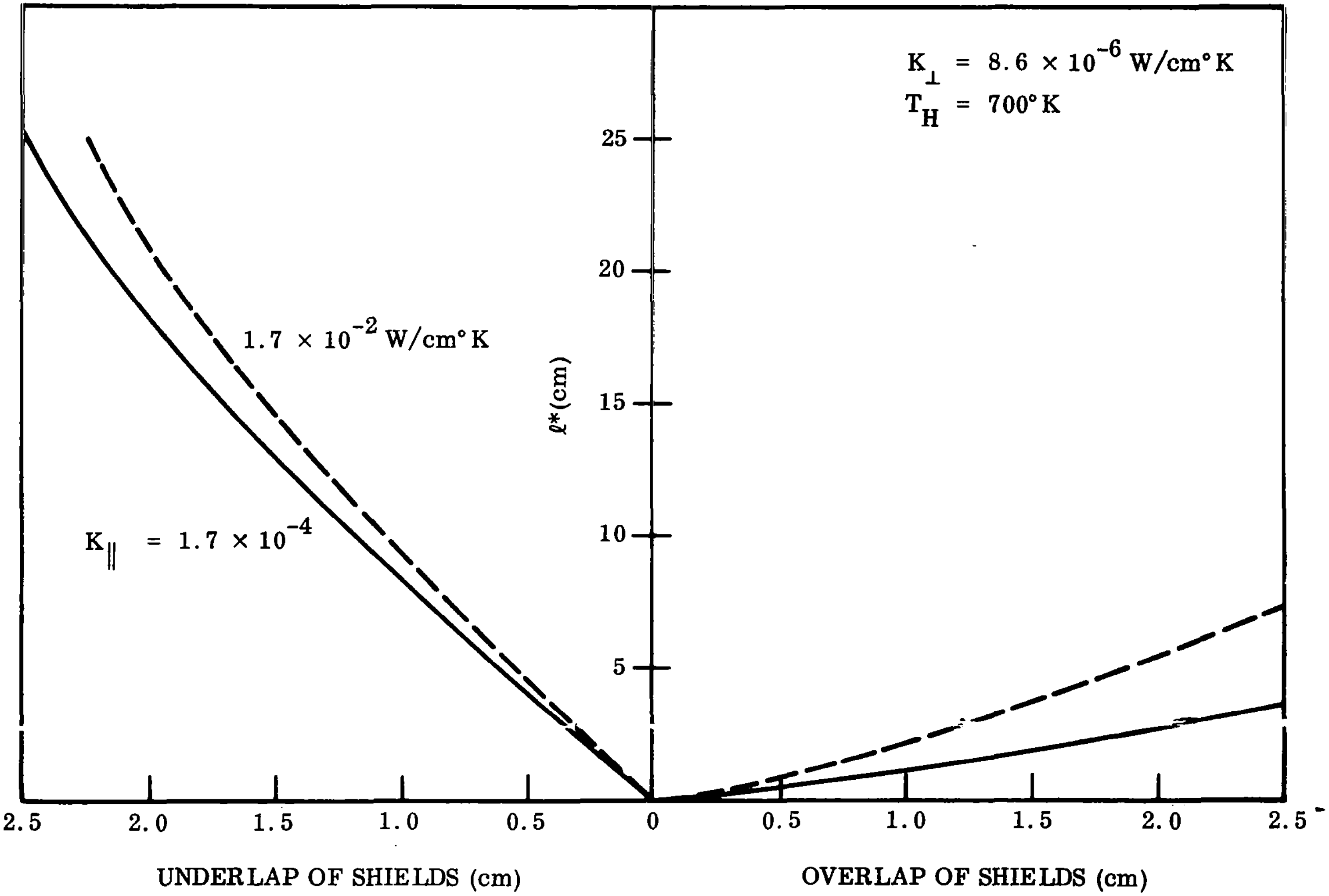

Figure 13 Effect of Lapping Shields on Performance of Multilayer Insulation System

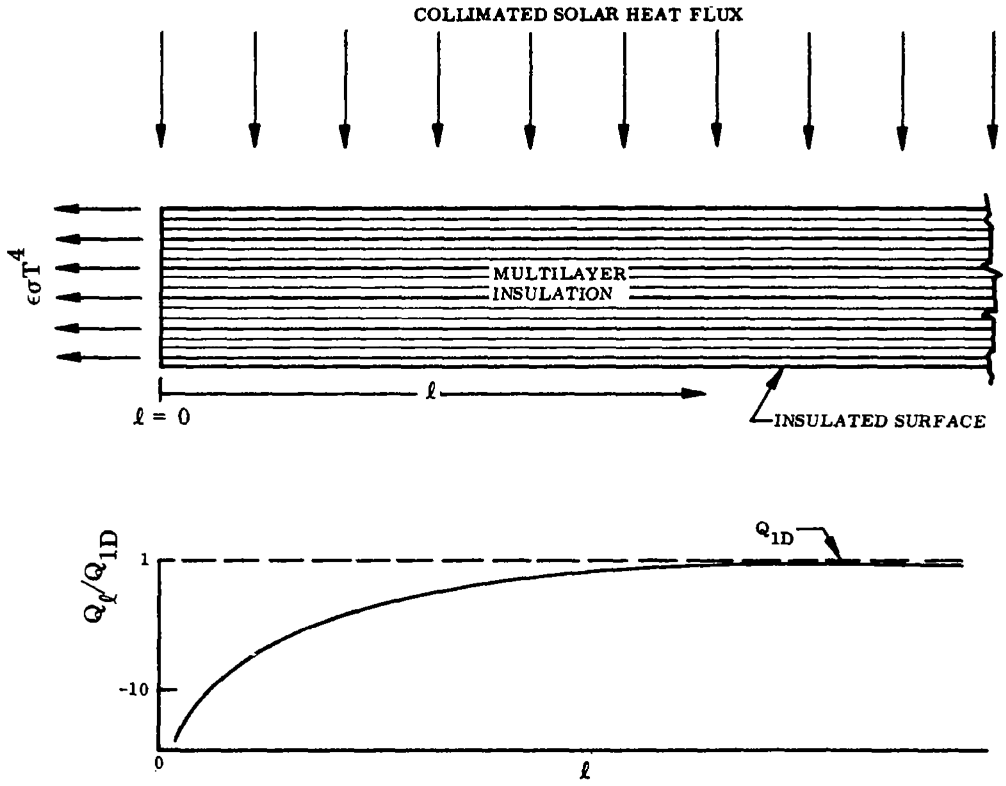

Figure 14 Edge Rejection

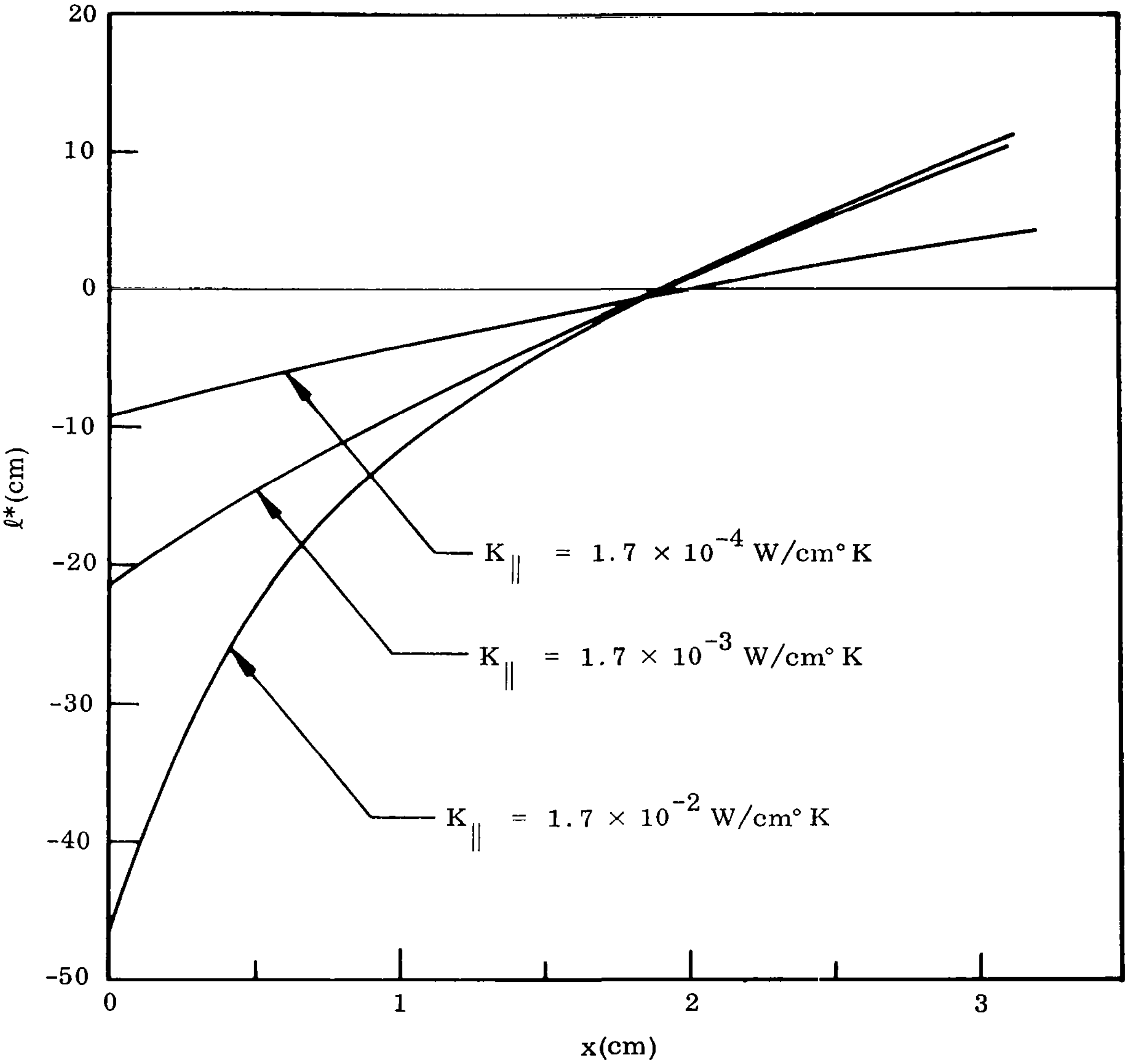

Figure 15 Edge Rejection – Influence of Parallel Conductivity $K_{\|}$ on ℓ^* Versus x

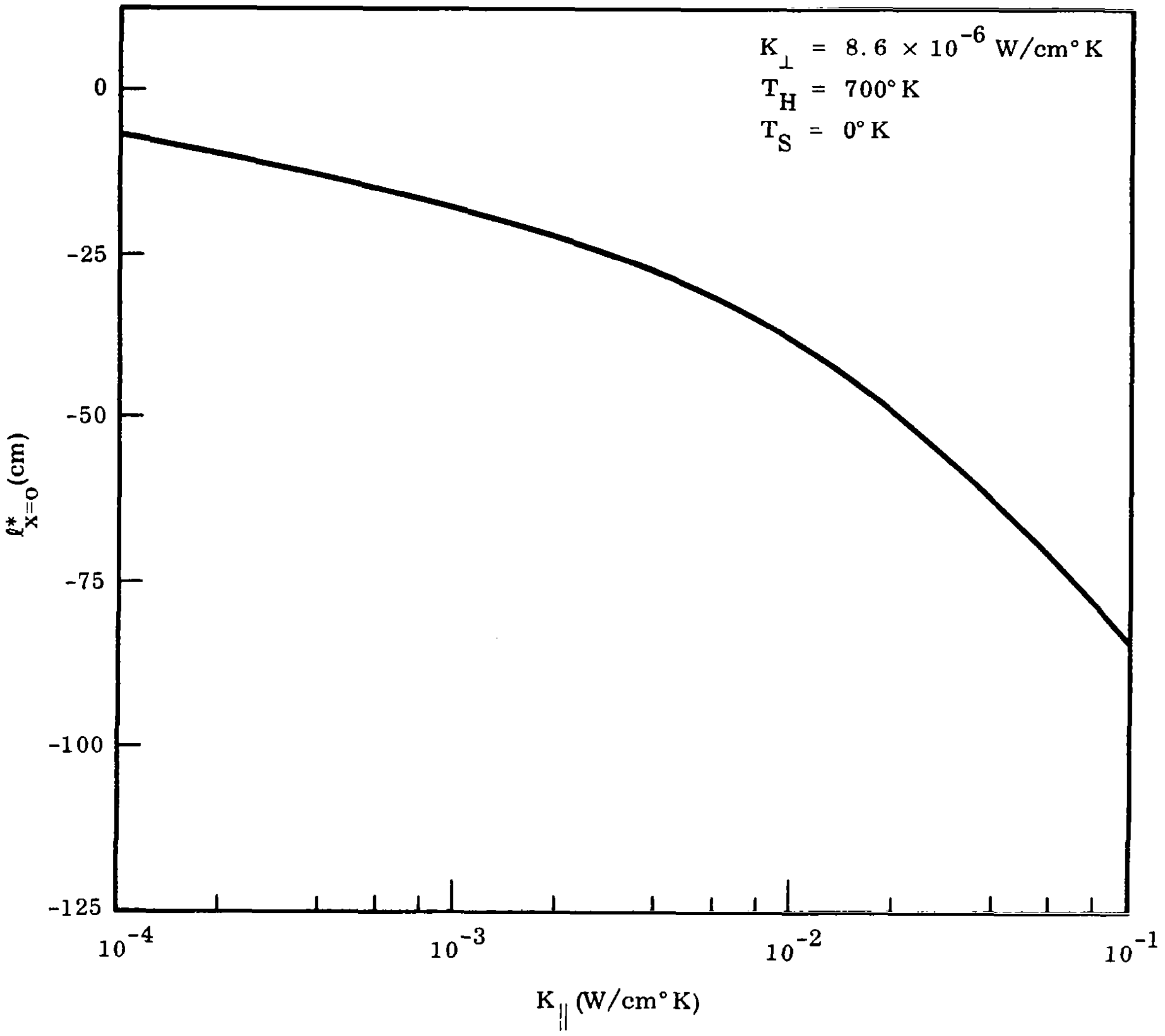

Figure 16 Edge Rejection – $\ell^*_{x=o}$ Versus $K_{\parallel}$

Constant temperature penetration. – Penetrations consisting of booms, support wires, and/or struts in which the radius of penetration varied from 0.16 to 2.54 cm were analyzed. The boundary temperature of the penetration was assumed to be constant at 422°K. An intermediary insulation was used between the penetration and the multilayer insulation. On the radial model, the only mode of heat transfer between the penetration and adjacent insulation is radiation. The emittance of the insulation was taken as 0.85, and the emittance of the wall was varied from 0.01 to 1.0. One series of computations was made with a pseudo-emittance of 10.0 on the penetration wall. This value of emittance was used in order to reduce the thermal resistance $(R \propto 1/\epsilon)$ between the penetration and insulation, simulating the effect of conduction heat transfer without adding a parallel resistance to the radial model network.

As stated previously, the output of the computer program for the radial model is the effective radius R_E and the ratio of the two-dimensional heat transfer to the one-dimensional heat transfer (Q_{R_E}/Q_{1D}) within the radius R_E. Similar to the slab model analysis, a combination of R_E and the ratio (Q_{R_E}/Q_{1D}) is necessary to determine the optimum combination of intermediary and multilayer insulation for minimum heat transfer when using the radial model. The parameter R^* is used to represent the increase in heat transfer due to a penetration of the insulation system and is defined as follows:

$$R^{*2} = \left(R_E^2 - R_p^2\right)\left[\left(Q_{R_E}/Q_{1D}\right) - 1\right] \tag{14}$$

The total heat transfer within the radius R is given by the following equation:

$$Q_R = Q_{1D}(R^{*2} + R^2) \tag{15}$$

The results of the analysis using the radial model with a constant wall temperature penetration are shown in Figures 17 through 22. It is concluded from the results of a broad parametric study that the influence of the radius of penetration R_p is significant only for R_p greater than 0.75 cm (Figures 17 and 18), and for $\epsilon_p > 0.1$ the results are similar for either radiation or conduction heat transfer between the penetrating members and the adjacent insulation (Figures 19 and 20). Because of this similarity, only the results of the influence of the parameters of $K_{\parallel}$ (Figure 21) and $K_{\perp}$ (Figure 22) on the heat transfer of a multilayer insulation system are presented for a penetration with a radius of 2.54 cm and conduction heat transfer between the penetrating member and the adjacent insulation. From Figure 21 it is shown that when $K_{\parallel}$ is greater than 1.73×10^{-3} W/cm °K, the use of an intermediary insulation between the multilayer insulation and the penetration decreases the heat transfer. An intermediary insulation of 0.5 to 1.0 cm in width is adequate to minimize the heat transfer for a multilayer system with $K_{\parallel}$ in the range of 1.7×10^{-3} to 1.7×10^{-2} W/cm °K.

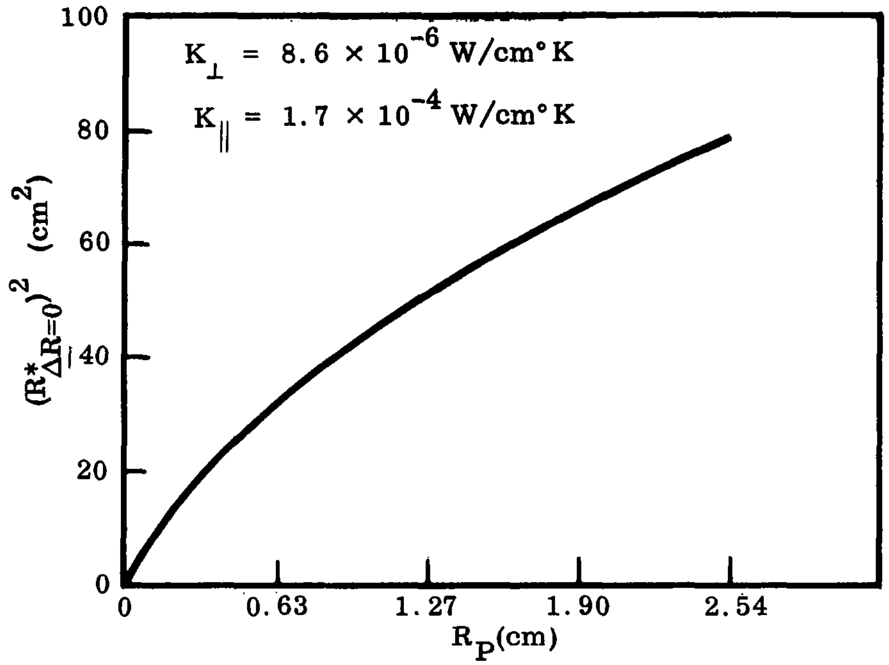

Figure 17 R^{*2} as a Function of Radius of Penetration for Case of Minimum R^*

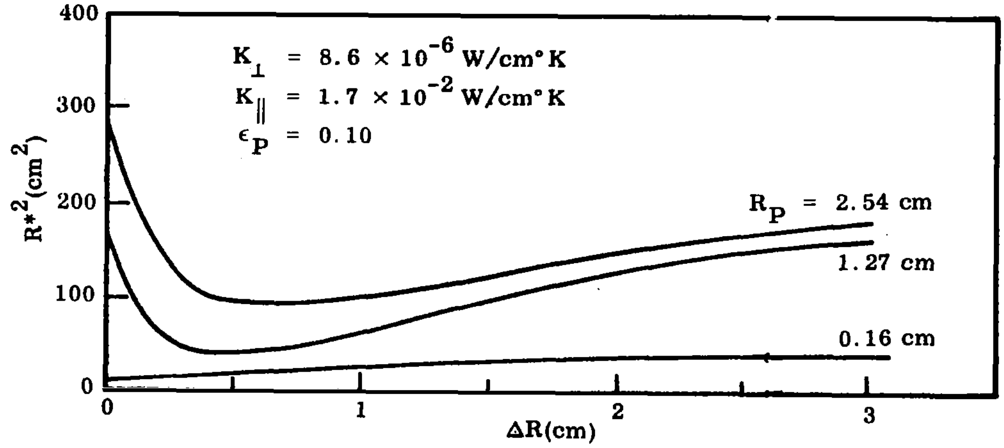

Figure 18 Influence of R_P on R^{*2} Versus ΔR

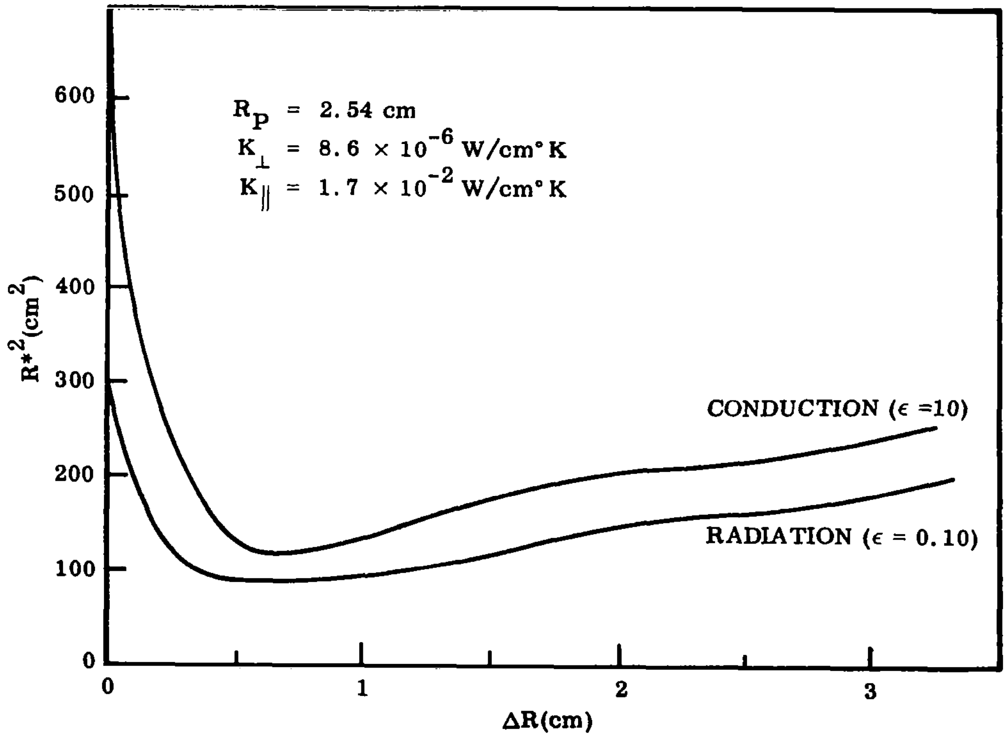

Figure 19 Influence of Heat Transfer Mode on R^{*2} Versus ΔR

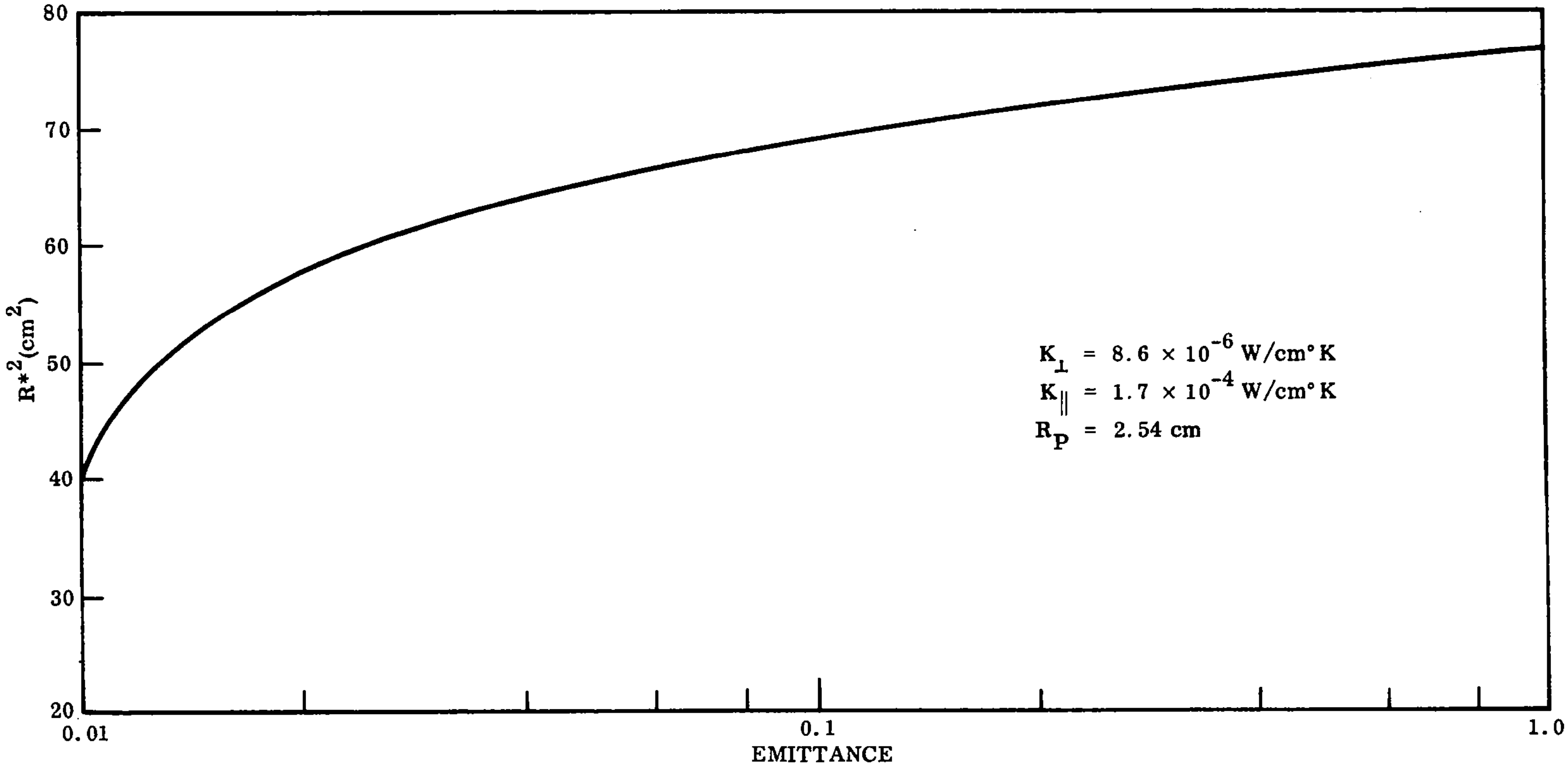

Figure 20 Influence of Emittance on R^{*2}

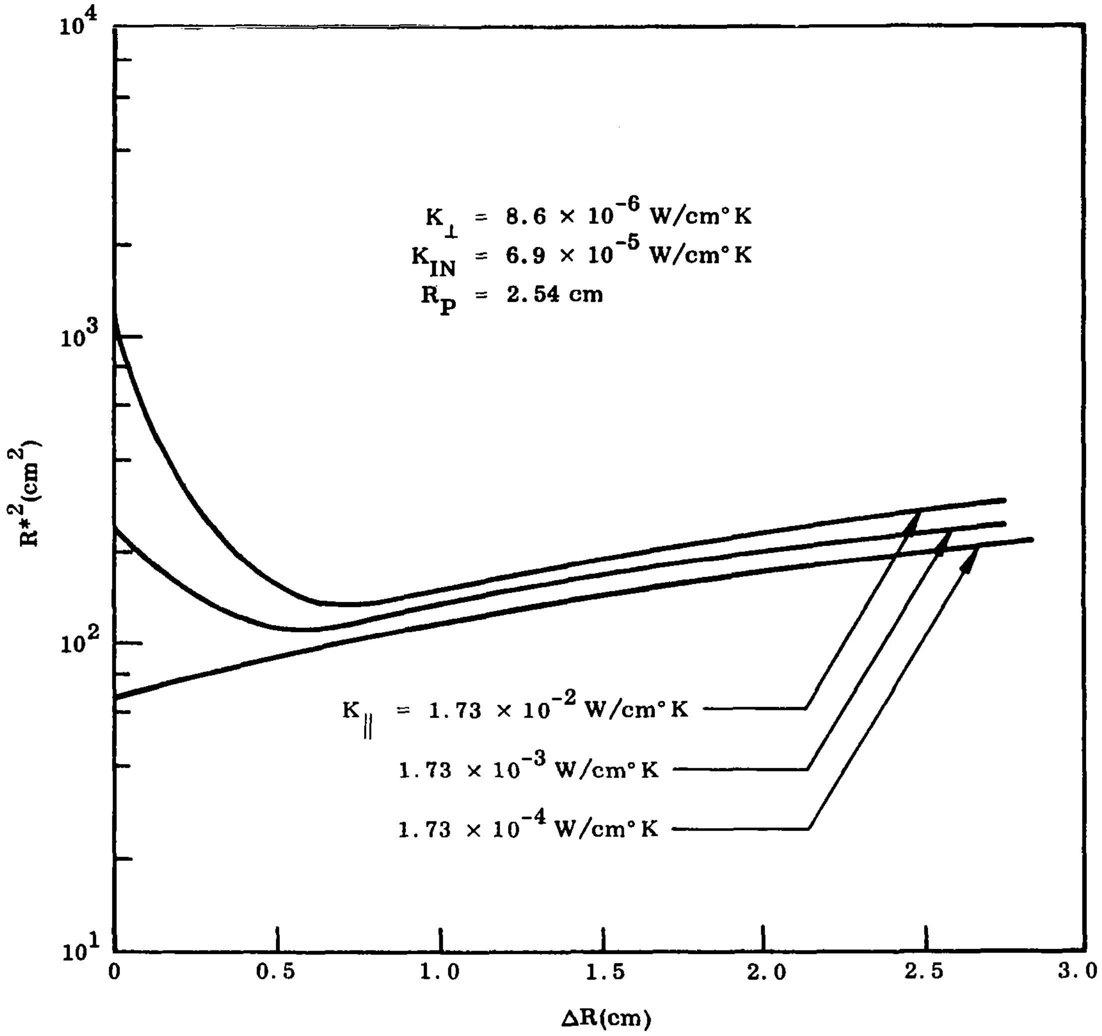

Figure 21 Influence of $K_\parallel$ on R^{*2} Versus ΔR With Conduction Heat Transfer Between Penetration and Intermediary

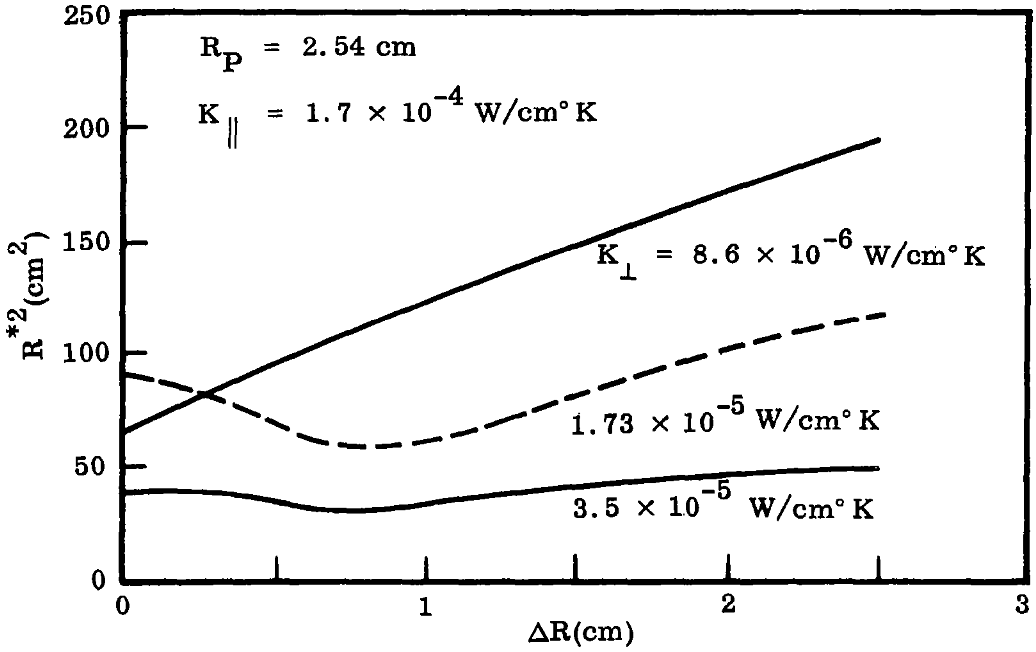

Figure 22 Influence of $K_{\perp}$ on R^{*2} Versus ΔR With Conduction Heat Transfer; T_{PEN} = 300°F

The dependence of $K_\perp$ on the selection of insulation for $K_\parallel$ of 1.7×10^{-4} W/cm °K or less is shown in Figure 22. When $K_\perp$ is less than 8.6×10^{-6} W/cm °K, no intermediary is necessary, but for $K_\perp > 1.7 \times 10^{-5}$ W/cm °K an intermediary insulation thickness of 0.7 cm is required to reduce the effects of two-dimensional heat transfer.

Linear gradient penetration. – Two series of multilayer insulation penetrations were analyzed for the case of a linear temperature gradient imposed along the penetration wall. In practice, the heat transfer between the insulation and penetration and the thermal resistance of the penetration and its juncture with the cold boundary would affect the temperature gradient in the penetration, as well as in the insulation. However, since this study does not include specific penetrations or constructions so that their resistances could be evaluated, the gradient in the penetration is held constant and linear. The mode of heat transfer between the penetration and the edge of the multilayer insulation is via conduction heat transfer. Because of the high thermal resistance of the insulation spacer materials, no allowance was made for contact resistance between the penetration and the multilayer insulation. The temperatures of the hot surface and the cold surface were 480° and 295°K, respectively, for all cases considered in this portion of the analysis.

The two linear temperature gradients considered are 28°K/cm and 116°K/cm. For temperatures of 480° and 295°K at the boundaries of the insulation and one-dimensional heat transfer through a 2.54-cm thickness of insulation, the linear temperature gradient in the insulation is 73°K/cm. Thus, for the low-temperature gradient, heat is absorbed by the penetration from the insulation, and for the high-temperature gradient the opposite effect occurs. The net heat transfer to the penetration from the insulation is assumed to be absorbed by the cold boundary surface.

Typical results of the computer analysis of the performance of multilayer insulation with a penetration having a linear temperature gradient imposed along the penetration length are presented in Figures 23, 24, and 25. Figure 23 illustrates the influence of the radius of penetration on the one-dimensional heat transfer for the two linear temperature gradients along the penetration. For $K_\perp \geq 8.6 \times 10^{-6}$ W/cm °K and $K_\parallel \leq 1.73 \times 10^{-4}$ W/cm °K, no intermediary insulation is required between the penetration and the multilayer insulation. The influence of an intermediary insulation and radius of penetration on the one-dimensional heat transfer is shown in Figure 24 for $K_\perp = 8.6 \times 10^{-6}$ W/cm °K and $K_\parallel = 1.73 \times 10^{-3}$ W/cm °K and for the two linear temperature gradients along the penetration. The additions of an intermediary of width 0.4 to 1.0 cm (ΔR) is sufficient to minimize the additional heat transfer into the insulation system due to the penetrations. The results shown in Figure 25 for $K_\perp = 8.6 \times 10^{-6}$ W/cm °K and 3.5×10^{-5} W/cm °K are similar to those presented in the previous figure.

4.2.2 Cylindrical Model

The model consists of four layers, each containing 160 nodes, as shown by Figure 26. This simulates one quarter of the insulation area and includes one penetration, an edge exposed to a variable temperature environment, and an edge which

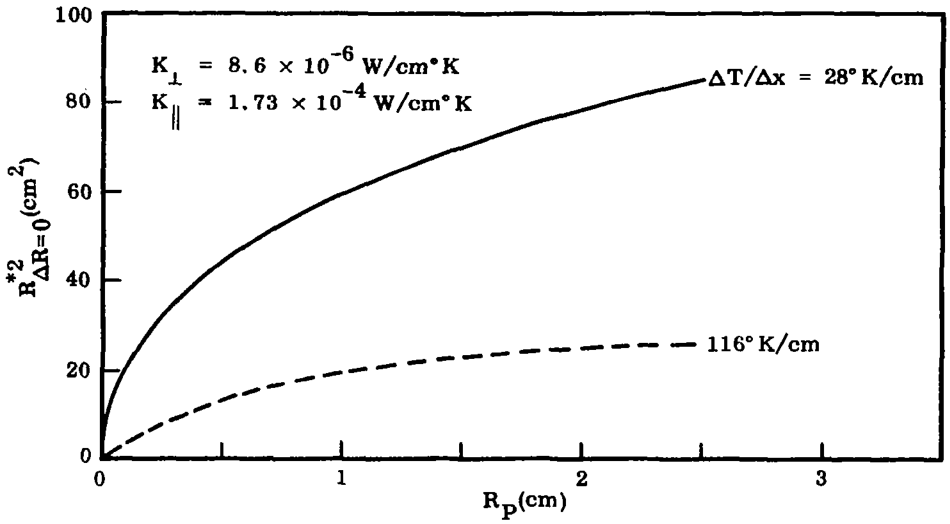

Figure 23 Influence of Radius of Penetration on One-Dimensional Heat Transfer for Linear Temperature Gradient at Penetration

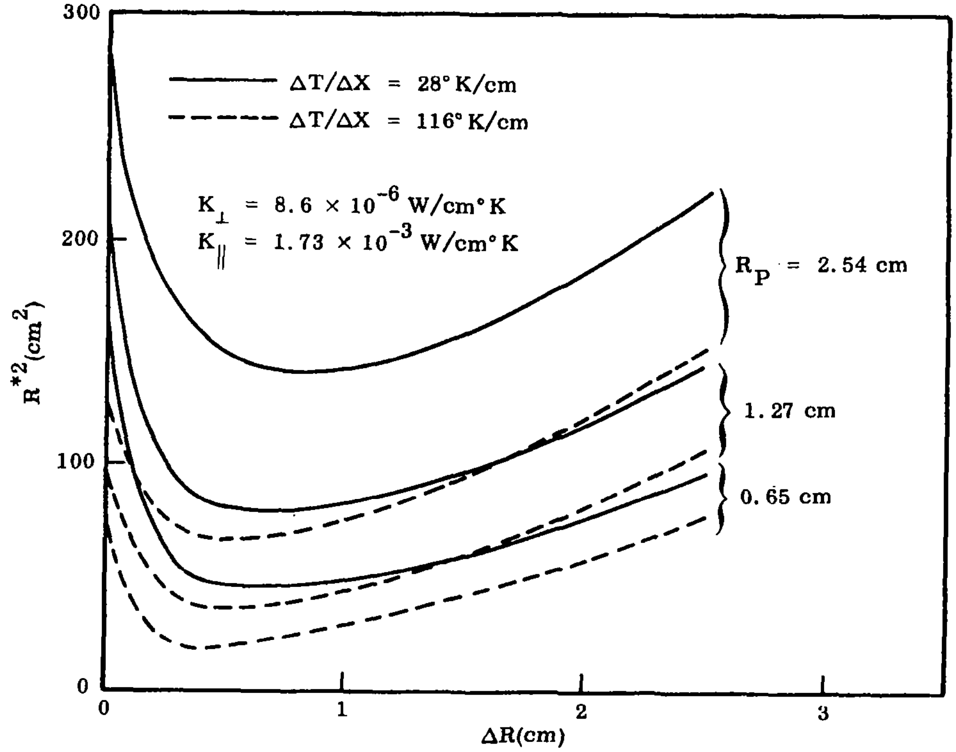

Figure 24 Influence of Intermediary Insulation and Radius of Penetration on One-Dimensional Heat Transfer for Linear Temperature Gradient at Penetration Wall

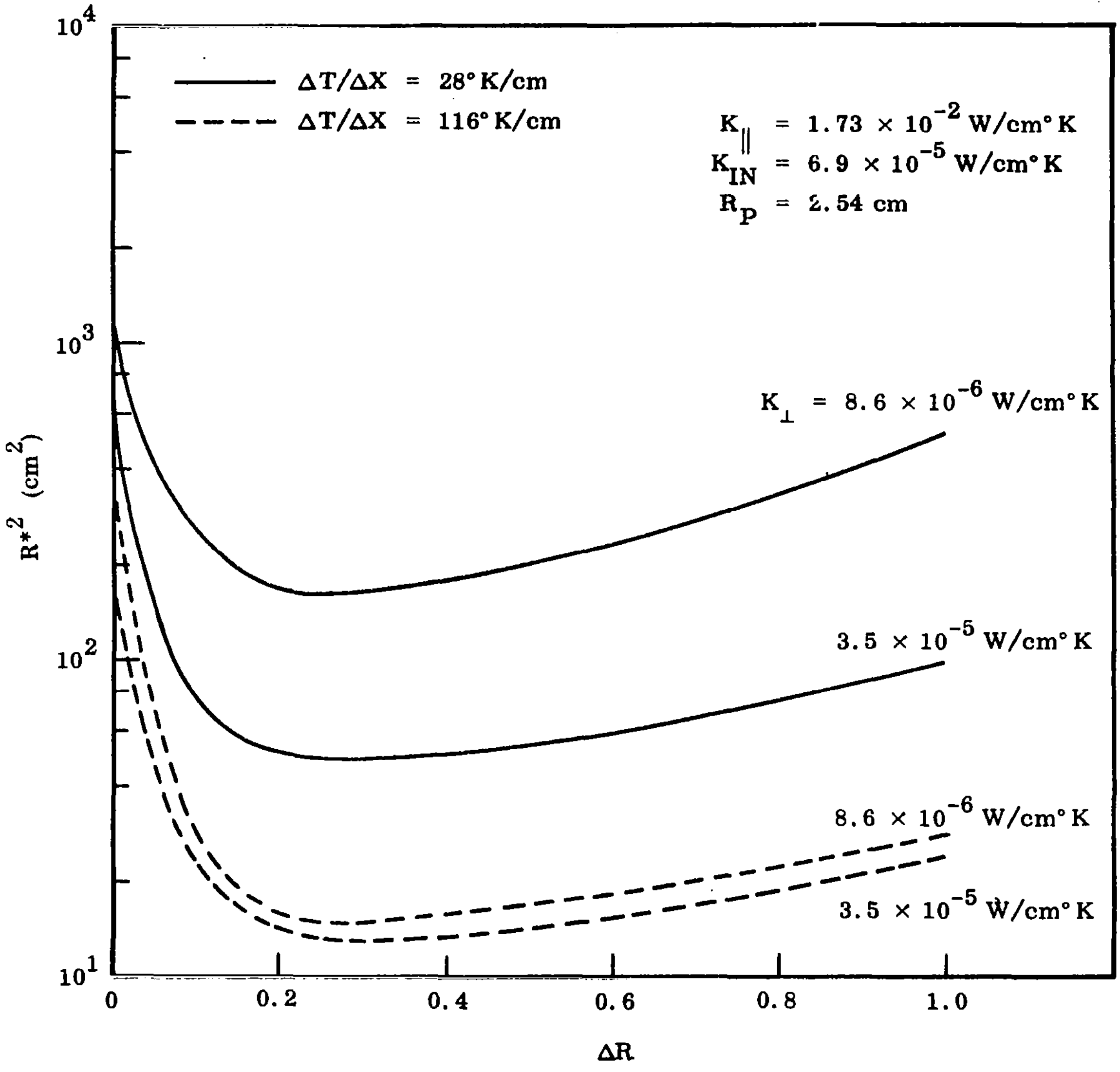

Figure 25 Influence of Intermediary Insulation and Thermal Conductivity in Normal Direction on One-Dimensional Heat Transfer

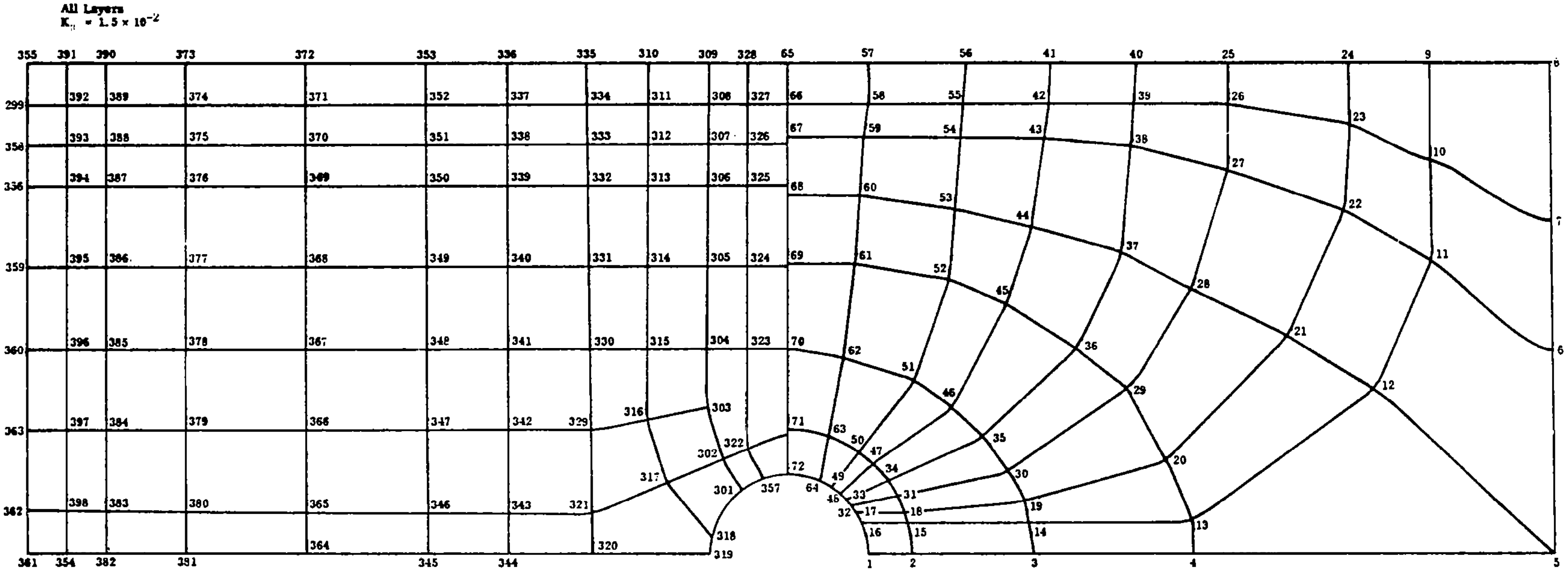

Figure 26 Cylinder Model Nodal Network

may be connected to a constant temperature boundary. The remaining two edges are considered as adiabatic surfaces on the basis of the symmetry of the configuration. The top and bottom layer nodes, through the thickness of the insulation, are connected to constant temperature boundaries. Similarly, the exposed edges are connected through variable resistances to a constant temperature source or sink. The penetration edge may be connected through variable resistances to either a constant temperature boundary or one having a linear gradient from the insulation cold boundary.

The nodal geometry of the layers of the model was based upon the method of curvilinear squares. Each node is at the center of a prismatic bar assumed to possess constant thermal properties. Although the program will accommodate variable thickness, the model thickness for this analysis was constant at 0.89 cm, based upon the insulation thickness used during the test phase of the program.

The model is used in conjunction with the Three Dimensional Insulation Penetration Model Program (ref. 16) which is composed of THERMOTRAN source statements and processed through the IBM 7094 operating system FORTRAN 2, Version 3.

Input parameter variations for the cylindrical model were not as extensive as those employed for the radial and slab models. Insulation conductivities were limited to those of an aluminized polyimide film -- Dexiglas system. Boundary temperatures were varied from 300° to 650°K for the hot surface and 77° and 300°K for the cold surface. The lower temperatures were to simulate the cylindrical insulation experimental test program conditions for comparison of experimental data with the analysis. No intermediary insulation was considered in this portion of the analysis program.

Butt joint. -- The influence of a butt-type joint without any intermediary insulation to a strut or protuberance from the cold boundary at that temperature is shown by Figure 27. The distance over which the two-dimensional effect is present is represented by the term ℓ^* , and this is analogous to that used for the slab analysis. The heat input ratio (Q/Q_{1D}) was developed for the 30.5 by 96 cm system. These results are comparable to those developed with the slab model.

Constant temperature penetration. -- Typical results of the penetration analysis, no intermediary insulation, are shown by Figure 28. These agree with those obtained using the radial model. Heat input ratios for the radial model are calculated using the R^* term. The heat input ratios for the cylindrical model are taken directly from the nodal heat balances.

Edge rejection. -- The effects of edges of the insulation which are exposed to a 0°K sink were analyzed for three temperature conditions. A constant temperature strut was present for all cases, and a strut plus penetration used for several studies. These were included as they present heat-flow paths from the cold boundary into the insulation and as such may remove an appreciable amount of heat from the structure. No intermediary insulation was considered as its effect was demonstrated in the earlier studies.

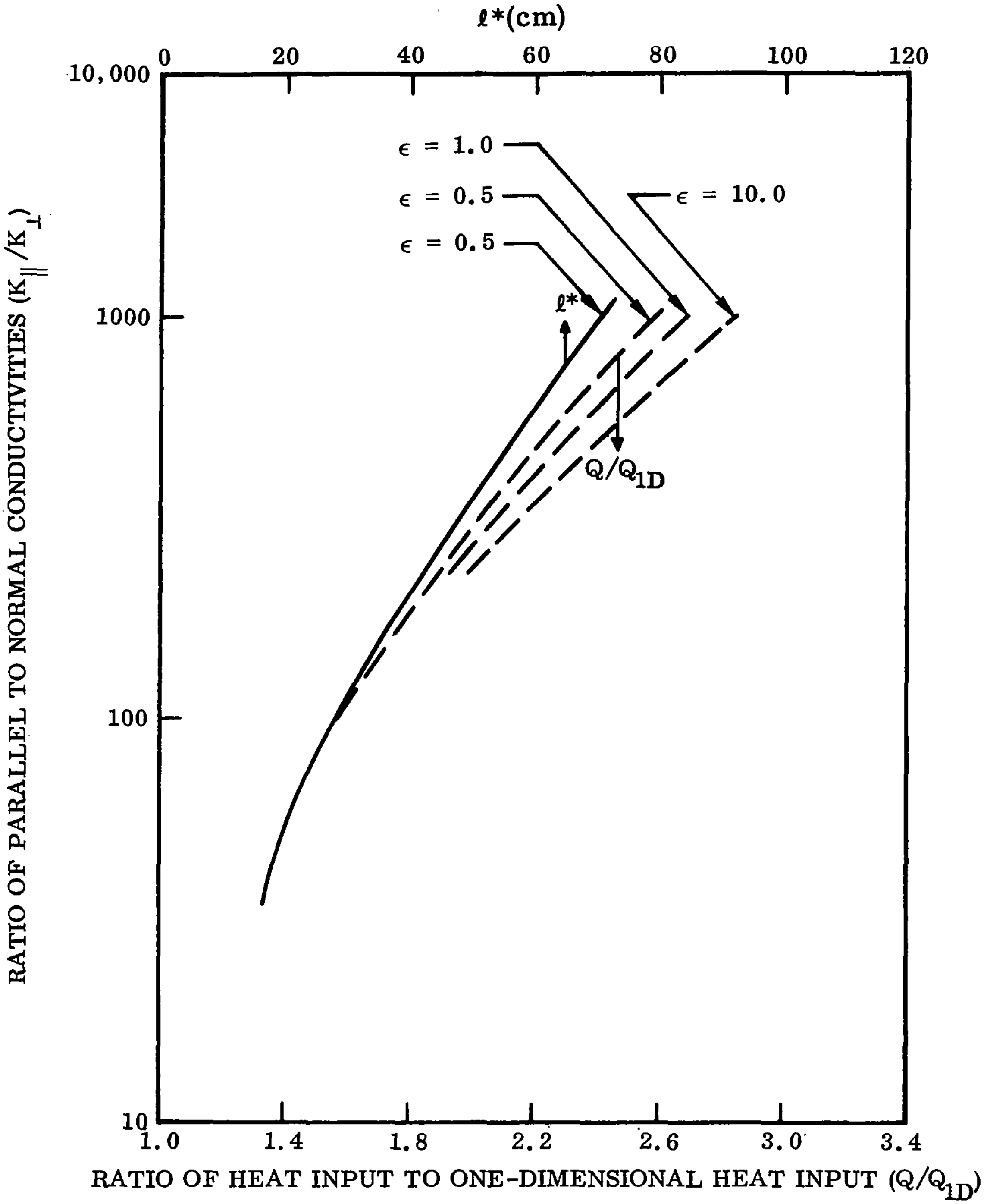

Figure 27 Dimensionless Heat Inputs and ℓ* as a Function of Conductivity Ratio for Cylindrical Model Analysis

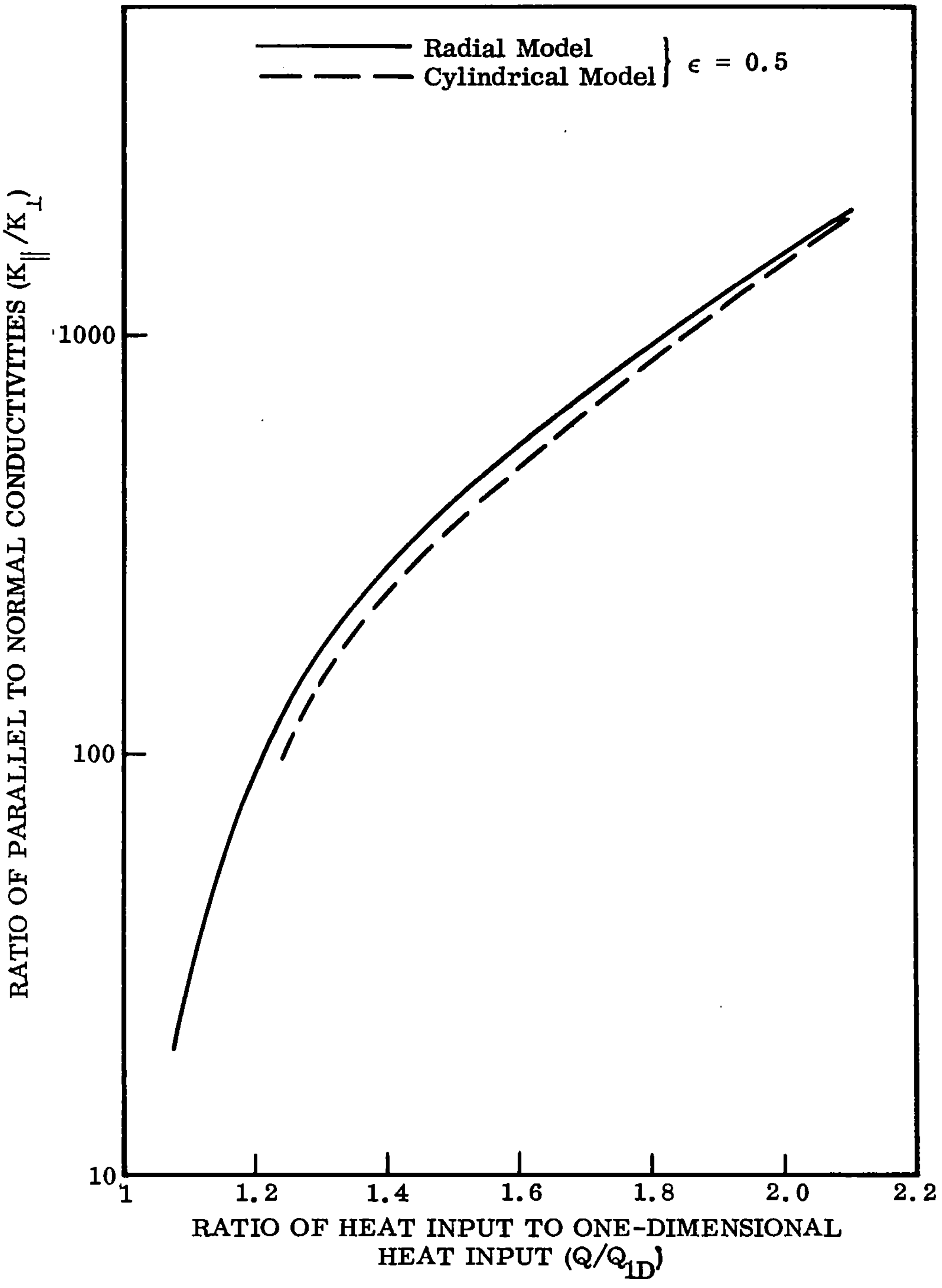

Figure 28 Dimensionless Heat Inputs as a Function of Conductivity Ratio for Cylindrical Model Analysis

For the conditions of a 300°K hot boundary and a 77°K cold boundary imposed upon the insulation system, the edges reduced heat input across the cold boundary from 20 to 70% of that occurring for the one-dimensional case. The range of parallel conductivities was varied from 1.7×10^{-4} to 1.7×10^{-3} W/cm °K for a constant $K_\perp$ of 1.6×10^{-6} W/cm °K. Examination of the layer temperature profiles for a system without a penetration showed the two-dimensional effects extended approximately 12 cm from the edge for a $K_\parallel$ of 4.3×10^{-4} W/cm °K. For larger values of $K_\parallel$, no one dimensional area was present in the entire 30.5 by 96 cm system.

For insulation at higher temperatures, the edge results in a heat flow across the cold boundary toward the edge. The strut and penetration transferred heat from the cold surface of the insulation to the inner insulation layers and out across the edges. As an example, for a 533°K hot boundary with a 300°K cold boundary, 50% of the energy rejected by the edges comes from the cold surface. A temperature profile through the insulation thickness showed the temperatures of the inner section of layers were lower than the cold boundary temperature. The heat rejection effect is shown graphically in Figure 29 for one insulation system. This presents a ratio of heat crossing the substrate or structure-insulation interface to the one-dimensional heat flux (Q/Q_{1D}) as a function of the mean temperature of the insulation system. This is not the edge temperature as it is a strong function of $K_\parallel$ and the presence of other perturbations such as penetration. The negative values of Q/Q_{1D} indicate that heat is being transferred from the insulated surface to the sink across the exposed edges.

4.3 DISCUSSION OF RESULTS

For the 400° to 700°K temperature range, the major portion of heat transfer occurs by radiation. Using commercially available reflective shield materials, the radiation is three to ten times that due to the conduction mechanisms. At an ambient pressure of 10^{-5} Torr or less, the conductivity of the gas phase is negligible. Typical values for radiation, solid, and gas conductivities calculated for a multilayer system at 700°K (300°K cold boundary) are 1.6×10^{-6}, 3×10^{-7}, and 1×10^{-8} W/cm °K, respectively, for a system at a layer density of 35 layers/cm. To attain effective thermal conductivities approaching those of the solid phase conductivity, 3×10^{-7} W/cm °K, significant improvements must be made in reflective shield materials (achieve total hemispherical emittance value of 0.025 or less) and spacer materials (maximize scattering cross section).

Because multilayer insulations have anisotropic thermal properties, careful consideration must be given to the lateral conduction effect of penetration and exposed edges. The degradation in thermal performance of such an insulation system is greatly magnified as the size decreases, and for small blankets the entire insulation may become a two-dimensional problem with the overall conductivity or conductance an order of magnitude different from the true one-dimensional thermal conductivity of the insulation.

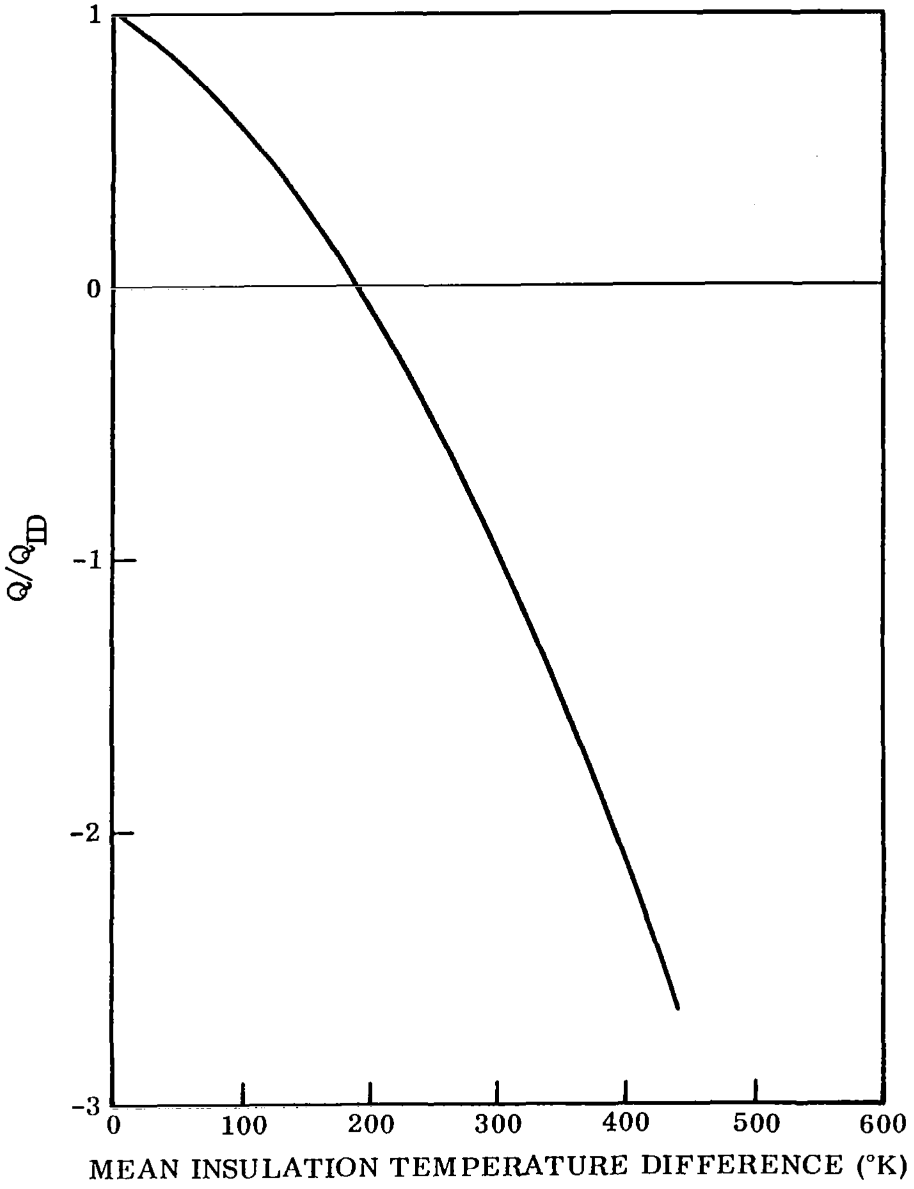

Figure 29 Ratio of Total Heat Transferred Across Insulation-Substrate Interface to the One-Dimensional Heat Transfer as a Function of Differences of Mean Insulation Temperature and Sink Temperature ($\epsilon = 0.85$)

From the results of the analytical studies of insulation discontinuities, the following conclusions may be drawn:

- When the ratio of parallel to normal conductivity is less than approximately 200, an intermediary insulation is not necessary between the insulation and a penetrating member at the temperature of the cold boundary. The metallized polyimide film insulation with paper-type spacers approaches this value, and the use of an intermediary is not recommended. For larger ratios of $K_{\parallel}/K_{\perp}$ an intermediary insulation will decrease the insulation degradation due to the penetration.

- For a penetrating member having a temperature gradient such that energy is transferred into the colder layers, the use of an intermediary insulation is the recommended practice. The lateral length of the intermediary is typically on the order of 0.5 to 1 cm.

- Effects of exposure of an edge of the insulation to a high temperature source of energy or a low temperature sink such as space may seriously degrade the insulation performance. For elevated temperatures, insulation edges radiating to space may remove a significant amount of heat from the vehicle or component. The use of an intermediary insulation is mandatory for such conditions. However, each application must be analyzed to determine the optimum construction. As an example, for an edge radiating to an environment within 100° to 150°K of the insulation temperature, the two-dimensional effect may not warrant an intermediary. Whereas, the case of radiation to or from a very high or low temperature source requires 2 to 3 cm of intermediary material.

Section 5

EXPERIMENTAL PROGRAM

The experimental investigations were conducted in three areas; (1) evaluation of materials suitable for construction of multilayer insulation; (2) determination of the thermal performance of a number of systems; and (3) verification of the analytical models. The paucity of thermophysical properties data in the literature required that measurements be made of optical and thermal properties for a number of shield and spacer materials. Effective thermal conductivity measurements were made on a variety of insulations to provide both heat-transfer data and information on the validity of the simplified analytical model for multilayer insulation. Finally, multidimensional effects were experimentally determined and compared with the results of the analytical studies.

5.1 MATERIAL EVALUATIONS

The general material considerations are chemical and structural stability over the specified temperature range, density, availability, and cost. Specific conductive heat-transfer parameters are thermal conductivity, geometry, thickness, and fiber diameter. The major radiative properties are emittance, refractive index, and transmittance. The materials selected for study, their application, and reason for selection are summarized in Table 1.

TABLE 1. – MATERIALS SELECTED FOR INITIAL STUDY OF BASIC PARAMETERS

Material	Use	Comment
Stainless steel	Shield	Relatively high emittance
Aluminum foil	Shield	Low emittance, high thermal conductivity
Kapton polyimide film[a] coated with vacuum-deposited aluminum, gold, and silver	Shield	Low emittance and thermal conductivity, can be used with or without separator
Glass fiber paper	Spacer	Low thermal conductivity, high scattering and absorption coefficient
Refrasil	Spacer	Low thermal conductivity, relatively lower scattering and absorption coefficient
Carbon cloth	Spacer	High absorption coefficient

[a] E.I. DuPont de Nemours & Co., Inc.

5.1.1 Reflective Shields

Total hemispherical emittance as a function of temperature, stability at temperature in vacuum, and coating characterization were the major items for experimental investigation. A number of coated polyimide film specimens were obtained to determine the total hemispherical emittance obtainable from commercial coating companies. Thermal and mechanical properties are based upon data available in the literature. Source and pertinent properties of the shield materials are listed in Table 2.

Film characterization. – Several measurements techniques were employed to determine the thicknesses of the metal films on the polyimide film for correlation with total emittance data. These were electrical resistance, light-transmission, weight by difference, and electron microscope studies of cross sections of the film. Resistance, weight difference, and the electron microscopy were utilized for the aluminum coatings. Light transmission and resistance were used to characterize the gold and silver coatings. Also, for the aluminum coatings prepared by D. L. Clausing Company, optical flats were placed adjacent to the film during the evaporation process. Film coating thicknesses on the flats were determined by the interferometer method.

The results of the coating characterization studies are summarized in Table 3. The resistance method gave reasonably accurate data on coating thickness for the gold and silver coatings examined. For several of the aluminum coatings, large discrepancies are apparent between the resistance method and the electron microscope studies and weight measurements. This is attributed to the character of the coatings themselves. Numerous pin holes and irregularities which would result in a larger value of resistance were observed in specimens 2, 3, and 4. The coatings appear to consist of a series of small mounds as shown by Figure 30. Inspection of the electron microscope cross sections also shows coating irregularities (Figure 31).

No single method was found to be suitable for determining the thickness of all coatings examined. The resistance method is dependent upon the integrity of the electrical path through the coating. Therefore, the results are subject to any discontinuities in the coating, such as pin holes or granular structure, which might be a function of the deposition process, but are not necessarily an indication of thickness or optical properties of the coating. A combination of resistance and light transmission measurements offers the best method for evaluating the metallic coatings on thin organic film reflective shields.

Optical properties of shields. – The lack of optical properties data on the polyimide film prompted the measurement of both spectral transmittance and reflectance. Transmittance measurements were performed with the Beckman Model IR-12 Infrared Spectrophotometer over the wavelength region from 2.0 to 50 μ.* The infrared reflectance measurements were performed with a Perkin-Elmer heated cavity reflectometer and Model 13 Infrared Spectrophotometer.* The spectral reflectance of

---

*NASA, Ames Research Center.

TABLE 2. – REFLECTIVE SHIELD MATERIALS

Material	Source	Density (g/cm^3)	Thickness (mm)	Specific weight (kg/m^2)	Thermal conductivity at 300°K (W/cm °K)	ϵ_T at 300°F
Aluminum foil	Alcoa Mil A143	2.70	6.35×10^{-3}	1.72×10^{-2}	3.80	0.035
Stainless steel foil, type 316	Rodney Metals	8.02	2.54×10^{-2}	2.3×10^{-1}	1.6×10^{-1}	0.132
Kapton polyimide film, coated with aluminum	McCordi Metallizing	1.42	2.5×10^{-2}	3.58×10^{-2}	1.55×10^{-3}	0.050 to 0.080
Kapton polyimide film, coated with aluminum	D. L. Clausing Company	1.42	2.54×10^{-2}	3.58×10^{-2}	1.55×10^{-3}	0.035 to 0.055
Kapton polyimide film, coated with gold	D. L. Clausing Company	1.42	2.54×10^{-2}	3.58×10^{-2}	1.55×10^{-3}	0.038 to 0.050
Kapton polyimide film, coated with silver	D. L. Clausing Company	1.42	2.54×10^{-2}	3.58×10^{-2}	1.55×10^{-3}	0.040 to 0.060
Kapton polyimide film, coated with aluminum	NRC Corp.	1.42	1.27×10^{-2}	1.79×10^{-2}	1.55×10^{-3}	0.029 to 0.058
Kapton polyimide film, coated with gold	Schjeldahl	1.42	1.27×10^{-2}	1.79×10^{-2}	1.55×10^{-3}	0.032
Kapton polyimide film, coated with silver with SiO$_x$ overcoating	Schjeldahl	1.42	1.27×10^{-2}	1.79×10^{-2}	1.55×10^{-3}	0.028

?

TABLE 3. – SUMMARY OF CHARACTERIZATION STUDIES OF METAL-COATED POLYIMIDE FILM

Aluminum coatings

Specimen no.	Specified thickness (Å)	Optical flat monitor	Measured coating thickness (Å)		
			Resistance	Weight difference	Electron micrograph
A2	2000	2200	1250	–	1500 to 3000
A3	1000	800	350	870	–
A4	1000	1050	500	1080	600 to 1200
A5	500	650	600	480	600
A6	800	850	900	960	900

Gold coatings

Specimen no.	Specified thickness (Å)	Measured coating thickness (Å)	
		Resistance	Light transmission
G2	500	480	525/550
G3	500	480	525/550
G4	600	610	650/700
G5	1000	840	750/925

Silver coatings

Specimen no.	Specified thickness (Å)	Measured coating thickness (Å)	
		Resistance	Light transmission
S1	700	640	opaque
S2	700	670	700/750
S3	500	520	500/530
S4	400	410	450/480
S5	400	390	370/390

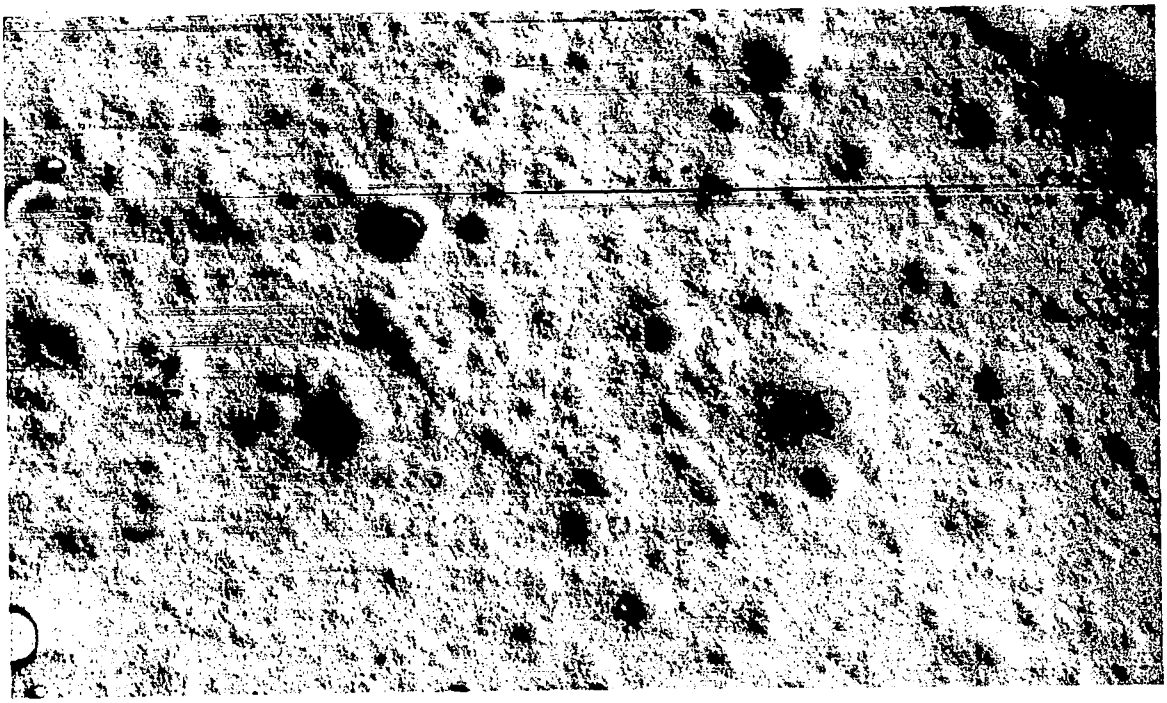

4000×

Figure 30 Appearance of 2200 Å Aluminum Surface on Polyimide Film

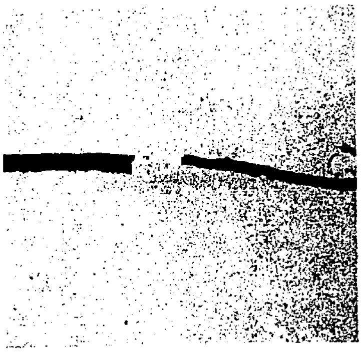

4000×

Figure 31 Cross-Section Photomicrograph of Aluminized Polyimide Film Sample A2 the film side of 2.54 x 10^{-3} cm (1 mil) singly aluminized polyimide material is shown in Figure 32. The material exhibits spectral absorption characteristics very similar to Mylar except for the visible wavelength region. Total hemispherical emittance at 300°K is 0.60. The transmission of 2.54 x 10^{-3} cm and 7.62 x 10^{-3} cm (1 and 3 mils, respectively) thick films, shown in Figure 33 for the wavelength region from 2.0 to 50.0 μ, illustrates the relatively high transparency in the far infrared and near infrared regions. The high absorption in the 6- to 9.5-μ region points to the need for an adequate thickness of low emittance surface coating to provide efficient radiation shields in the 300° to 700°K temperature range.

Total hemispherical emittances of a number of reflective shield materials were determined from integrated spectral reflectance data and/or calorimetric measurements. The reflectance measurements were performed with a heated cavity reflectometer and associated spectrophotometer (refs. 17 and 18) over the spectral range of 2.0 to 24.0 μ. Total hemispherical emittance measurements as a function of temperature were made by attaching specimens of the film material to a 2.54-cm-diameter cylinder and performing a heat balance with the internally heated cylinder radiating to a cold wall in a vacuum. The apparatus and method are described in Appendix B. Comparative values of a room temperature emittance were also obtained using a Lion Research Corp. Model 25-B Emissometer. The data on metals, using this device, are expected to be somewhat lower than the total hemispherical values because the instrument measures primarily the specular component. However, the device permits rapid measurements which may be used for comparative purposes. The emissometer was calibrated using an aluminum foil reference standard. A summary of the emittance data is presented in Table 4.

The total hemispherical emittance data for aluminum surfaces (Figure 34) illustrates the need to measure the material being used for shields. An empirical relationship between emittance and temperature for metals as a function of resistivity (ref. 20) was used to calculate the theoretical curve. Calorimetric measurements of dry annealed aluminum foil and adhesive-backed aluminum foil exhibit approximately the same slope with temperature but have significantly different values of emittance. These differences may be attributed to the aluminum alloy and the manufacturing and surface preparation processes. Similarly, the data for a pure aluminum cylinder (Figure 35) are consistently higher than the theoretical values. This is attributed to change in structure of the surface by the machining and polishing procedures. The vacuum-deposited aluminum coatings on 2.54 x 10^{-3} cm (1 mil) thick polyimide film (Figures 34 and 35) generally follow the same increase with temperature, but with higher values. The influence of aluminum thickness on emittance is not readily apparent from inspection of the data. A decrease in ϵ_T is observed for increasing thickness for coatings supplied by the same vendor. However, there is no consistency in emittance for a given coating thickness from different suppliers. This indicates that the deposition process and condition of the substrate may be as important as the coating thickness.

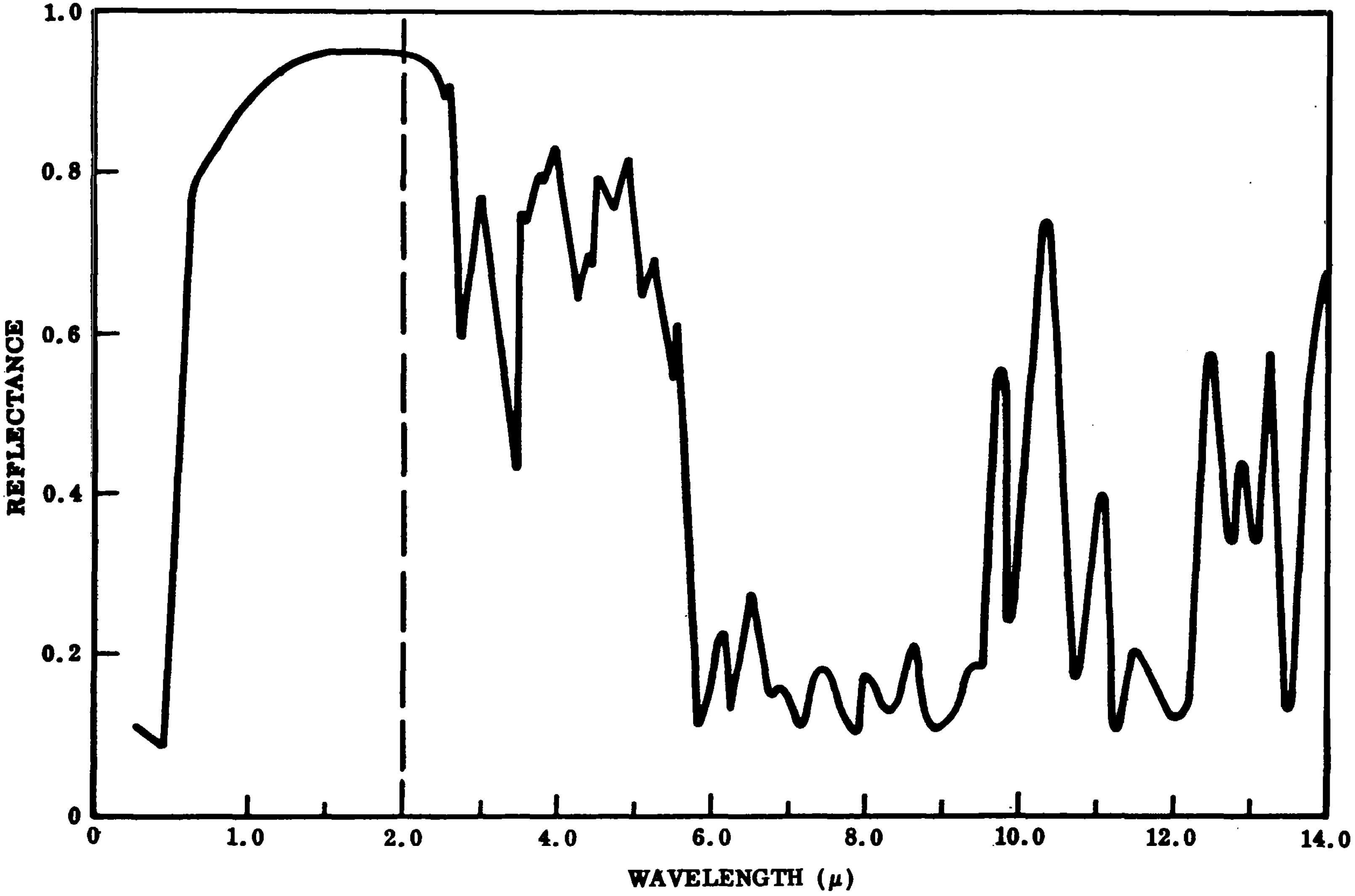

Figure 32 Spectral Reflectance of Uncoated Side of Polyimide Film (2.54 × 10^{-2} mm), Coated on One Surface With Aluminum

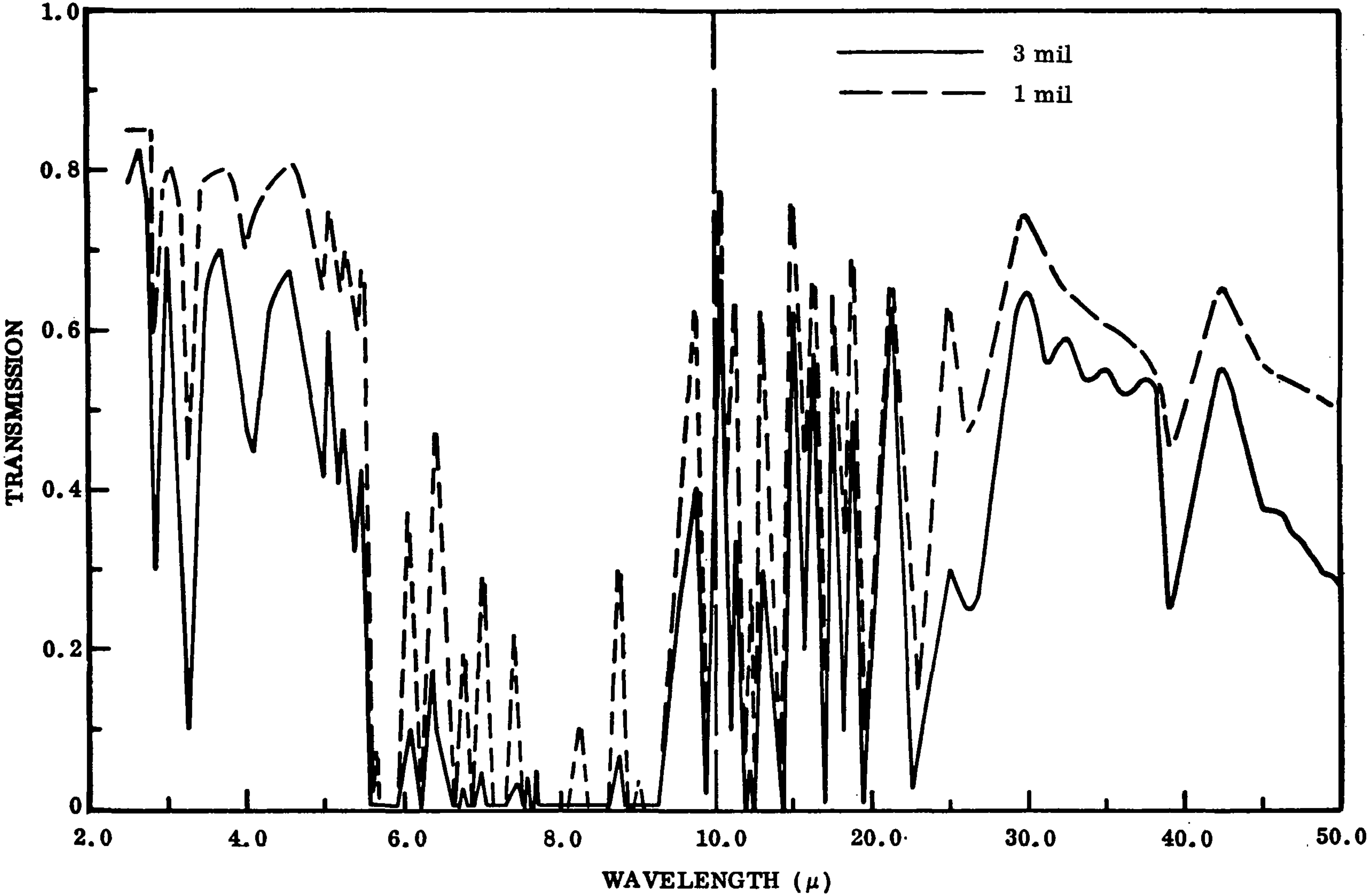

Figure 33 Spectral Transmittance of Polyimide Film

TABLE 4. – SUMMARY OF EMITTANCE DATA ON REFLECTIVE SHIELD

Material	Nominal coating thickness (Å)	Total hemispherical emittance at 300°K		Emissometer ϵ
		Calorimetric	Reflectance	
Aluminum foil, 1/4 mil	–	0.035	0.032	0.03
Type 316 stainless steel, bright finish	–	–	0.130	0.12
Vacuum deposited Aluminum on polyimide film[a]	2200 1000 850 650	0.044 0.036 0.040 0.052	0.028 0.024 0.025 0.026	0.04 0.04 0.04 0.04
Vacuum deposited Aluminum or polyimide film[b]	600 400	0.032 0.058	0.025 0.058	0.03 0.05
Vacuum deposited Aluminum or polyimide film[c]	700 300	0.046 0.080	0.042 –	0.04 0.07
Vacuum deposited Gold on polyimide Film	900 600 500	0.040 0.038 –	0.017 0.016 0.017	0.03 0.03 0.03
Vacuum deposited gold on polyimide[c]	d d	0.034 0.051	0.020 –	0.02 –
Chem. deposited gold on polyimide film[e]	200 to 800	0.059	–	0.05
Vacuum deposited silver on polyimide film[a]	700 500 400	0.040 – –	0.017 0.018 0.021	0.04 0.03 0.04
Vacuum deposited silver with SiO4 overcoating on polyimide film[f]	d	0.035	0.035	0.03

[a] D. L. Clausing Company
[b] NRC Corporation
[c] McCordi Metallizing Corporation
[d] Coating thickness not known
[e] Reflective laminates
[f] Schjeldahl

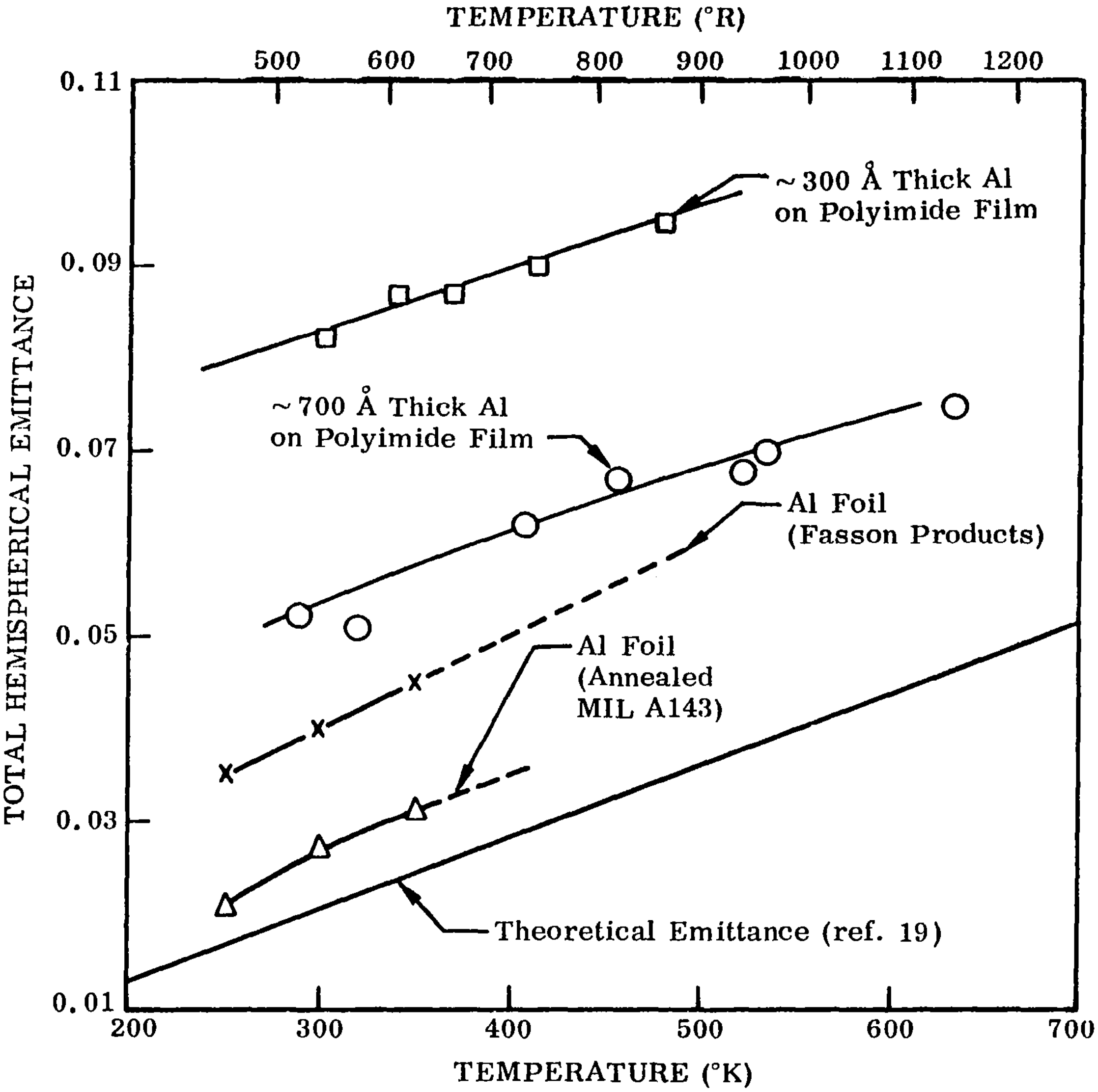

Figure 34 Total Hemispherical Emittance of Several Aluminum Surfaces as a Function of Temperature. (Numbers represent order of data point)

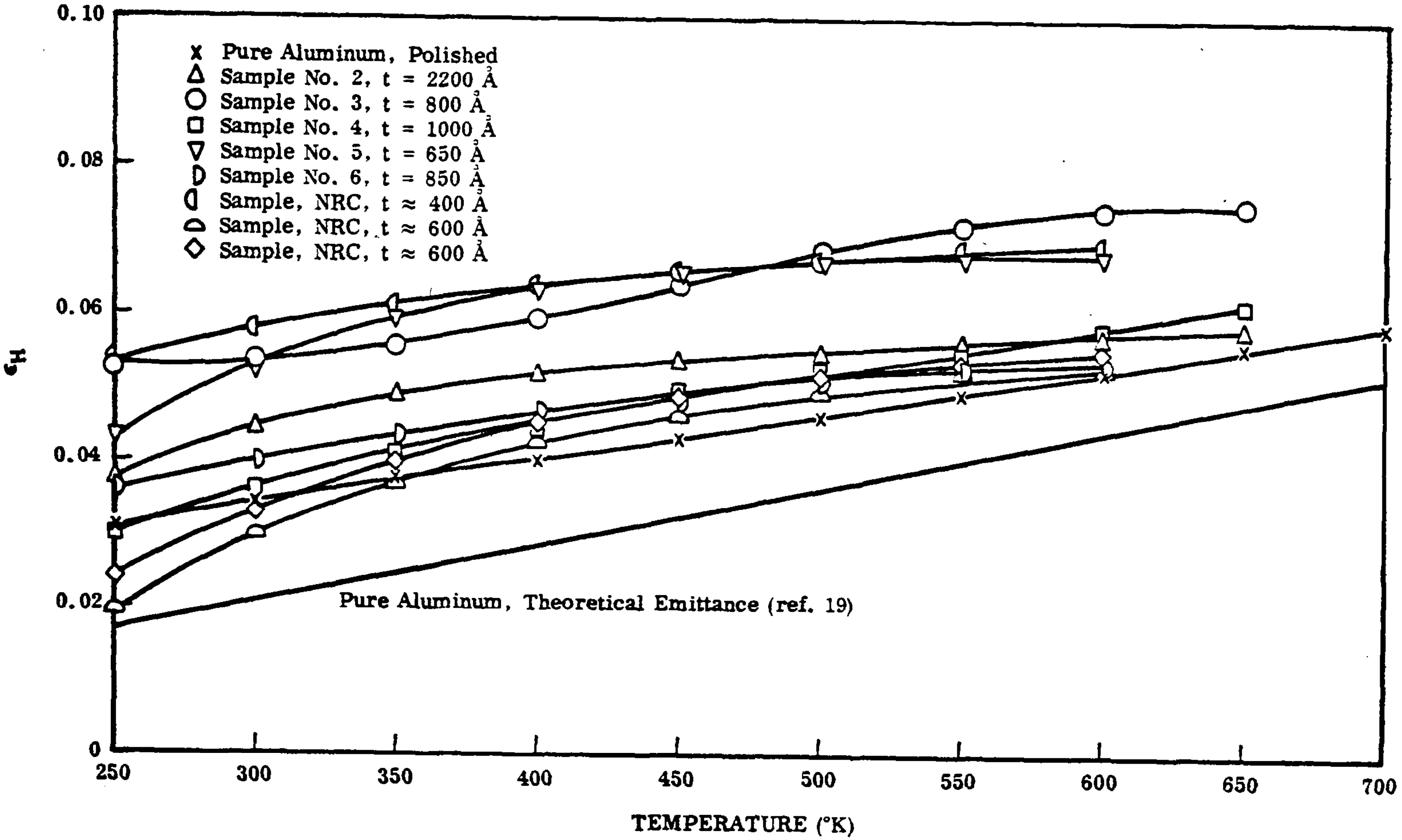

Figure 35 Total Hemispherical Emittance of Aluminum and Aluminum-Coated Polyimide Film Samples

Data from specimens prepared by the same vendor using 99.99% pure aluminum showed a wide variation in ϵ_T at a thickness of 800 Å. One specimen which appeared granular under electron microscope examination had a total hemispherical emittance of 0.053 at 300°K while a second specimen of 850 Å thickness showed an ϵ_T of 0.040. The resistivity measurements on the former also showed a poor coating based upon its electrical characteristics. Likewise a 2000 Å coating had an emittance of 0.044 and exhibited a higher resistance than one would expect for this thickness. For the three specimens on which good correlation with resistance determination of thickness was obtained, an increase of emittance of from 0.036 to 0.052 was measured for thicknesses decreasing from 1000 Å to 650 Å.

Vacuum-deposited 99.999% pure silver coatings (Figure 36) did not result in the decrease in emittance compared to aluminum that was expected from the theoretical values for pure metals. Although no visual defects were noted in coating appearance, silver films are very sensitive to structural changes and present problems in some evaporation techniques (ref. 20).

The relatively high values of emittance achieved on the polyimide film for aluminum, gold, and silver (Figures 34 through 37), as well as the variation between suppliers, are attributed to coating techniques. Although specifications on the material were made in terms of resistivity, it appears that control of the thickness is not the only important consideration. The deposition process and quality of the substrate surface are also important. Coated polyimide film is commercially available for use as reflective shields having a total hemispherical emittance of 0.03 to 0.06 over the temperature range of 300° to 700°K. Unless improvements are made in processing techniques, coating thickness of 600 Å to 800 Å are sufficient to achieve these levels of emittance.

5.1.2 Spacer Materials

Absorption and scattering coefficients of the various spacer materials were measured to provide data for the analysis of the experimental thermal conductivity data and for the study of the radiation heat-transfer mechanism. The technique consists of measuring the transmission of several thicknesses of each material. Measurements are performed with the specimens at room temperature and at angles from normal to 60 deg from normal. Spectral data are obtained over the wavelength range from 1.5 to 15 μ by using a 1700°K source in conjunction with a Perkin-Elmer Model 98 monochrometer. A description of the apparatus is presented in Appendix C. The absorption and scattering coefficients, a and s, respectively, are calculated from the transmission data as a function of thickness using the expressions developed in ref. 14. The materials considered for spacer materials and the experimental values of absorption and scattering coefficients are given in Table 5.

Spectral and total transmission measurements were made for one-, two-, four-, and eight-layer thicknesses of the borosilicate glass spacer materials. Angular data were also measured to determine spatial distribution of the energy scattered in the forward direction. The angular distribution varied considerably with thickness out to 60 deg from normal. The single-thickness material exhibited predominantly normal transmission and the four-layer material exhibited maximum transmission from 20

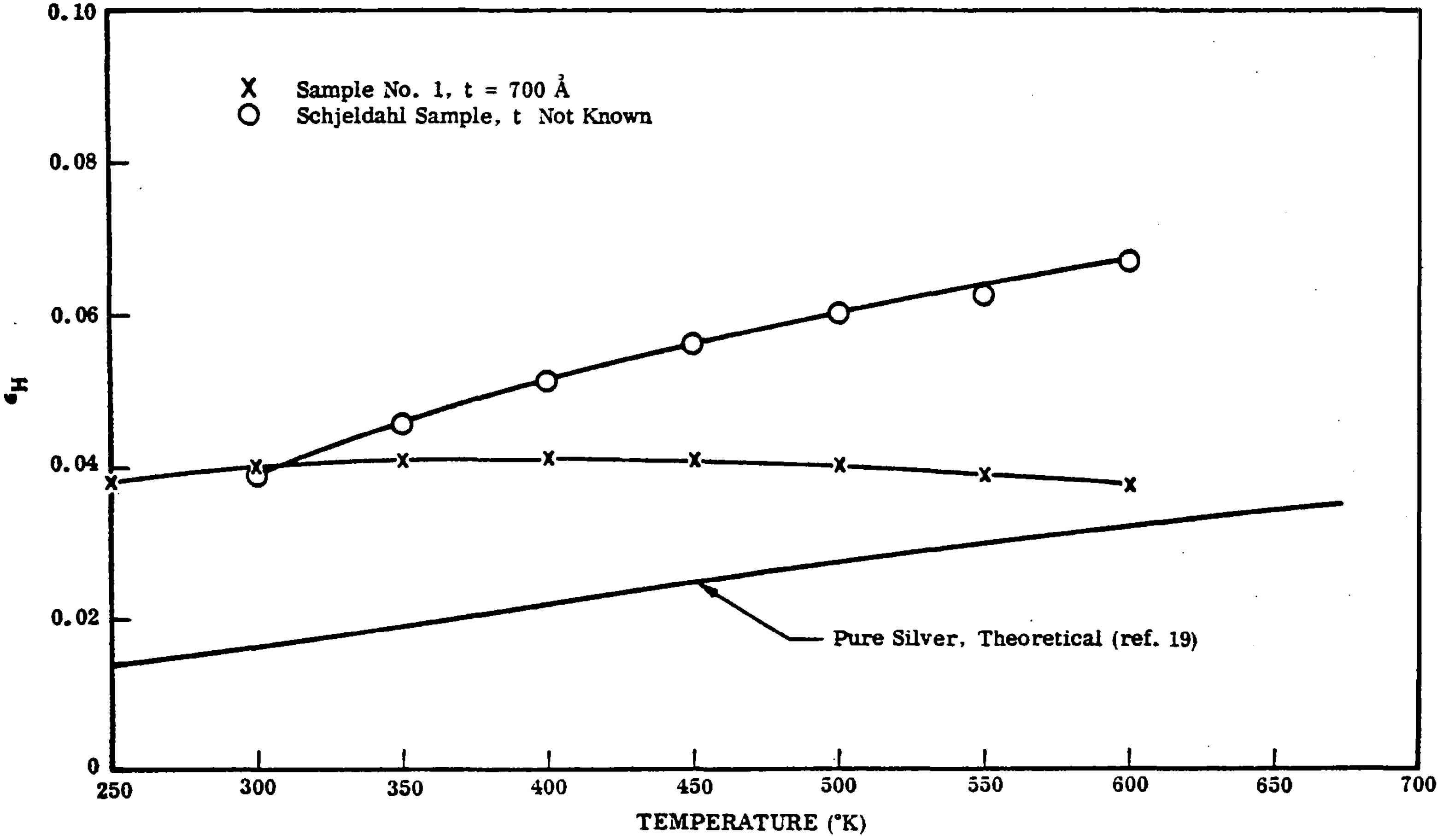

Figure 36 Total Hemispherical Emittance of Silver-Coated Polyimide Film

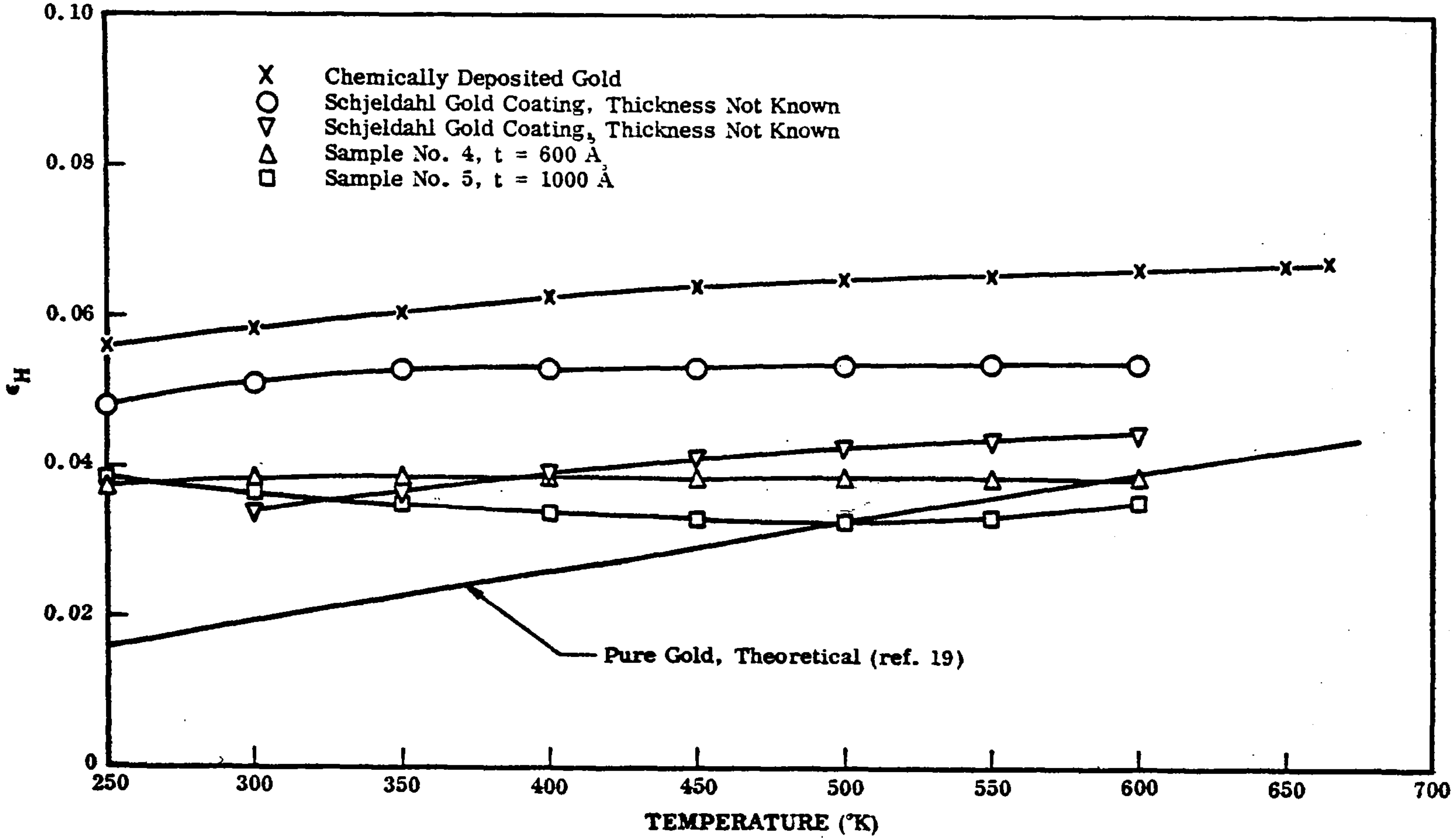

Figure 37 Total Hemispherical Emittance of Gold-Coated Polyimide Film Samples

TABLE 5. – ABSORPTION AND SCATTERING COEFFICIENTS FOR SEVERAL SPACER MATERIALS AS A FUNCTION OF SOURCE TEMPERATURE

Material	Supplier	Source temperature (°K)	Absorption coefficient (cm^{-1})	Scattering coefficient (cm^{-1})
Glass-fiber paper (nominal fiber diameter < 1 μ), 7.6×10^{-2} mm thickness	C. H. Dexter Co.	500	13	260
		650	11	270
		800	11	280
		1000	7	310
		1700	6	250
Glass-fiber paper (nominal fiber diameter < 1 <), 1.5×10^{-2} mm thickness	Amflex Prod. Div. AMF	500	3	265
		650	11	280
		800	11	300
Silica-fiber felt (nominal fiber diameter 10 μ)	H. I. Thompson	500	< 2	33
		650	< 2	50
		800	< 2	71
		1000	< 2	74
Silica fiber felt (nominal fiber diameter, 1.3 μ)	H. I. Thompson	500	< 2	38
		650	< 2	57
		800	< 2	73
		1000	< 2	76
Carbon fiber paper (nominal fiber diameter, 10 μ)	H. I. Thompson	775	4	385
		923	2	260
		1123	2	185
		1273	4	200

to 30 deg from the normal. All specimens showed significant deviations from a cosine distribution. Total transmission was calculated from measurements of total energy collected over 20 percent of the forward hemisphere. Spectral transmission measurements for the wavelength region from 1.5 to 15 μ showed absorption bands in the 6.0- to 9.0-μ region. Similar measurements were performed with the two Refrasil specimens and the graphite cloth material. The graphite cloth showed a spectrally flat transmission at about 2% over the 1.5- to 15-μ region for a single thickness. The Refrasil materials exhibited a transmission band from 6 to 8 μ but at other wavelengths in the 1.5- to 15-μ region the spectral transmission was less than 0.5 percent for the 4.83 mm thickness material. No significant differences were detected in transmission or angular distribution for the two fiber diameters measured. The spatial distribution of transmitted energy for this material does not follow a cosine distribution.

A summary of the optical property measurements is given in Table 5. Values of absorption and scattering coefficients were calculated from total transmission data as described in Appendix B. The glass-fiber and carbon fiber papers presented the largest scattering coefficients. A portion of the difference between the values of s for the glass and silica fibers is due to the greater number of scattering centers per unit volume. Significant differences in scattering and absorption coefficients were noted for thin layers. The reported data are based on the greater thicknesses. The glass paper scattering coefficient is approximately 40% larger when based on transmission data for one and two thicknesses.

Uncertainties in thickness measurement and spatial distribution of energy, and the errors associated with measurement of very low values of transmission result in an estimated maximum uncertainty of 50% for the reported coefficients. Other investigators (ref. 6) reported scattering coefficients for the glass paper which are less than the values reported herein. Variations in experimental apparatus for measuring nonisotropic scattering materials and inhomogeneities in the material itself probably contribute significantly to these differences.

Effective thermal conductivity measurements for spacer materials were performed in vacuum (10^{-4} Torr or less) as a function of bulk or layer density and hot boundary temperature. A cold boundary temperature of 273°K was used for all materials. A flat plate type of apparatus, described in Appendix D, was used for all of the experimental measurements. Heat flux is determined calorimetrically by measurement of boiloff flow rates using liquid butane and nitrogen as the calorimetric fluids.

Two submicron-size glass fiber papers and two high-purity silica fiber batt-type materials were investigated. A description of these materials is contained in Table 6. Effective thermal conductivities of the two silica fiber materials are shown as a function of hot boundary temperature in Figure 38. The A-100 material (1.3-μ-diameter fiber) is superior to the 10-μ-diameter fiber material (B-100) as an insulator. Neither type of silica fiber material showed as low a conductivity as the submicron-size fiber papers at a comparable density. Data for Dexiglas and Tissuglas papers are presented in Figures 39 and 40 for a number of densities. Both of these materials show the same thermal conductivity at equivalent densities as illustrated by Figure 41. This was expected because both are composed of submicron fibers and the scattering coefficients were nearly the same. Thermal conductivity of the insulation composed of paper-like materials is less than one-half of that for the silica fiber materials. Qualitatively, this reduction may be ascribed to the greater scattering coefficients of the former materials. The ratio of conductivities is less than the scattering coefficient ratio, but the absorption properties of the papers are greater than those of the silica fiber.

The paper-like materials are the better choice for a multilayer spacer because they are thin and permit a larger number of reflective shields per cm without large compressive forces which increase the solid conduction. Similarly, Tissuglas appears to be more promising than Dexiglas as it is approximately one-fifth the thickness of the latter. The Tissuglas and Desiglas materials are also useful as an intermediary insulation. This is a more nearly thermally isotropic material utilized to

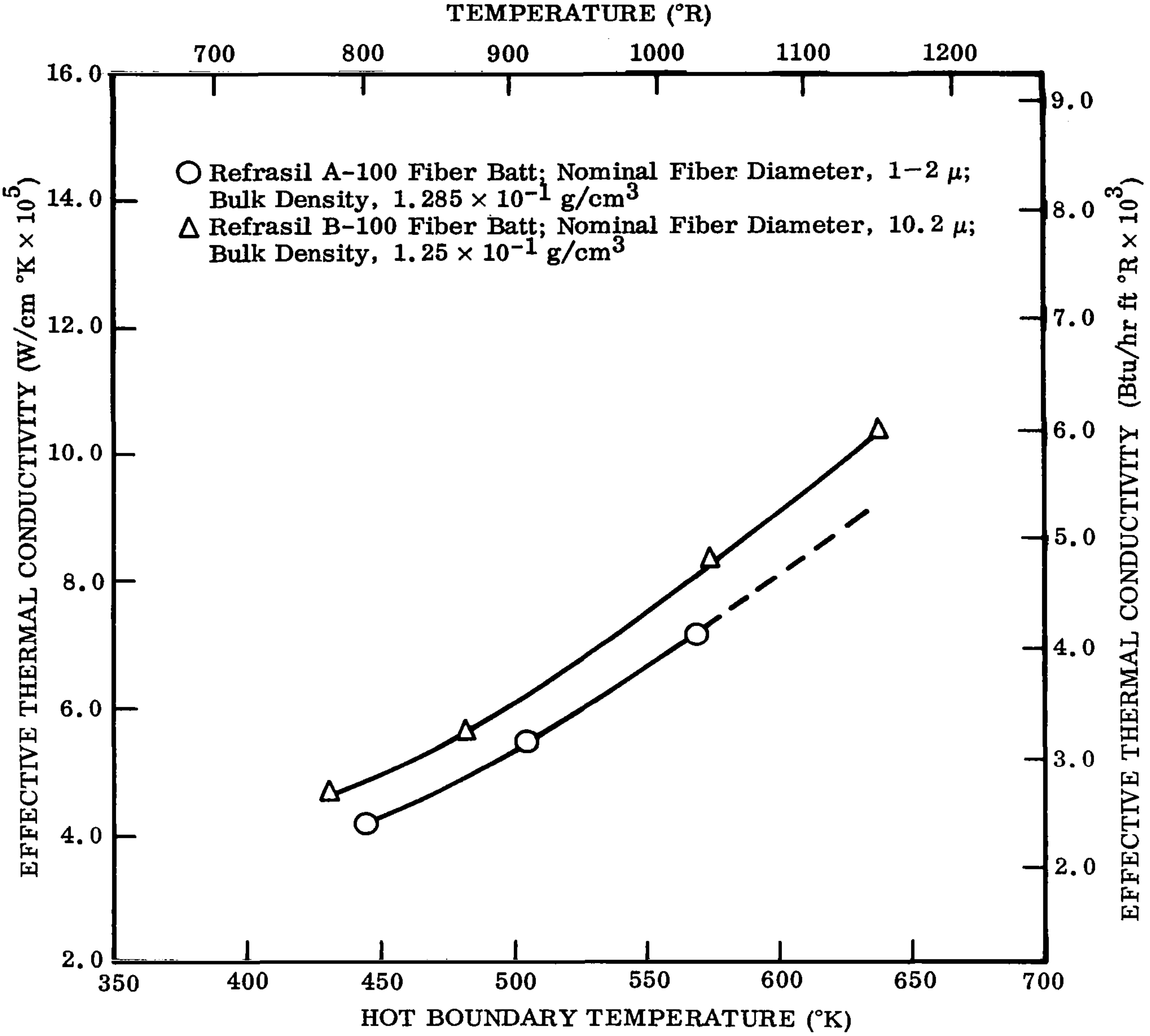

Figure 38 Effective Thermal Conductivity of Refrasil Spacer Material as a Function of Temperature and Fiber Diameter

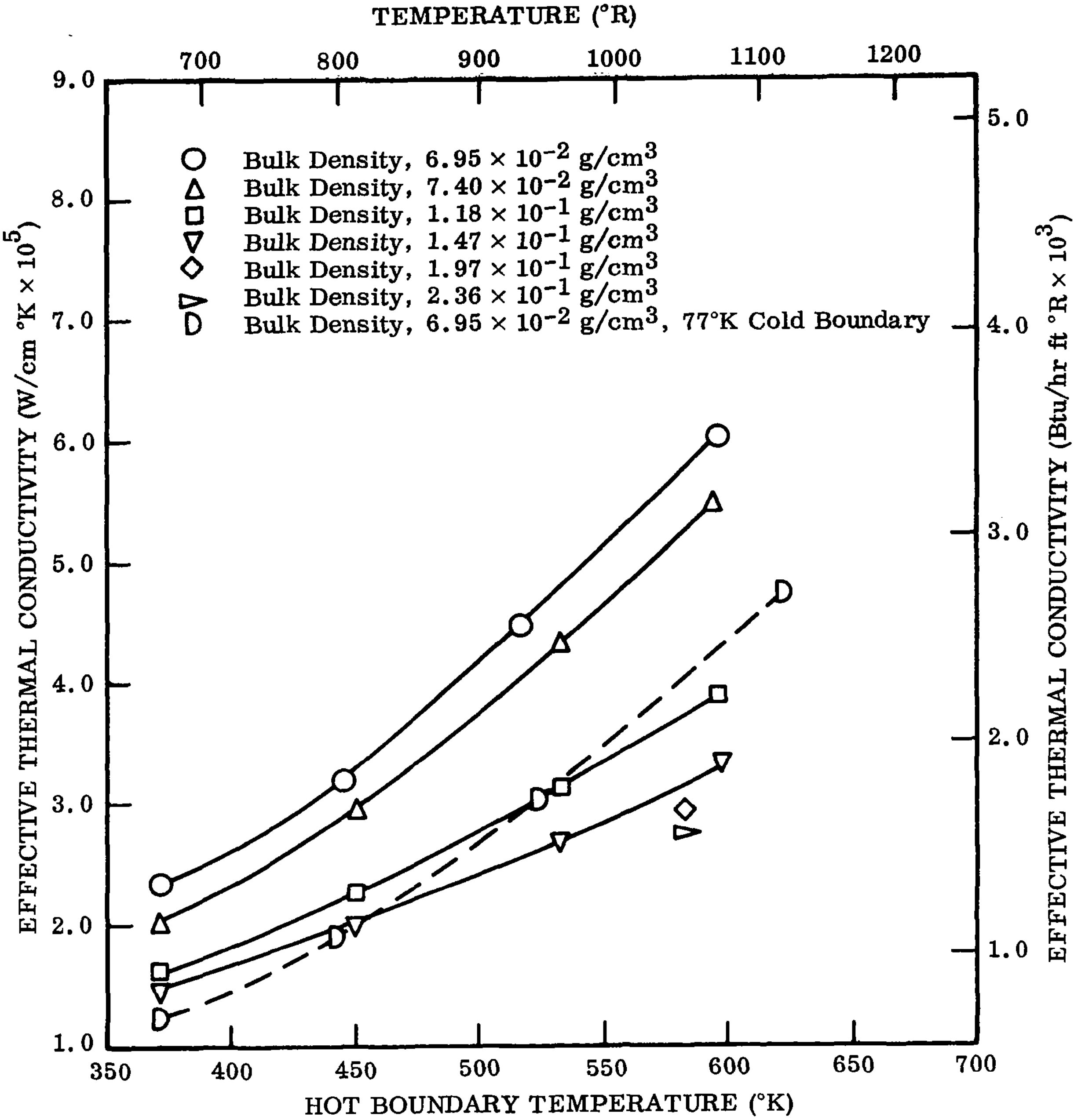

Figure 39 Effective Thermal Conductivity of Dexiglas Spacer Material as a Function of Temperature and Density

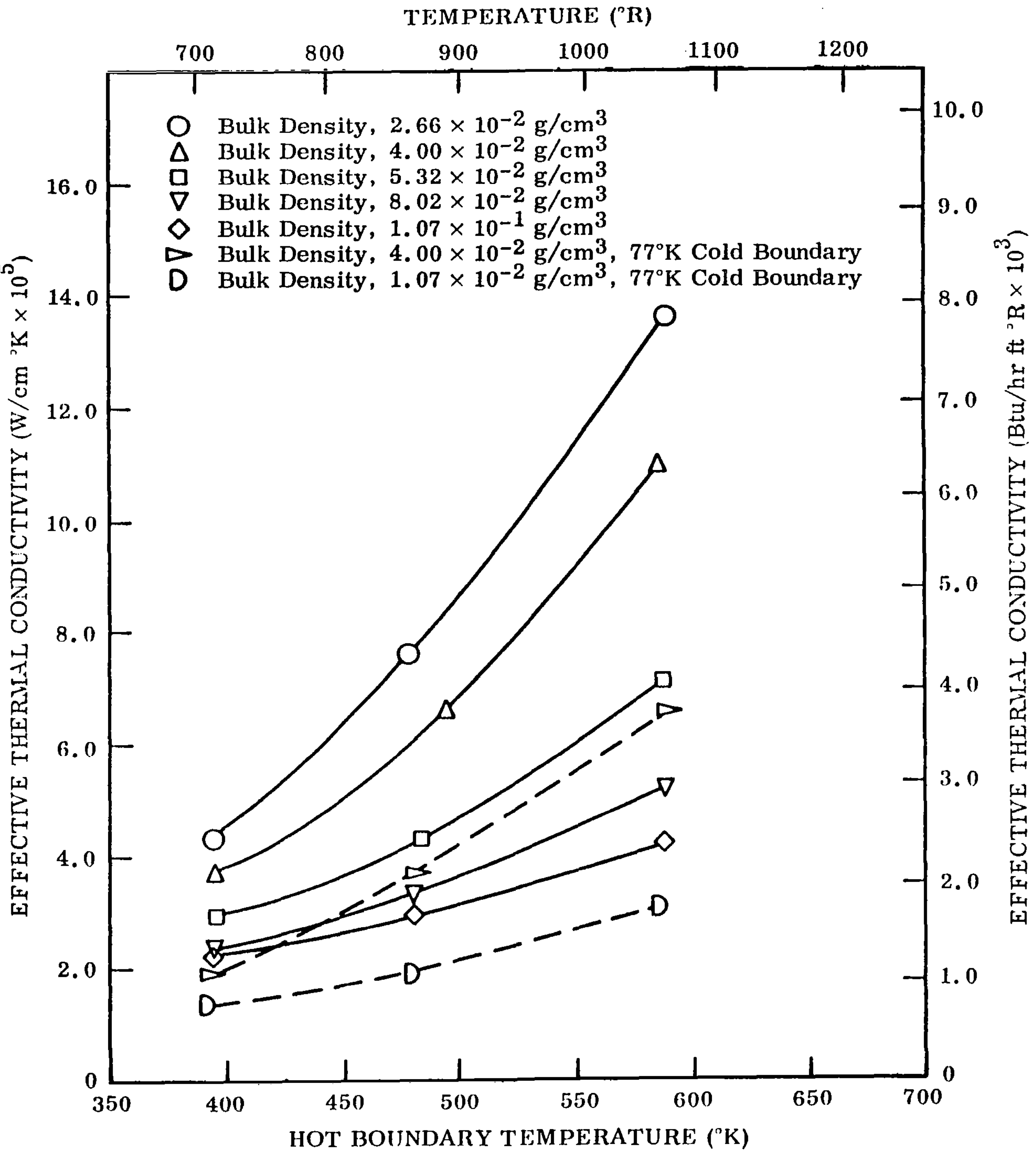

Figure 40 Effective Thermal Conductivity of Tissuglas Spacer Material as a Function of Temperature and Density

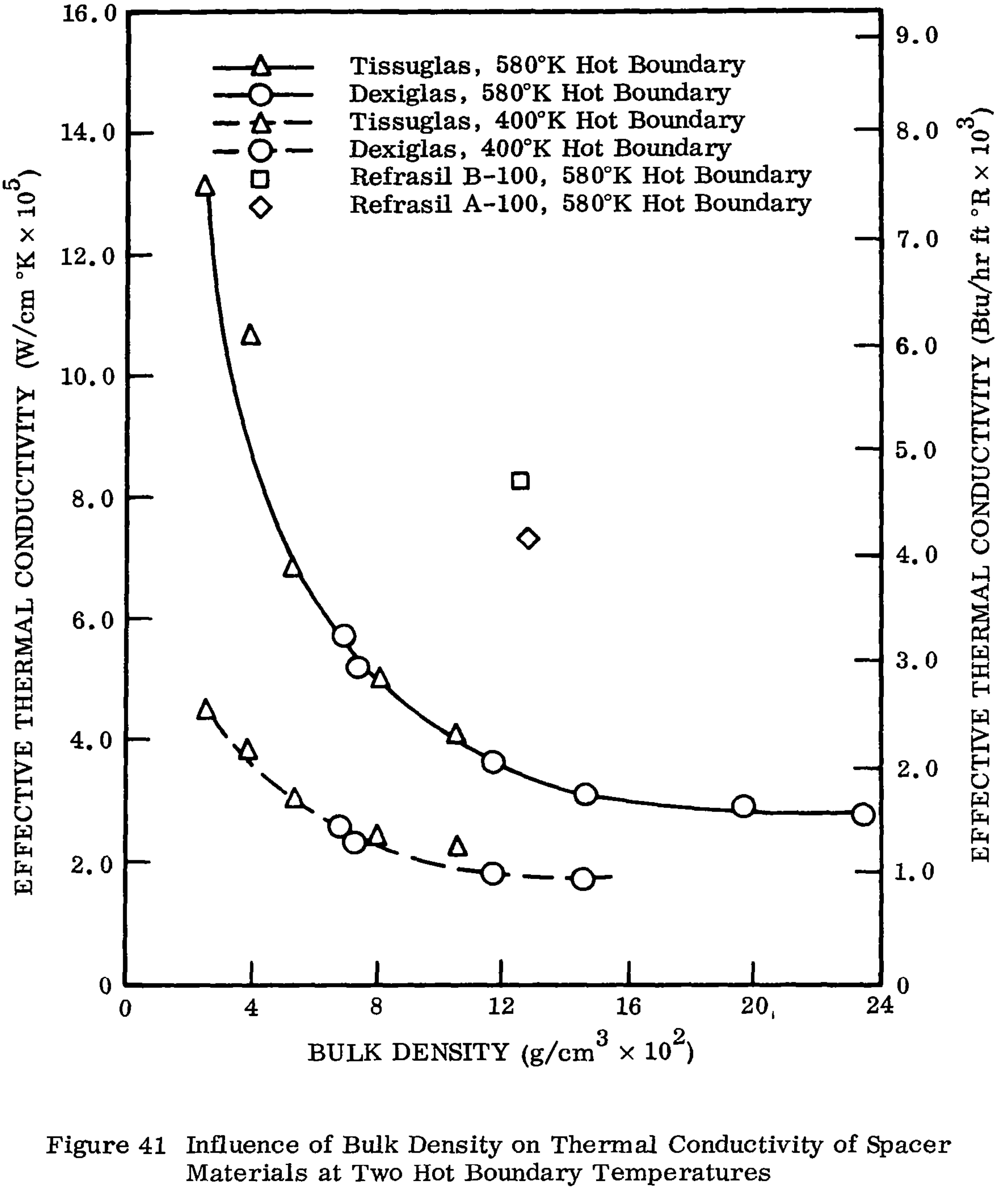

Figure 41 Influence of Bulk Density on Thermal Conductivity of Spacer Materials at Two Hot Boundary Temperatures

TABLE 6. – DESCRIPTION OF SPACER MATERIALS

Material	Source	Nominal density (g/cm^3)	Thickness (mm)	Fiber diameter (mm)	Specific weight (kg/m^2)
Dexiglas (borosilicate glass)	C. H. Dexter & Sons Paper Co.	2.0×10^{-1}	7.62×10^{-2}	$< 10^{-3}$	1.54 × 10-2
Tissuglas (borosilicate glass)	Amflex Prods. Div, AMF[a]	2.2×10^{-1}	1.52×10^{-2}	$< 10^{-3}$	3.4×10^{-3}
Refrasil A-100 (99% SiO_2)	H. I. Thompson Co.	5×10^{-2}	4.83	1.3×10^{-3}	2.5×10^{-1}
Refrasil B-100 (99% SiO_2)	H. I. Thompson Co.	5×10^{-2}	4.83	1×10^{-2}	2.5×10^{-1}

[a] Current source is Pallflex Corporation.

prevent lateral conduction from the anisotropic multilayer to disturbance such as penetration or exposed edges in the insulation system.

5.2 MULTILAYER INSULATION PERFORMANCE TESTS

Effective thermal conductivities of seven different composites were measured in vacuum (5×10^{-5} Torr or less) as a function of hot boundary temperature for a 273°K cold boundary. The systems included stainless steel and aluminum and gold-coated polyimide film reflective shields and spacers of Dexiglas, Tissuglas, Refrasil, and graphite cloth. Also, one system was tested which did not include spacers, but rather had detents formed into the shields to maintain their spacings. Conductivity was also measured as a function of density for a 77°K cold boundary for several composites. The flat plate apparatus, Appendix D, was used for all measurements.

Data for a multilayer insulation composed of 30 layers of aluminized polyimide film (0.0254 mm thick) with 0.0762-mm Dexiglas paper spacers is shown by Figure 42. At a 600°K hot boundary temperature, conductivity was measured at layer densities of 24, 28, and 32 layers/cm. The minimum in conductivity is observed to

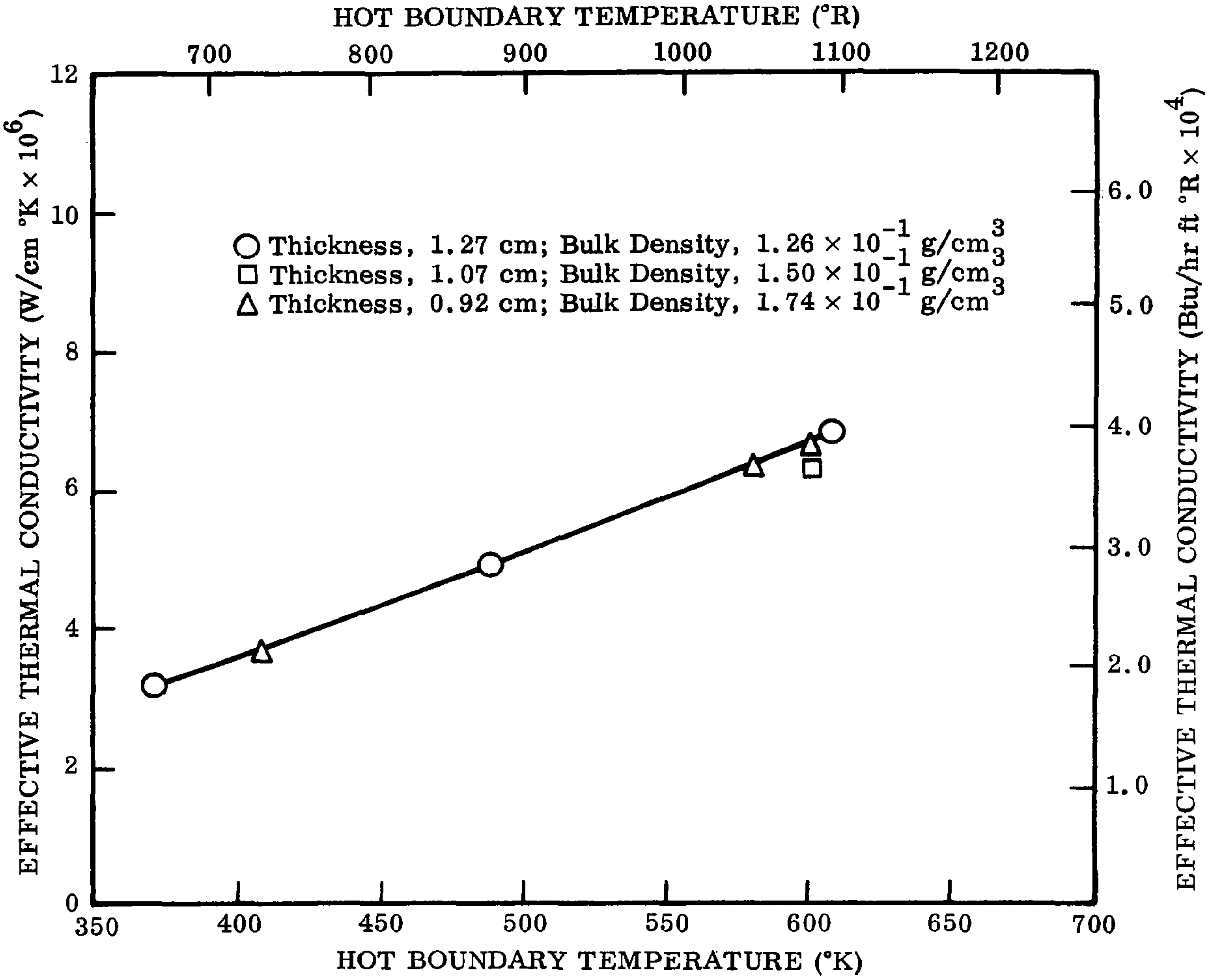

Figure 42 Effective Thermal Conductivity of an Aluminized Polyimide Film/ Glass Paper Multilayer Insulation System Having 30 Shields With 7.6×10^{-3} cm Thick Spacers

occur at a layer density of 28 to 30 layers/cm, and this value is 6.5×10^{-6} W/cm °K. Two additional insulations composed of the aluminized polyimide shields and Dexiglas spacers were measured at several densities (Figures 43 and 44). At 600°K the minimum conductivity of the insulation using the 0.23 mm thick spacer was 8.2×10^{-6} W/cm °K, and that of the insulation having 0.38 mm thick spacers was 8.5×10^{-6} W/cm °K. The greater conductivity of both these insulations, compared to that of the 0.076-mm spacer material, is attributed to the increase in solid phase conduction and absorption caused by the thicker spacers. At a layer density of 20 layers/cm, conductivities are approximately 7.5×10^{-6} W/cm °K for the insulation using the thinest spacer material and 8.8×10^{-6} and 12×10^{-6} W/cm °K for the successively thicker spacers. The minimum in conductivity occurred at approximately 8 layers/cm for the 0.38 mm spacer and 10 layers/cm for the 0.23 mm spacer. A minimum density times conductivity product for the Dexiglas-aluminized film system occurs for a 0.23 mm spacer material. Figures 43 and 44 illustrate the influence of edge boundary temperature on the measured conductivities using the flat plate apparatus. For the thicknesses tested, the two-dimensional heat-transfer effects are less than 5%.

The effects on conductivity of variations in shield and spacer material are shown by Figure 45. The importance of shield emittance is illustrated by comparing the data for two systems using the same spacer with stainless steel and aluminized polyimide film shields (Figure 42). Doubling the emittance increased the effective conductivity by approximately 80%. The graphite cloth spacer resulted in a very high effective thermal conductivity, approximately six times that obtained with the Dexiglas spacer material, illustrating the effect of a highly absorbing spacer media.

The thermal conductivity of a commercial multilayer system, as a function of hot boundary temperature, is shown by Figure 46. The system was composed of polyimide reflective shields having a chemically deposited gold coating and a batt type of fibrous spacer material similar in appearance to Refrasil but much thinner. The conductivity is approximately 20% higher at 600°K than that measured for an aluminized polyimide film-Dexiglas composite at a comparable density. This higher conductivity is due principally to the emittance of the chemically deposited gold shields, the emittance of which was 20% higher than that of the aluminized material.

The thermal performance of a system using Tissuglas spacers with aluminized polyimide film shields was investigated as a function of layer density and boundary temperatures. The data are shown graphically by Figure 47. Using a single layer of Tissuglas for each spacer (0.0152 mm thickness), conductivity was measured at layer densities of 24, 30, 47, and 59 layers/cm. The density corresponding to minimum thermal conductivity lies in the range of 60 to 65 layers/cm for a 273°K cold boundary temperature and hot boundary temperature to 600°K. However, for a cold boundary temperature of 77°K, the optimum layer density appears to be in the vicinity of 50 layers/cm (Figure 47). Conductivity as a function of layer and bulk densities is shown in Figure 48 for three hot boundary temperatures. The minimum $k\rho$ product for this system at 575°K is 1.5×19^{-7} W/cm °K-g/cm^3 at a layer density of 24 layers/cm. A second test was conducted using the same radiation shields, but

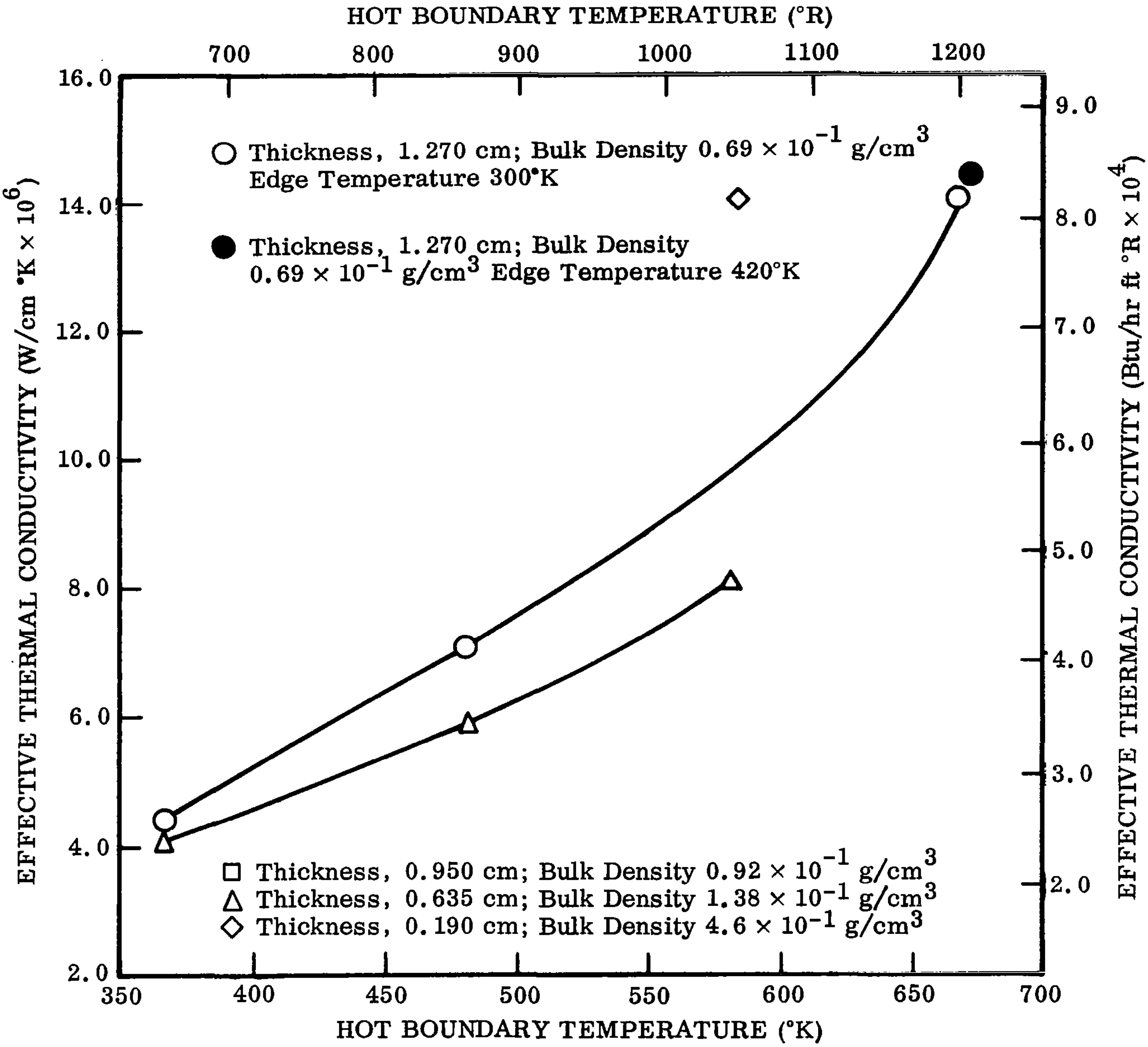

Figure 43 Effective Thermal Conductivity of Aluminized Polyimide Film Dexiglas Multilayer System as a Function of Temperature and Bulk Density; Spacer Thickness 2.3×10^{-2} cm Uncompressed; 10 Shields

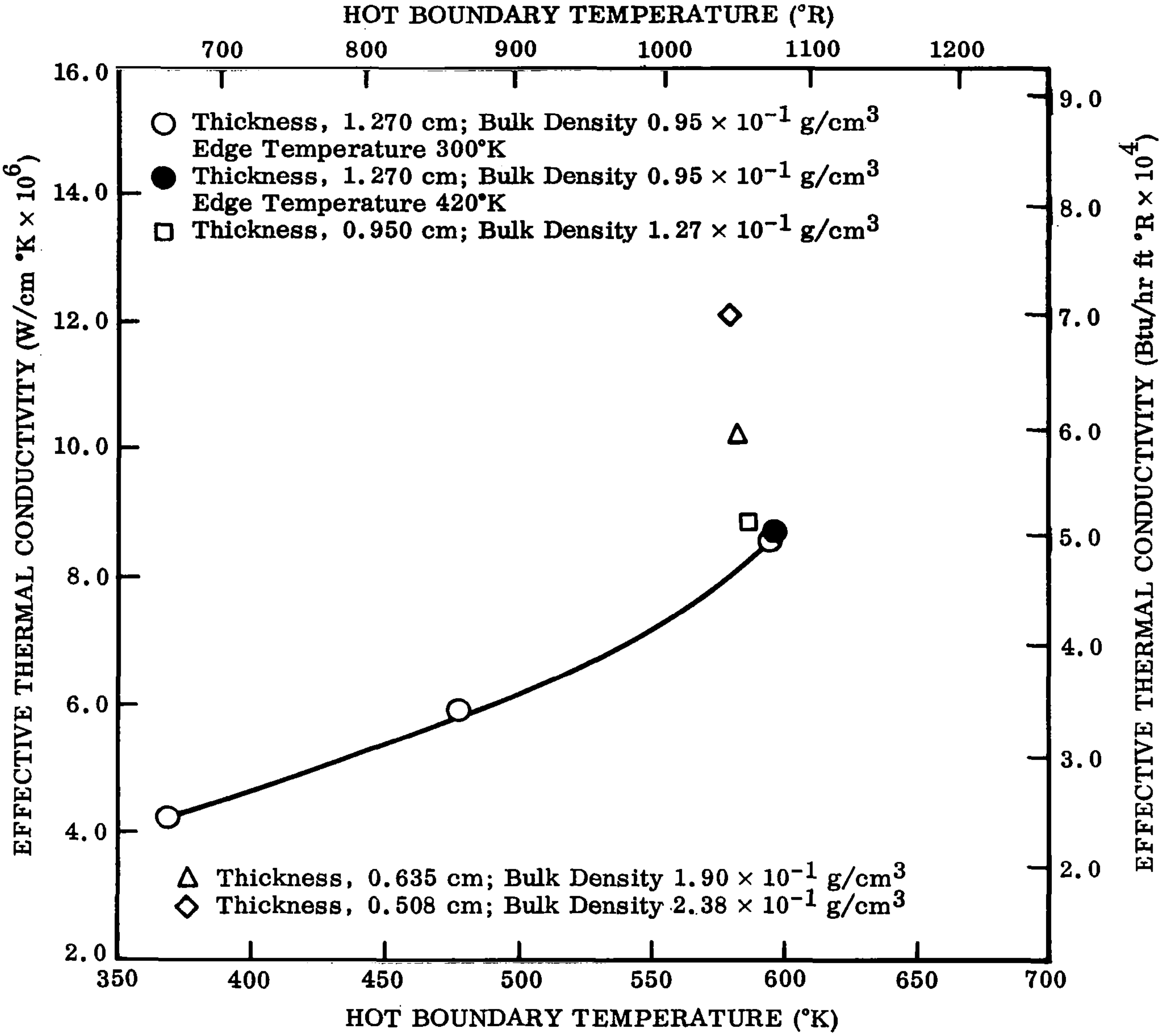

Figure 44 Effective Thermal Conductivity of Aluminized Polyimide Film Dexiglas System as a Function of Temperature and Bulk Density; Spacer Thickness 3.8×10^{-2} cm; 10 Shields

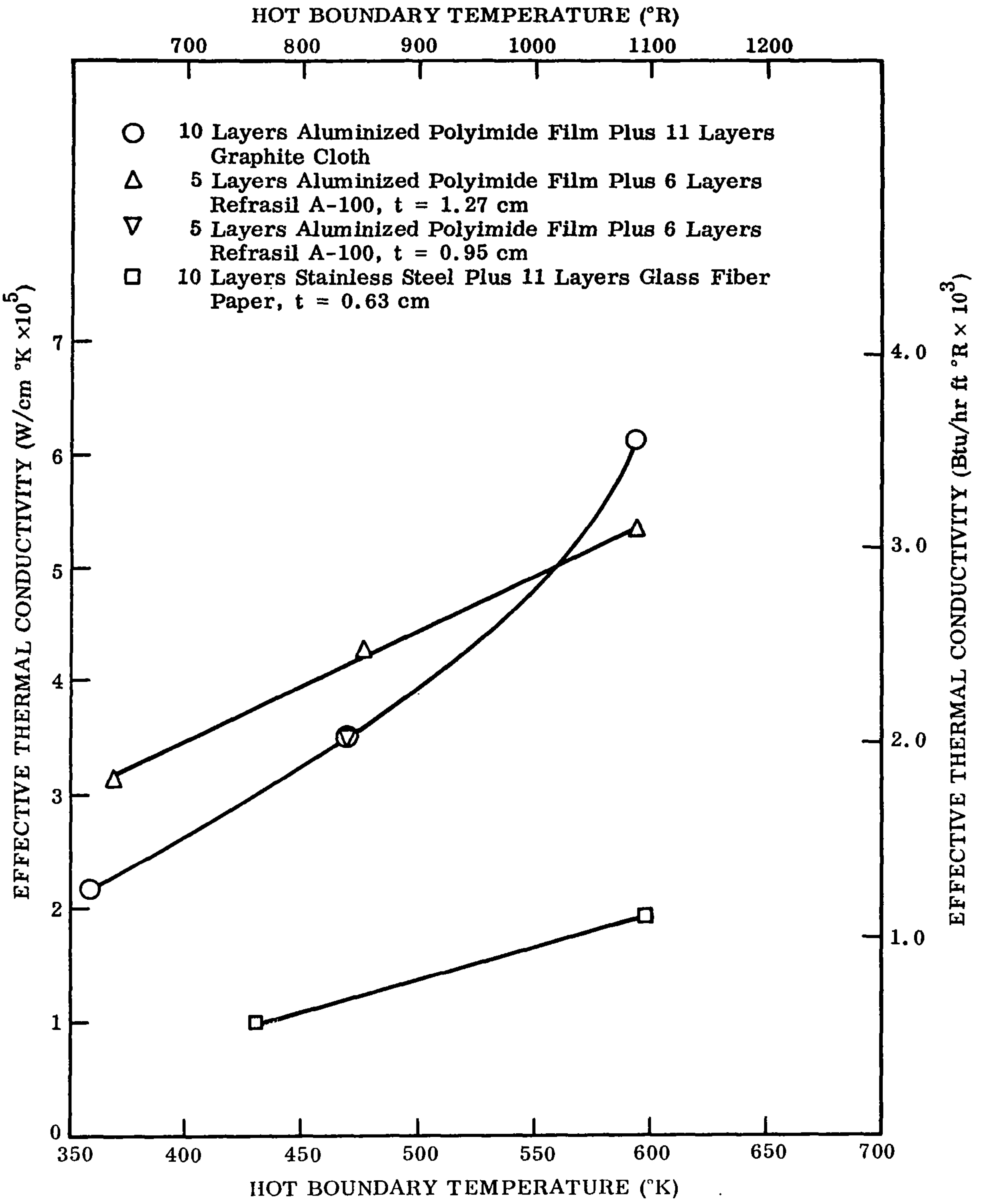

Figure 45 Effective Thermal Conductivities of Several Combinations of Shield and Spacer Materials

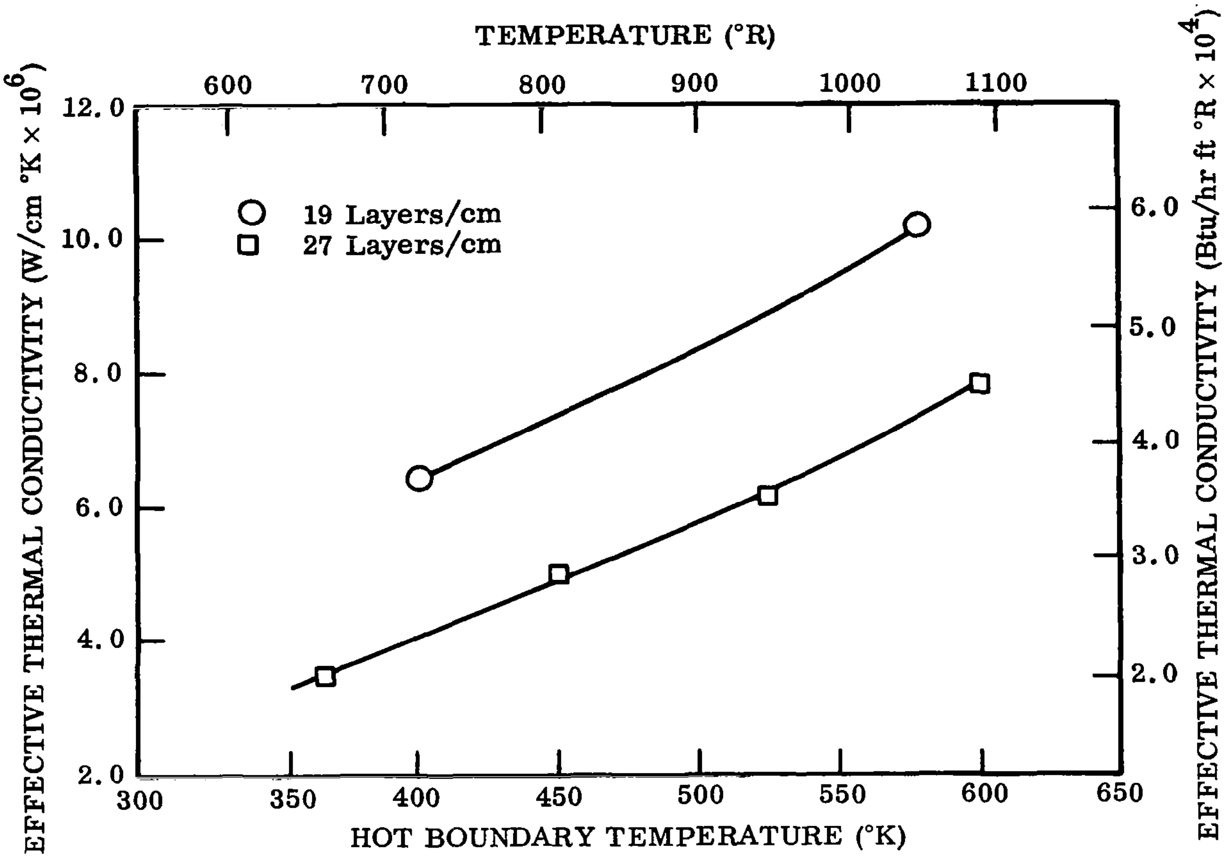

Figure 46 Effective Thermal Conductivity of Gold-Coated Polyimide (Chemical) – Fiber Batt, Multilayer Insulation

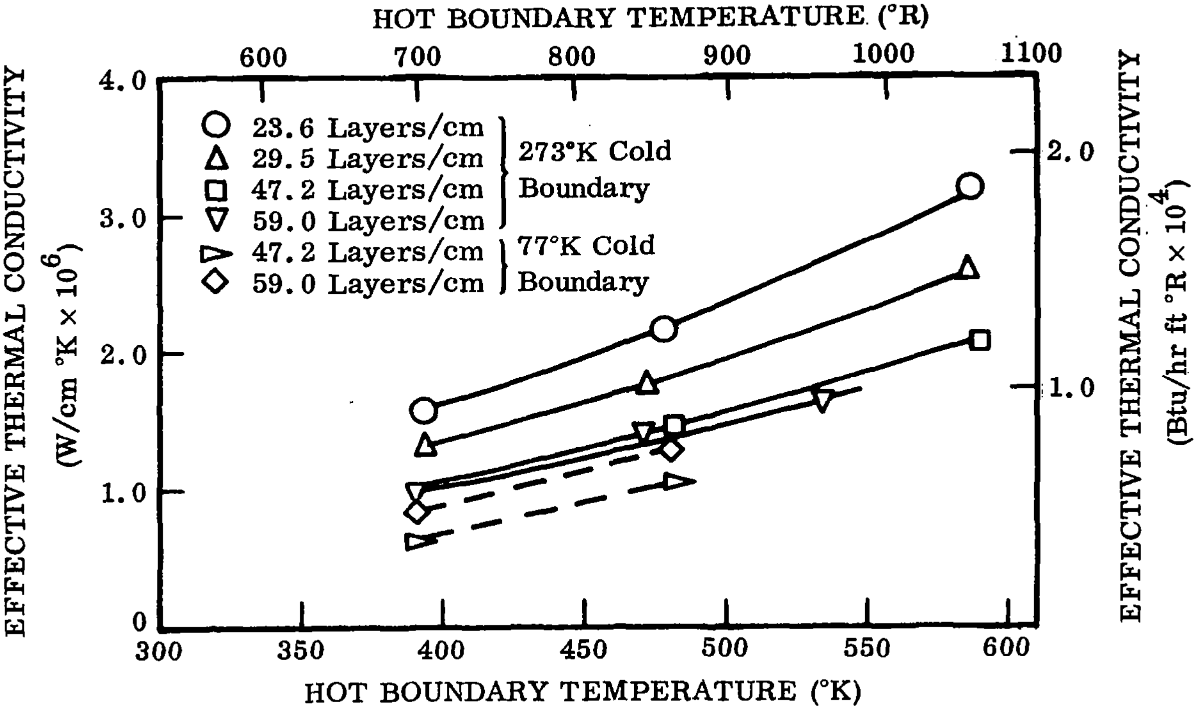

Figure 47 Effective Thermal Conductivity of Aluminized Polyimide Film and Tissuglas Multilayer Insulation

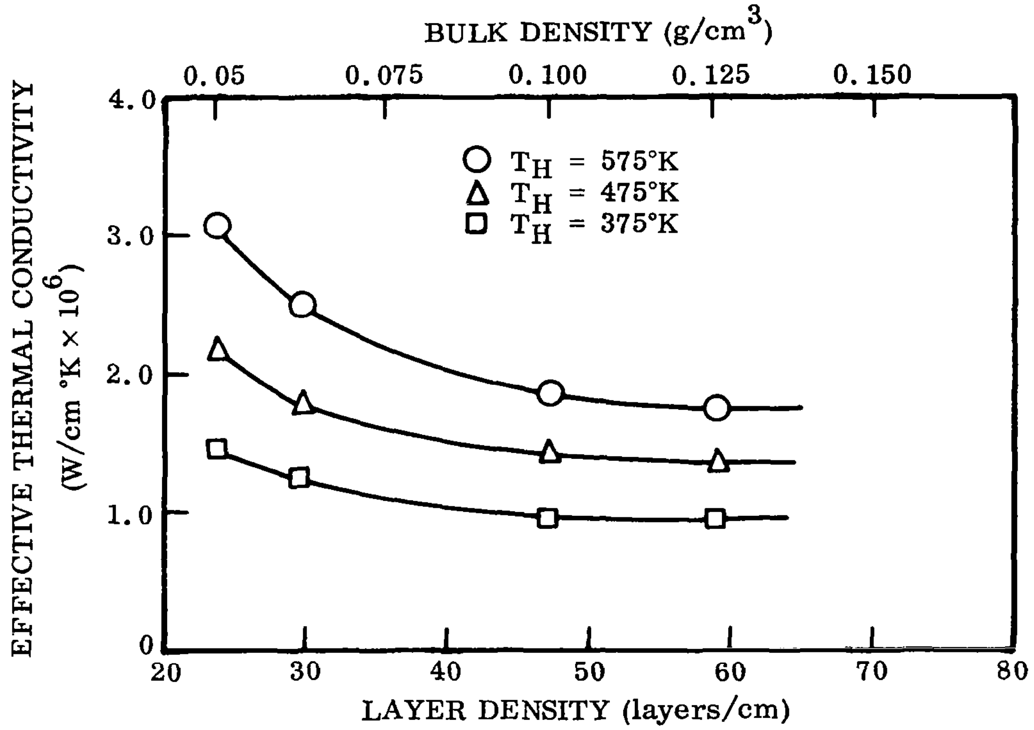

Figure 48 Effective Thermal Conductivity of Aluminized Polyimide Film and Tissuglas as a Function of Layer Density and Bulk Density

each spacer layer consisted of four thicknesses of the Tissuglas paper. This was done to evaluate the influence of spacer thickness and obtain comparative data with the Dexiglas material of approximately the same thickness. The thicker spacer resulted in a conductivity approximately twice that measured for the single layer spacers at equal layer densities. Also, the conductivities of the Dexiglas insulation system and the four layers of Tissuglas were nearly equal. The increase in conductivity with the thicker spacer is greater than one would estimate from considerations solely of the solid conduction term. It appears to be more nearly coupled with the large absorption of the thicker material.

The final insulation system tested was made up of reflective layers only. The spacers were detents formed into the polyimide film. They measured approximately 1.5 mm deep by 3 mm long by 1.5 mm wide and were located on 1-cm centers. Thermal conductivity for four layer densities is shown by Figure 49. In comparison with the Tissuglas spacer at comparable layer densities, the dimpled system has a conductivity approximately 15% greater than that with the paper spacer which indicates the dimpling results in a slightly higher solid conduction term. Figure 50 illustrates the effect of layer density on conductivity for a 535°K hot boundary temperature. This system is more efficient on a $k\rho$ basis than the optimum shield-spacer combination shown in Figure 51.

5.3 MULTIDIMENSIONAL HEAT TRANSFER TESTS

A calorimeter-type test model was constructed for verification of the multidimensional heat-transfer analysis. Testing was limited to a single insulation system (aluminized polyimide film shields with Dexiglas spacers). The effects of a strut and penetration at the temperature of the system cold boundary and edges exposed to a LN_2 cooled sink were measured for comparison with the results of the analytical studies.

A three-chamber calorimetric type of apparatus, described in Appendix E, was constructed for this portion of the program. Test conditions were to regulated hot and cold boundary temperatures rather than to subject the exterior insulation surface to an absorbed heat flux. Thus, these data yield a ratio of conductance to the one-dimensional conductance for fixed boundary temperatures. Although the absorbed flux method would result in direct ratios of heat transfered into a specific geometry, it is a more complex procedure because of the necessity of very accurate knowledge of source and surface spectral characteristics.

5.3.1 Insulation System

The multilayer insulation system consisted of 29 layers of aluminized polyimide film (1.27×10^{-2} mm thick) procured from NRC Corporation and 28 layers of Dexiglas paper (7.63×10^{-2} mm thick). The blanket was made up for a 96 cm length in four layer sections. The section placed in contact with the cold boundary contained 11 reflective layers. Each of the other sections was fabricated using 6 reflective layers. These sections were arranged to provide a staggered-type joint. The overlap was

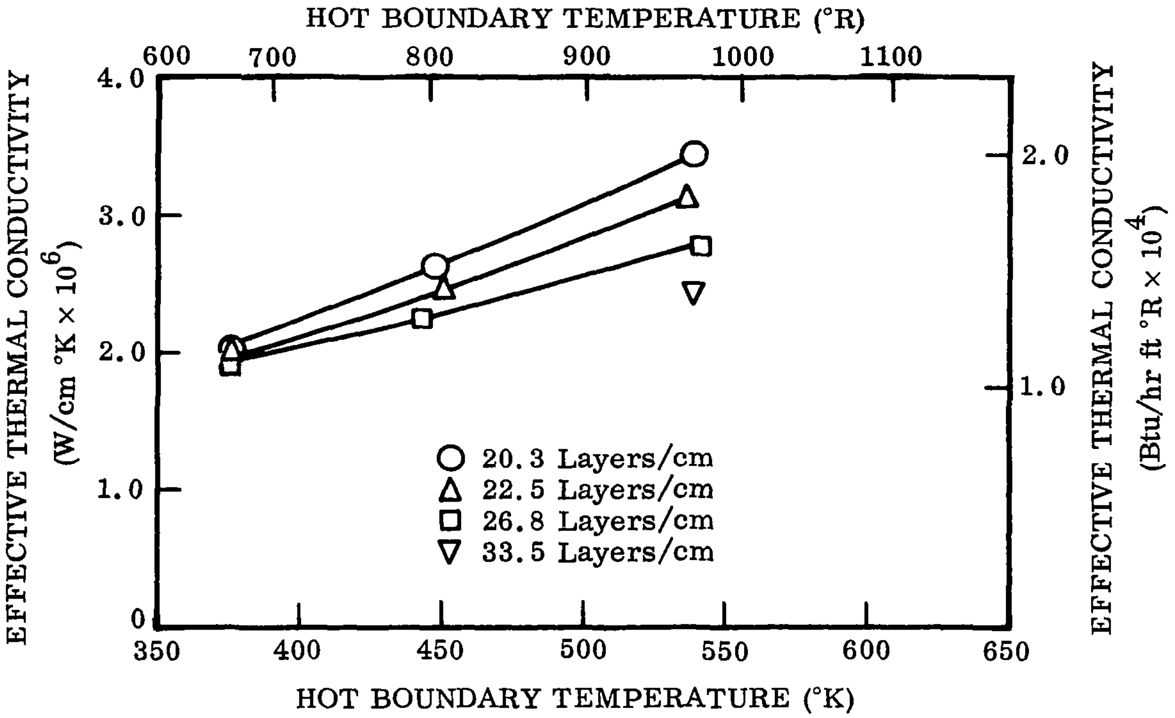

Figure 49 Effective Thermal Conductivity of Aluminized Polyimide Film Insulation, No Spacer Material (Dimpled)

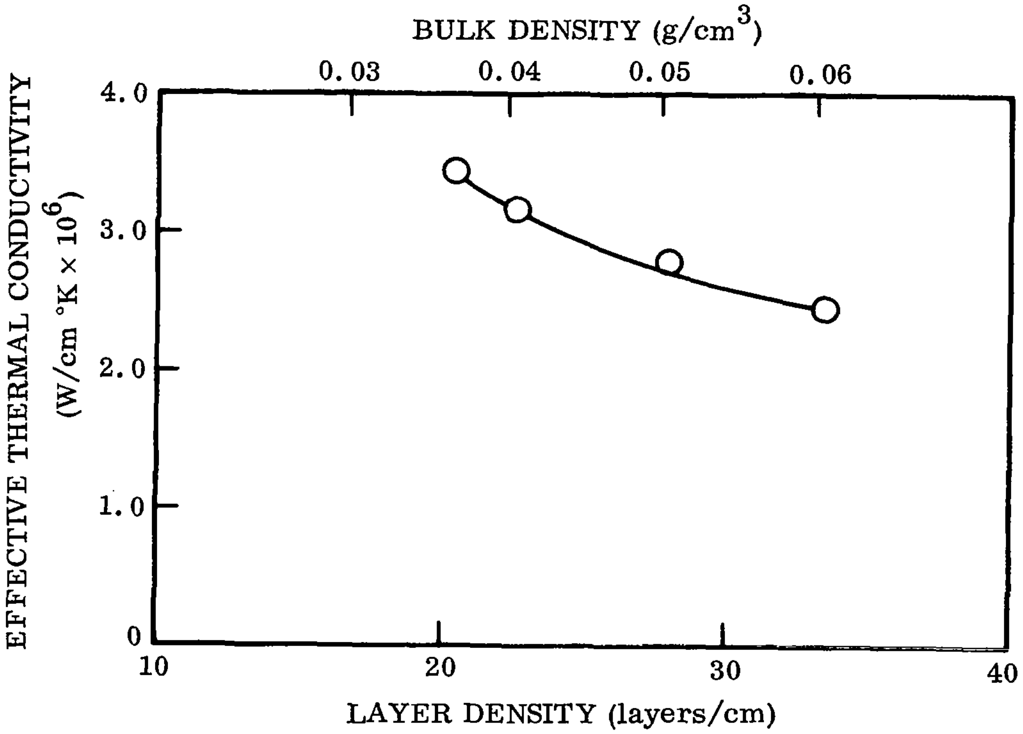

Figure 50 Effective Thermal Conductivity of Dimpled Aluminized Polyimide Film as a Function of Layer and Bulk Density

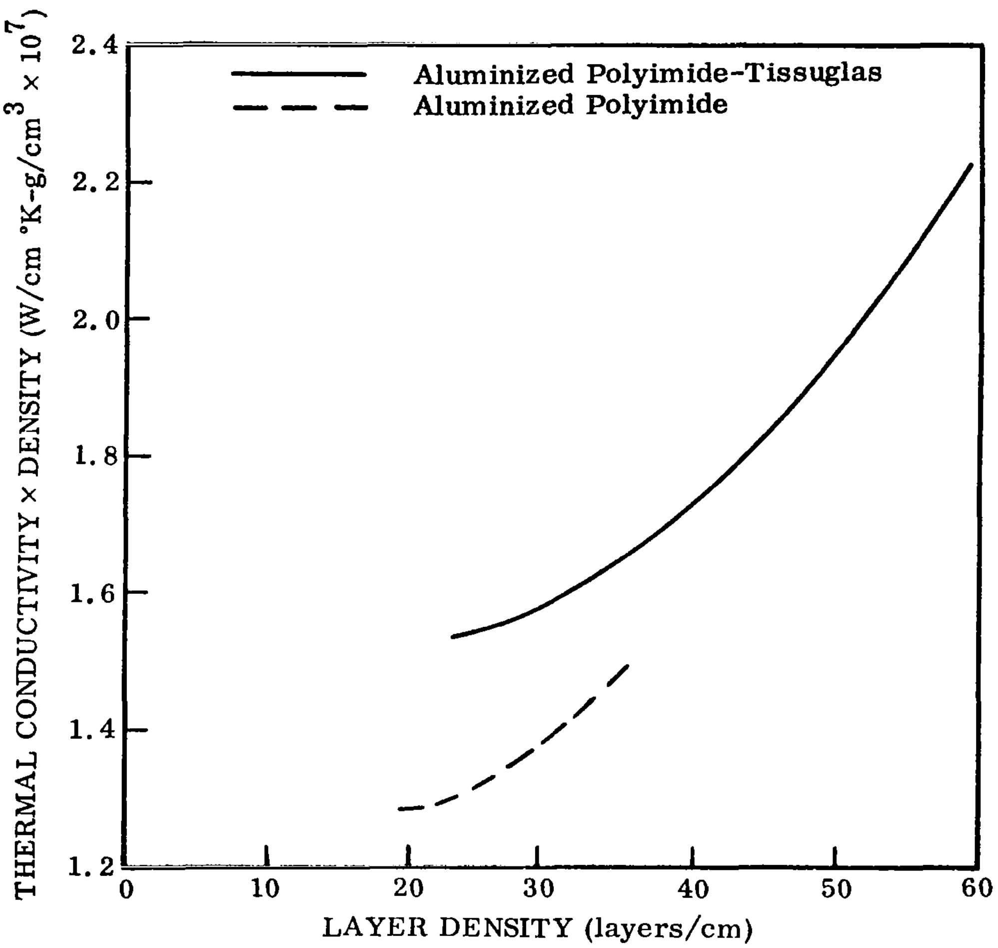

Figure 51 Thermal Conductivity Times Density Product for Two Multilayer Systems for a 500°K Hot Boundary Temperature

approximately 2 cm to adjacent layers (Figure 52). The reflective shields were terminated 10 cm from the end of the blanket. Alumel steel wires, 3-mil in diameter, were used to support the blanket as illustrated by Figure 52. These were located on 15-cm centers. Attachment of the blanket to the model was accomplished using Velcro fasteners on 15-cm centers. These were bonded to the surfaces using a rubber-base adhesive. During installation of the insulation on the model, two of the 3-mil wires failed. This occurred near the overlap joint due to handling while the blanket was being placed on the model in the vertical position. A total of 12 support wires remained intact during test.

Thermocouples were attached to the 11th, 17th, and 23rd reflective shield layers. For the 11th and 23rd layers they were located as shown in Figure 53. Only a center point thermocouple was used for the 17th layer. Junctions were attached to the metal surface with a conductive, silver, filled epoxy cement.

5.3.2 Experimental Results

The heat transfer rates measured for the one-dimensional condition were 0.82, 1.59, and 3.48 W for outer boundary temperatures of 293°, 366°, and 467°K, respectively. The effective thermal conductivity of the test insulation, 0.89 cm thickness, is shown by Figure 54 as a function of hot boundary temperature. A comparison is made with the range of values of thermal conductivity of an aluminized Mylar-Dexiglas system of comparable layer density and at a 300°K hot boundary temperature. These data, obtained by the NBS-type cryostat for a continuous wrap system and from a penetration calorimeter for a layered configuration (ref. 16), are somewhat lower than those measured for the test model insulation. The local compression of this insulation at support wires, attachment points, and the insulation joint is believed to cause a significant portion of this discrepancy. Thermal conductivities for a section of layers were estimated on the basis of the temperatures measured at intermediate layers. To compensate for the varying boundary temperatures across such sections, the data are plotted as a function of the radiative potential term. As shown by Figure 55, the data agree reasonably well with those based upon overall boundary conditions. The scatter is attributed to the local variations in layer density. Inspection of the insulation upon completion of testing showed a layer density variation on the order of 20%.

The measured temperature profiles through the insulation at the center point are shown by Figure 56. The dashed lines represent the data obtained from the analytical program using the conductivity versus temperature data extrapolated to lower temperatures from the curve of Figure 54. Examination of the layer temperature data showed a compression at the insulation joint. Temperatures measured in this area were 20° to 40°K lower than the remainder of the layers for the section adjacent to the cold boundary (11th layer). At the 23rd layer position (toward exterior surface), this difference did not exceed 5°K for all hot boundary temperatures. The variations observed between the center thermocouple and those located 15 cm away in an axial direction were within 1.5°K for all tests. Similar results were obtained for those spaced 25 cm from the center toward the insulation joint.

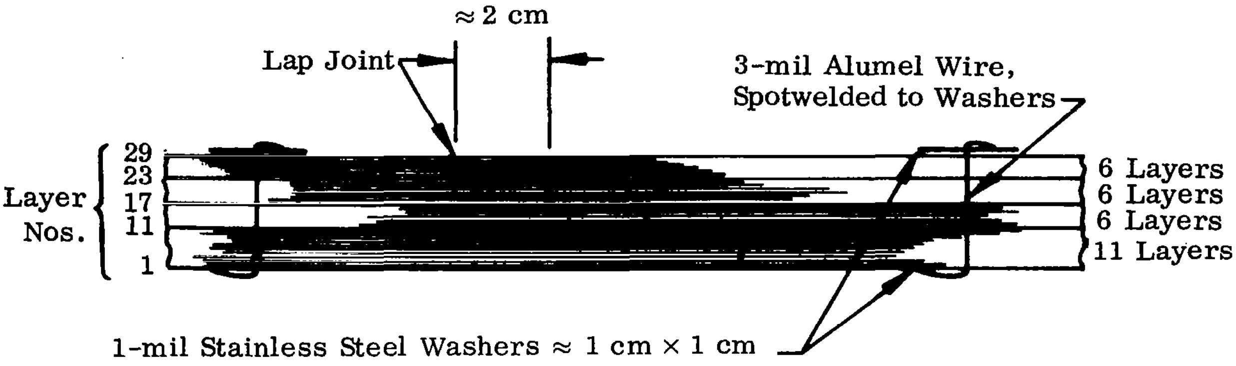

Figure 52 Details of Insulation Lap Type Joint and Support Wires for Blanket

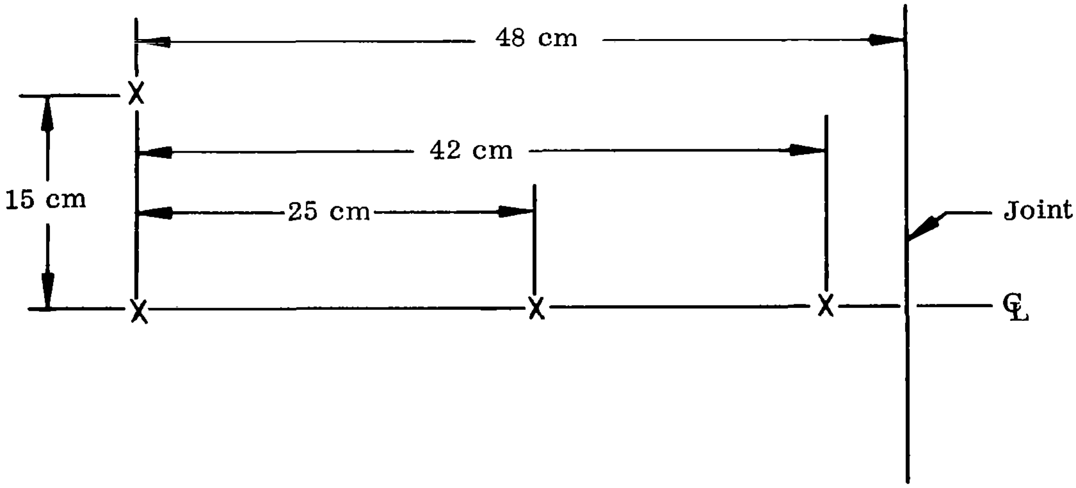

Figure 53 Locations of Thermocouples on 11th and 23rd Insulation Layers

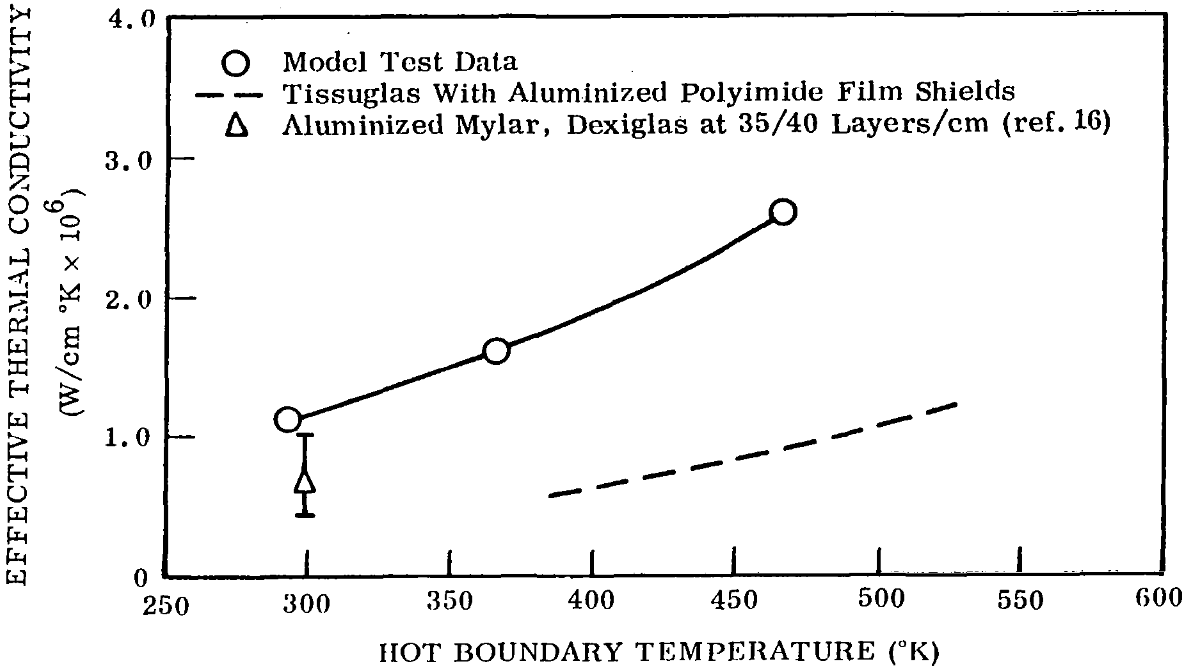

Figure 54 Effective Thermal Conductivity of Model Test Insulation as Measured During Model Tests, With a 77°K Cold Boundary

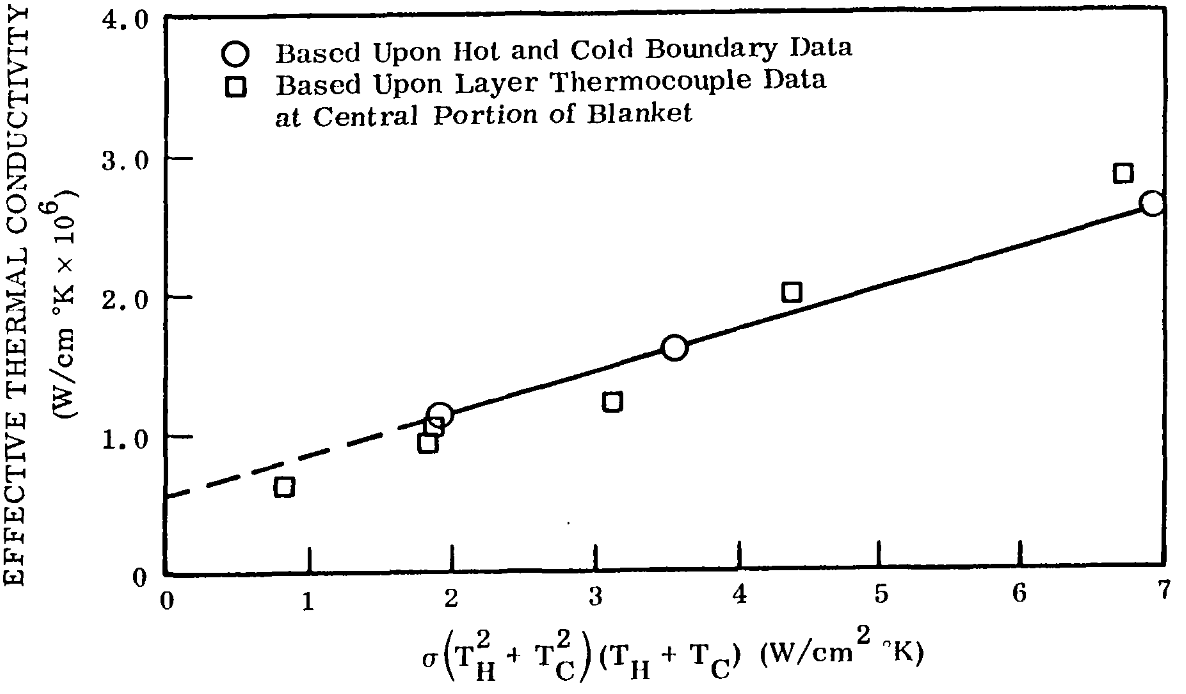

Figure 55 Effective Thermal Conductivity of Test Insulation as a Function of Radiative Potential

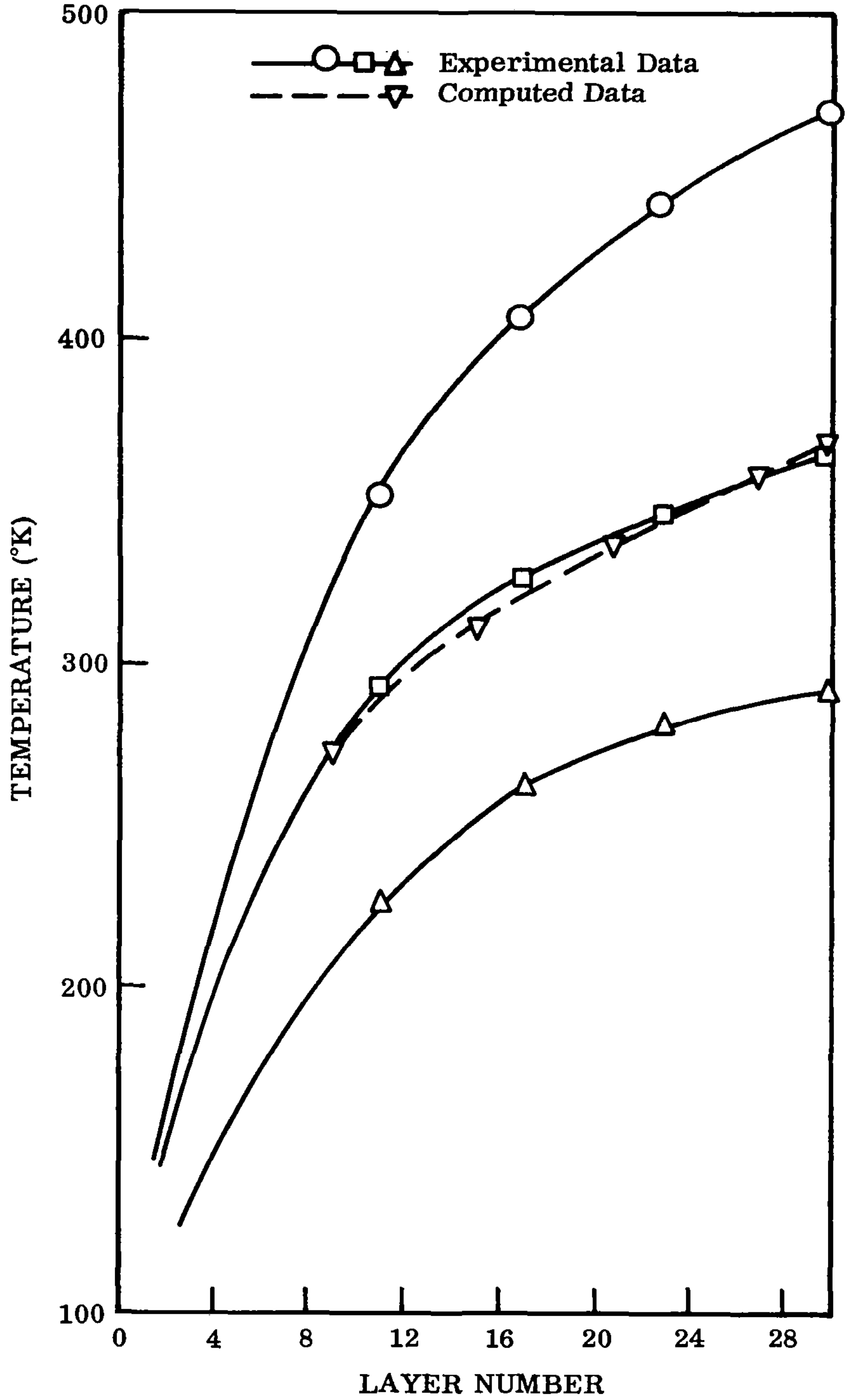

Figure 56 Insulation Temperature Gradients at Centerline of Blanket

The constant temperature penetration (77° K) tests were conducted at hot boundary temperatures of 295° and 368° K. Penetration temperatures for these tests were 82° and 85° K, respectively. As the penetration temperature was slightly higher than cold boundary temperature, some thermal resistance was present in this path which would result in a small decrease in heat transfer from the insulation. For the 295° K condition, the measured heat input was 1.07 W or 1.30 times the one-dimensional value. At a 368° K temperature, a heat input of 2.19 W was measured. This is 1.37 times the one-dimensional heat input.

For the condition of a constant temperature penetration and strut, the measured values of heat input to the calorimeter were as follows: 1.65 W at 296° K, 2.01 times the one-dimensional condition; and 3.37 W at 3.67° K, 2.13 times the one-dimensional value. As the area of insulation exposed at the butt joint to the strut is approximately four times that at the penetration, a greater degradation of insulation performance might be expected than was observed. The presence of the additional heat transfer path alters the gradient through the insulation and reduces the potential between the insulation and the strut. Comparison of the one-dimensional layer temperature data with the data for this case shows a reduction of 20° to 45° K in temperatures measured on intermediate layers. For a large system of low parallel conductivity, the effects should be additive. However, for small systems, as with higher parallel conductivities, the zone of penetration influence overlaps that of the strut.

The test conditions with the edges of the insulation radiating to a 77° K sink did not result in any useful data. Cutting of the insulation at the ends of the measuring section produced two circumferential gaps approximately 0.3 cm in height. Interior portions of the calorimeter were exposed to thermal energy from the surroundings which resulted in a large heat leak into the calorimeter. Approximate calculations showed the magnitude of this leak could account for from 40 to 70% of the measured heat input. Therefore, the data from this phase are not reported.

5.4 DISCUSSION OF EXPERIMENTAL RESULTS

The best choice of materials for construction of an efficient multilayer insulation system is the metallized polyimide film for reflective shields and a submicron-size glass fiber paper for the spacer. Aluminized polyimide film withstands the temperature and vacuum environmental conditions of the high-temperature insulation system without showing any significant changes in either the thermal or mechanical properties which are important to system performance. Although thermally efficient systems are achieved using the presently available commercially coated materials, further improvements in coating and processing techniques are desirable to produce a more efficient system from density-conductivity product considerations. A reduction in thermal conductivity of approximately 30% should be attained if metallizing techniques are improved so that the total hemispherical emittance of the coated material is reduced to values more nearly approaching that of the pure metal.

In regard to the spacer materials, the Dexiglas paper maintains better strength after exposure to elevated temperatures than does the Tissuglas. The latter, however, shows better strength at room temperatures which makes it a more attractive material from the standpoint of fabrication. An improvement in spacer thermal properties can be achieved by producing a material which acts as a better scattering media for the temperature range of the multilayer insulation. The submicron-size fibers exhibit maximum scattering cross sections at short wavelengths which correspond to temperatures higher than 700°K. The scattering cross section is strongly peaked at a characteristic wavelength of the incident radiation which is related to π times the fiber diameter. Consequently, for maximum scattering an ideal spacer would be composed of fibers in the 5- to 15-μ-diameter range. Fiber-to-fiber spacing must also be considered as coherent scattering effects are important.

An insulation composed only of radiation shields, spacers formed into shields themselves, is the most efficient from a conductivity times density ($k\rho$) consideration. However, this system has at least twice the parallel thermal conductivity of the shield-spacer construction. This is due to the greater radiant energy transfer along the voids between shields shich form a highly reflective cavity. A high value of parallel conductivity could result in severely degraded insulation performance in the vicinity of exposed edges or large penetrations.

Because of the complex geometry of the fiber materials, no theoretical model was found which would permit calculation of the solid phase conductivity of the insulations tested. However, an empirical expression based upon bulk density and temperature gives a good approximation for the solid conduction term. The constant for the solid phase conductivity term was determined from a plot of effective thermal conductivity versus the radiative term, $\sigma(T_H^2 + T_C^2)$. For both spacer and multilayer insulations solid phase conductivity was directly proportional to the spacer bulk density. However, the solid conductivity for the multilayer systems, at the same bulk density, is less than that for the spacer material alone, which suggests that the thermal resistance at each shield-to-spacer interface is significant.

Comparisons of experimental data with values of effective thermal conductivities calculated for several multilayer systems are shown by Figure 57. The calculations were carried out using the expression

$$k_e = C\rho T + \frac{\bar{n}^2 \sigma \left(T_H^2 + T_C^2\right)(T_H + T_C)\, t}{(a + 2s)\frac{t'}{2} + (N - 1)\left(\frac{2}{\epsilon} - 1\right)}$$

Reasonably good agreement is shown for specimen 6 which has a calculated ratio of radiant-to-conductive transport of less than 5 over the temperature range of 350° to 650°K. Also, the term accounting for absorption and scattering is much smaller than the term for the reflective shields. Specimen 3 has a ratio of radiant-to-conductivity transport of less than 5, but the size of the absorption and scattering

Specimen	Description
1	10 Layers Aluminized Polyimide Film, 11 Layers Dexiglas (2.3×10^{-2} cm), t = 1.27 cm
3	Same as No. 1 Except t = 0.635 cm
4	10 Layers Stainless Steel, 11 Layers Dexiglas, t = cm
6	30 Layers Aluminized Polyimide Film, 31 Layers Dexiglas, t = 1.27 cm

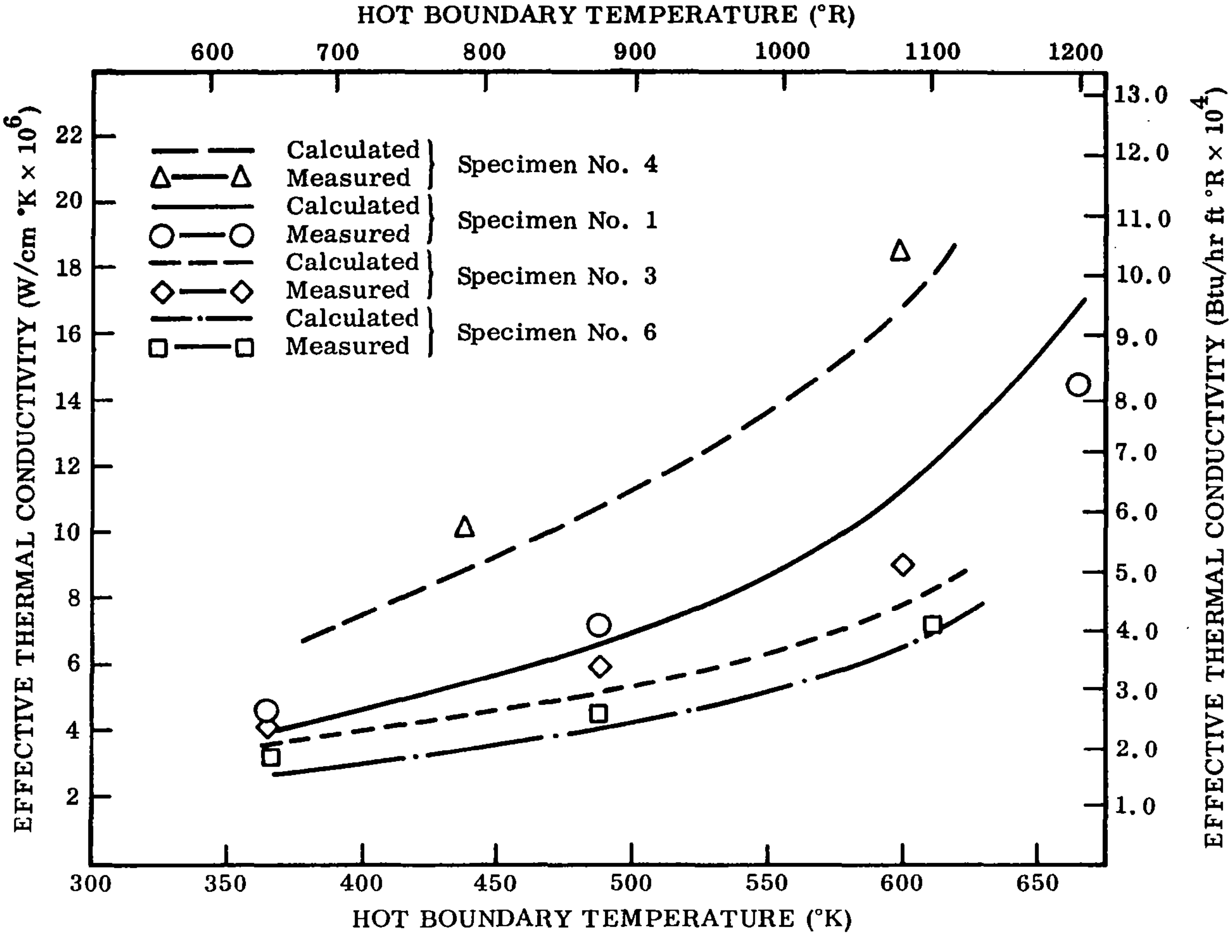

Figure 57 Comparison of the Calculated and Measured Values of Thermal Conductivity for Four Multilayer Insulation Systems

term is approaching that of the shield emittance term. Specimens 1 and 4 both have transport ratios greater than 10. For specimen 4, which shows the poorest agreement, the scattering term is the same as the multiple shield term. Based upon these comparisons, a good approximation of effective thermal conductivity may be made by neglecting interactions between conduction and radiation if the ratio of radiative-to-conductive transport is less than 5 and the ratio of scattering term to emittance term is less than 0.25. For the cases in which the absorption and scattering term is large, the interaction between conduction and radiation must be considered.

Figure 58 shows the agreement between calculated and experimental data for the Tissuglas aluminized polyimide film composite and the system using only reflective shields. The approximate model solution agrees with the experimental data within 5%.

The results of the analytical studies of the constant temperature penetration for the experimental temperature conditions are shown in Table 7. The measured value of heat input is 2.2 W. This is in good agreement with the results for an insulation having a parallel thermal conductivity of 4.3×10^{-3} W/cm°K. Data on the parallel conductivity of an aluminized Mylar-Dexiglas insulation having approximately the same layer density and thickness of aluminum (ref. 21) shows the conductivity varies from 3×10^{-4} to 7×10^{-4} W/cm°K over the test temperature range. An average value of $K_{\parallel}$ based upon the measured layer temperature gradient is 5.5×10^{-4} W/cm°K. The layer temperature data from the analytical study shows the penetration effect occurs to radial distances of 9 cm for a $K_{\parallel}$ of 4.3×10^{-4} and 14 cm for a $K_{\parallel}$ of 1.7×10^{-3} W/cm°K. The conductance between the insulation and penetration did not have a significant effect upon the results as evidenced by comparing the values for $\epsilon = 0.3$ and $\epsilon = 10.0$.

Table 7. – ANALYTICALLY DETERMINED HEAT INPUTS FOR CONSTANT TEMPERATURE PENETRATION ($T_H = 366$°K)

Parallel conductivity (W/cm °K)	Q_{Total} (W)	$Q_{Penetration}$ (W)
1.7×10^{-4}[a]	2.0	0.4
4.3×10^{-4}[a]	2.3	0.6
1.7×10^{-3}[a]	2.8	1.4
1.7×10^{-3}[b]	3.0	1.6

[a] ϵ at boundary = 0.3
[b] ϵ at boundary = 10.0

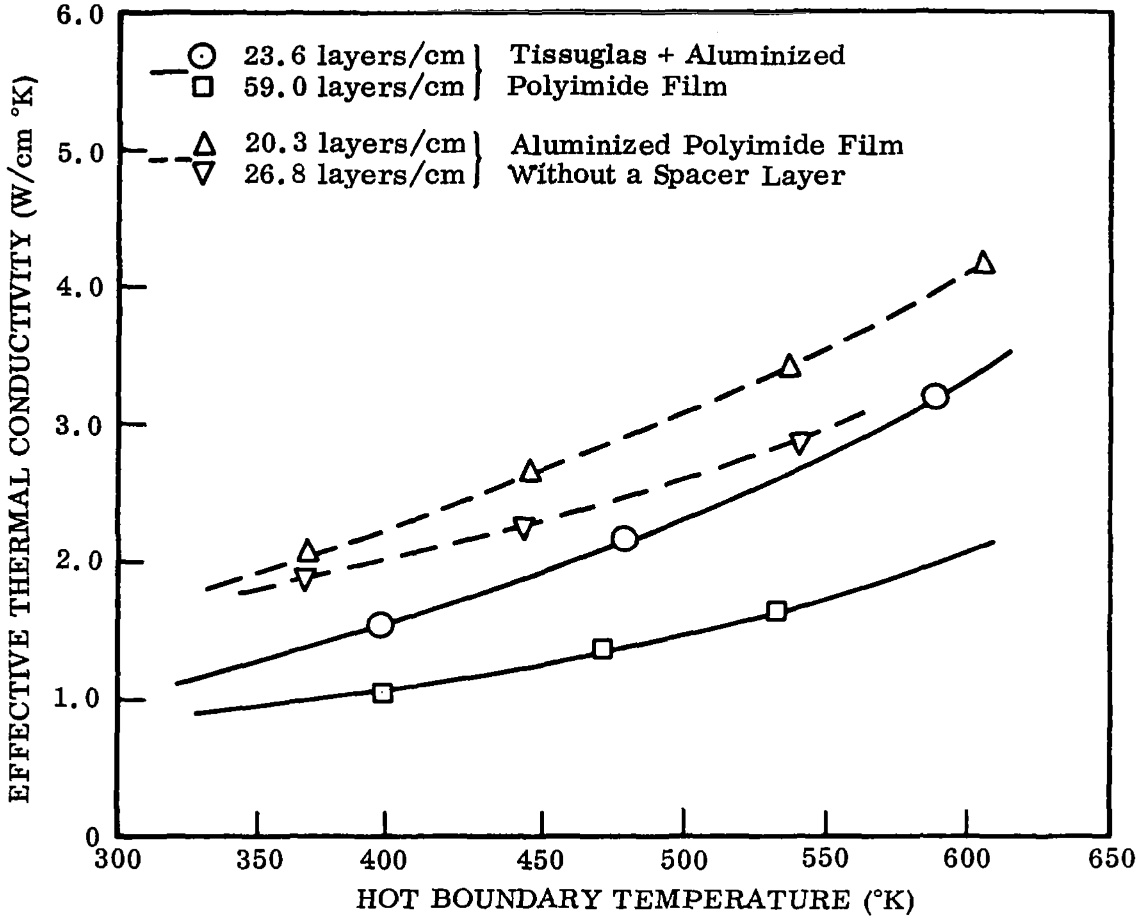

Figure 58 Comparison of Calculated and Experimental Values of Thermal Conductivity for the Aluminized Polyimide Film Multilayer Insulation (Lines Represent Calculated Values)

A qualitative comparison between the results of the radial model studies and those using the cylindrical model may be made using the data from Figure 20. The normal conductivity ($K_\perp$) used for computing these data is higher than that of the system for the cylindrical model. However, by taking a ratio of conductivities ($K_\parallel/K_\perp$) the two models may be compared for trends of the effect of the penetration. A heat input ratio (Q_p/Q_{1D}) is calculated using Eq. (15) and the values of R^{*2} from Figure 20. This comparison is shown by Figure 27, and the correlation is within 10 percent.

The analytical predictions of heat transfer for the model with both the strut and penetration are shown in Table 8. Again, the experimental heat input of 3.4 W agrees with the analysis for a material having a $K_\parallel$ of 4.3×10^{-4} W/cm°K. Heat input through the penetration is the same as for the case on a penetration alone. For the lowest value of $K_\parallel$, the strut has four times the heat input as the penetration which corresponds to the area ratios. This decreases with increasing values of $K_\parallel$ as the areas of two-dimensional heat transfer begin to overlap. The layer temperature profiles for a $K_\parallel$ of 1.7×10^{-4} W/cm°K show an effect of approximately 8 cm radially for the penetration and 8 cm for the strut which are spaced 23 cm apart. For a $K_\parallel$ of 1.7×10^{-3} W/cm°K, the temperature profiles verify the overlap of the zones.

Table 8. – ANALYTICALLY DETERMINED HEAT INPUTS FOR CONSTANT TEMPERATURE PENETRATION AND STRUT (366°K)

Parallel conductivity (W/cm °K)	Q_{Total} (W)	$Q_{Penetration}$ (W)	Q_{Strut} (W)
1.7×10^{-4}[a]	3.0	0.4	1.5
4.3×10^{-4}[a]	3.6	0.7	1.9
1.7×10^{-3}[a]	5.6	1.4	3.2
1.7×10^{-3}[b]	5.8	1.5	3.3

[a] ϵ = 0.3
[b] ϵ = 10.0

The analytical data from the radial and the slab models may be combined to calculate a ratio of Q/Q_{1D} for comparison with the cylindrical model and test results. Converting the slab model butt joint data to a conductivity ratio corresponding to that of the cylindrical model condition ($K_\parallel/K_\perp = 270$) for an ϵ of 0.05 an effective ℓ^* is 40 cm. This represents a degradation of 83% in heat input. The constant temperature penetration analysis yields a degradation of 42% for these insulation properties. Combining these, a total heat input is calculated to be 3.58 W which compares favorably with the 3.6 W from the cylindrical model data and 3.4 W for the test results.

Section 6

CONCLUSIONS

A study has been made of the performance of multilayer insulation systems for use in the 300° to 700°K temperature range. A number of reflective shield and spacer materials have been evaluated, and thermal conductivities measured for several insulation systems. Effects of the anisotropic thermal conductivity properties of the insulations have been analyzed and compared with limited experimental data. General recommendations for treatment of the multidimensional heat transfer problems are developed. The principal results obtained are as follows:

- Metallized polyimide film and glass fiber spacer materials are compatible with the vacuum and temperature environment to 700°K. The optical properties of commercially available metallized organic films need improvement to achieve an optimum insulation system.
- Thermal conductivities of insulations composed of aluminized polyimide film-glass fiber spacers and aluminized polyimide films with integral spacers are presently achievable in the range of 1×10^{-6} to 3×10^{-6} W/cm°K for 300° to 700°K temperature conditions. Typical insulation densities are 0.050 to 0.125 g/cm^3. Intermediary insulation of compressed submicron fiber size glass paper has a thermal conductivity on the order of 2×10^{-5} W/cm°K over this temperature range.
- The simplified heat transfer model permits engineering-type calculations of multilayer insulation thermal conductivities based upon spacer and shield thermophysical properties and physical characteristics of the system.
- Analytical models developed to study the multidimensional heat transfer in multilayer insulations permit predictions of the effects of discontinuities upon overall thermal performance.

Comparison of the results of the cylindrical model to the slab and radial models shows the data from the latter models may be combined for calculating thermal performance when penetrations are separated by distance such that two-dimensional zones do not materially overlap. Good agreement was obtained between models for penetration and strut or butt joints. However, when edges are considered in conjunction with penetration, the cylindrical model is needed to account for the three-dimensional effect such as observed for the strut normal to an edge or where the degraded zones of discontinuities overlap. The experimental tests established the validity of the analytical models.

Section 7

REFERENCES

1. Streed, E. R., and Arvesen, J. C.: A Review of the Status of Spacecraft Thermal Control Materials, Society of Aerospace Material and Process Engineers Annual Meeting, St. Louis, Mo., 1967.

2. Riede, P. M., and Wang, D. I. J.: Characteristic and Applications of Some Superinsulations, Advances in Cryogenic Engineering, Vol. 5, Plenum Press, 1959, pg. 209.

3. Caren, R. P., and Cunnington, G. R.: Properties and Applications of Multilayer Insulation Systems, AICHE Annual Meeting, Houston, Texas, 1967.

4. Verschoor, J. D., and Greebler, P.: Heat Transfer by Gas Conduction and Radiation in Fibrous Insulations, Trans. Am. Soc. Mech. Eng., 74, 1952.

5. Wang, D. I.: Multiple Layer Insulations, presented at 1961 Conference on Aerodynamically Heated Structures, AFOSR, 1961.

6. Wechsler, A. E., and Glaser, P. E.: Investigation of the Thermal Properties of High Temperature Insulation Materials, ASD TDR-63-574 (July 1963).

7. Strong II, M., Bundy, F. P., and Bovenkirk, M. P.: J. Appl. Phys., 31, No. 1, Jan. 1960.

9. Hamaker, H. C.: Radiation and Heat Conduction in Light Scattering Materials, Phillips Res. Reports, Vol. 2 (1947).

10. Larkin, B. K. and Churchill, S. W.: Heat Transfer by Radiation Through Porous Materials, J. AICHE, 476 (1959)

11. Klein, J. D.: Heat Transfer by Radiation in Powders, Ph.D. Thesis, Massachusetts Institute of Technology (1960).

12. Glaser, P. E., Wechsler, A. E., Simon, I. and Berkowitz, J.: Investigation of Materials for Vacuum Insulation up to 4000° F, ASD TDR-62-88 (1962).

13. Viskanta, R.: Heat Transfer by Conduction and Radiation in Absorbing and Scattering Materials, J. Heat Transfer (ASME), pg. 143 (1965).

14. Folweiler, R. C.: Thermal Radiation Characteristics of Transparent, Semi-Transparent, and Translucent Materials Under Non-Isothermal Conditions, ASD TDR-64-719 (1964).

15. "Radial Insulation Penetration Model," Contract NAS 8-11347, LMSC-A742593, Vol. IV, Aug. 1965.

16. Study on High-Performance Insulation Thermal Design Criteria, LMSC-A852904, Prepared under Contract NAS 8-20353, Final Report for NASA George C. Marshall Space Flight Center.

17. Shaw, C. C.: Apparatus for the Measurement of Spectral and Total Emittance of Opaque Solids. Surface Effects on Spacecraft Materials (F. J. Clauss, ed.) John Wiley & Sons, Inc., 1964.

18. Dunkle, R. V. et al., Heated Cavity Reflectometer for Angular Reflectance Measurements, ASME, Progress in International Research on Thermodynamic and Transport Properties, Academic Press, New York, 1962, pg. 541.

19. Davisson, C. and Weeks, J. R.: The Relation Between the Total Thermal Emissive Power of a Metal and Its Electrical Resistivity. J. Opt. Soc. Am., 8, pg. 581 (1924).

20. Greenberg, S. A. and Vance, D. A., Low Solar Absorptance and Emittance Surfaces Utilizing Vacuum Deposited Techniques, Report No. CR-73039, Final Report for NASA, Ames Research Center, Oct. 1966.

21. Coston, R. M. and Vliet, G. C., Thermal Energy Transport Characteristics Along the Laminations of Multilayer Insulations, AIAA Thermophysics Conference. New Orleans, 1967.

22. Plank, W.: Physik Z, 15, (1914)

23. Bitler, W. R., 1965, Optical Properties of Metals and Alloys, AFOSR-65-1843, 1965.

Appendix A

METAL FILM THICKNESS CHARACTERIZATION

Several measurements techniques were employed to determine the thicknesses of the metal films on the polyimide film for correlation with total emittance data. These were electrical resistance, light-transmission, weight by difference, and electron microscope studies of cross sections of the film. Resistance, weight difference, and the electron microscope were utilized for the aluminum coatings. Light transmission and resistance were used to characterize the gold and silver coatings. Also, for the aluminum coatings prepared by D. L. Clausing Company, optical flats were placed adjacent to the film during the evaporation process. Film coating thicknesses on the flats were determined by the interferometer method.

Film thickness was calculated from resistance measurements using the relationship between resistance per unit area, resistivity of the bulk metal, and thickness of the metal film (ref. 22). The expressions used for aluminum, gold, and silver are given by Eqs. (A.1) through (A.3).

$$R_{Al} = \frac{2.65 \times 10^{-8}}{t} + \frac{3.14 \times 10^{-16}}{t^2} \tag{A.1}$$

$$R_{Au} = \frac{2.35 \times 10^{-8}}{t} + \frac{3.38 \times 10^{-16}}{t^2} \tag{A.2}$$

$$R_{Ag} = \frac{1.59 \times 10^{-8}}{t} + \frac{3.38 \times 10^{-16}}{t^2} \tag{A.3}$$

The resistances per unit area (in ohms per square) are plotted as a function of thickness for these three metals in Figures 59, 60, and 61.

Film resistance is measured using a Leeds and Northrup Model 4285 Kelvin Bridge and a copper probe unit. The latter consists of two copper current electrodes 10 cm long by 0.6 cm wide having a 0.3-cm radius on the edge which is placed in contact with the film. The potential contacts are 3.8 cm long by 0.6 cm wide copper bars having a square edge for contact with the film at a spacing of 3.8 cm. The test specimens are strips 3.8 cm wide by 15 cm long. For each strip, three determinations of resistance are made along a 10-cm spacing between current electrodes. To evaluate the possible effect of nonuniform contact resistance on the film data, the

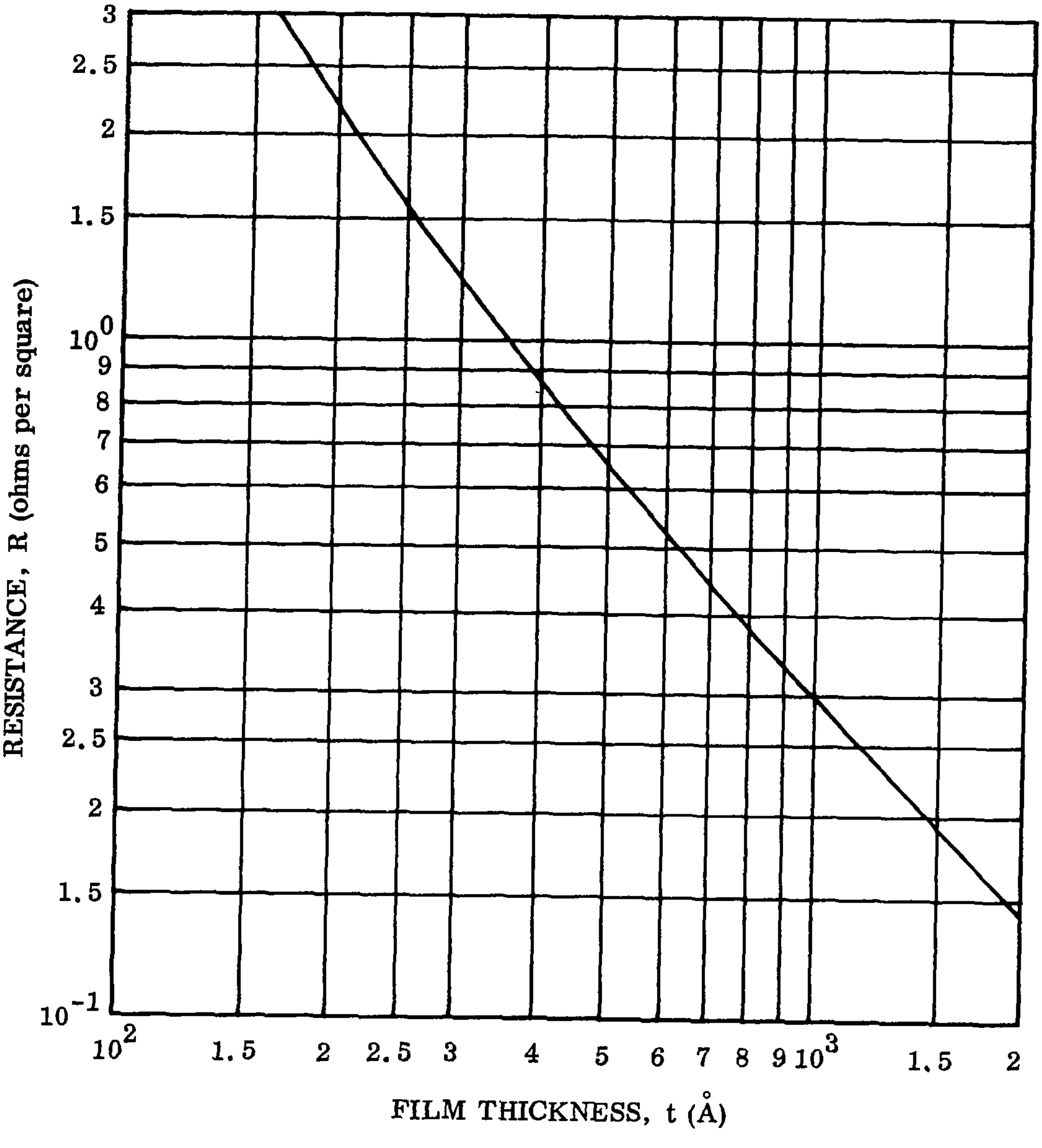

Figure 59 Thickness of Aluminum Film as a Function of Film Electrical Resistance From Eq. (A.1)

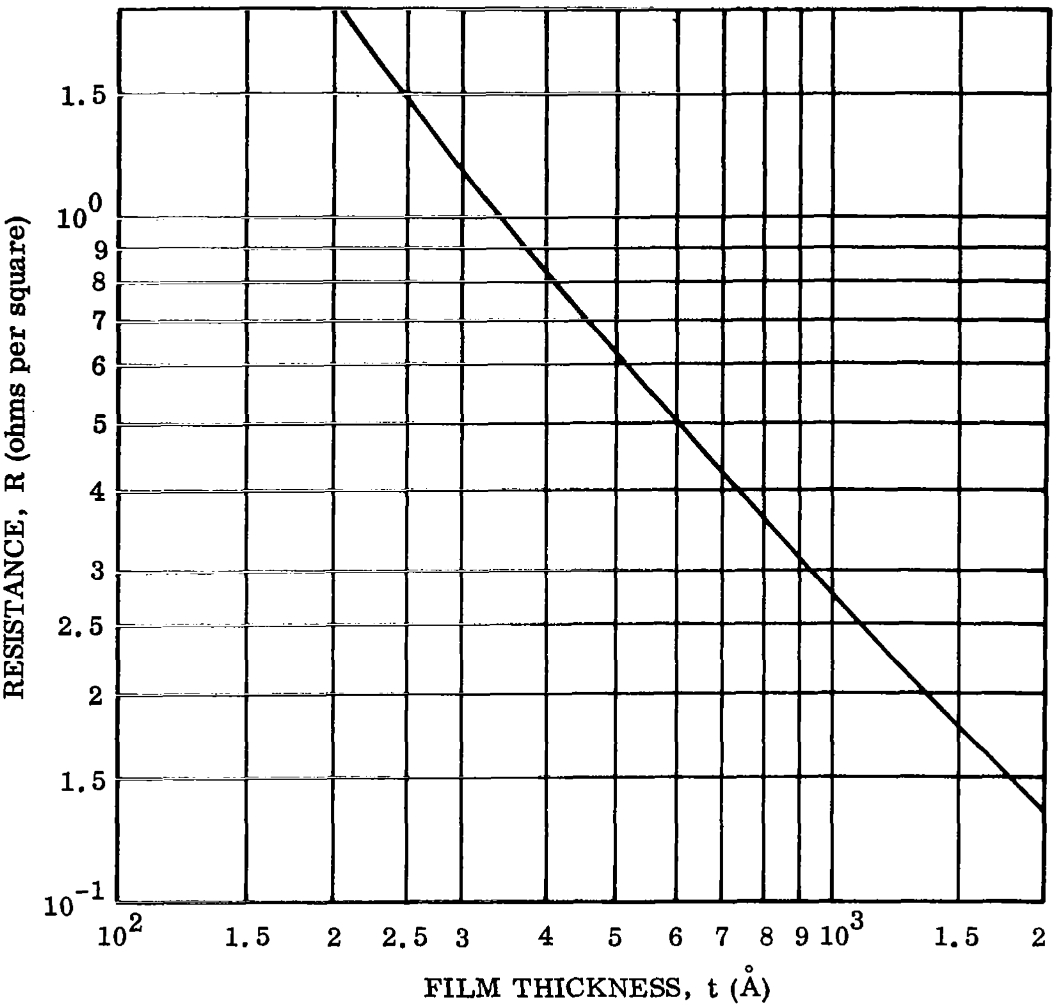

Figure 60 Thickness of Gold Film as a Function of Film Resistance as Calculated From Eq. (A.2)

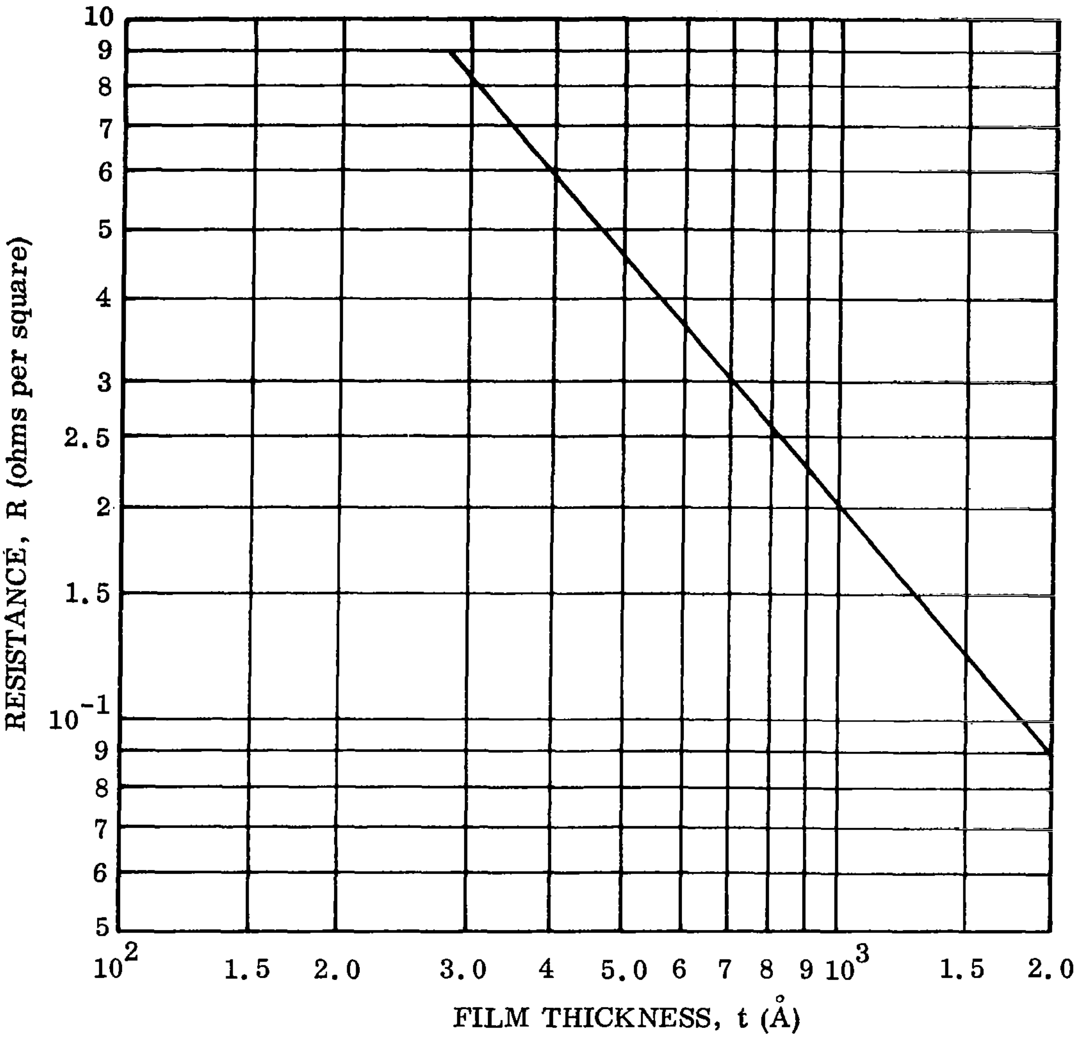

Figure 61 Thickness of Silver Film as a Function of Electrical Resistance From Eq. (A.3)

electrodes and two of the aluminum film specimens were coated with a mercury-indium amalgam. Essentially no difference in resistance was observed using this method over the standard procedure of a dry contact between electrode and film. All specimens are cleaned with acetone, detergent solution, distilled water, and ethyl alcohol, then air dried prior to measurement.

For the electron microscope studies, the metal film is removed from the polyimide substrate by coating it with an epoxy resin and then stripping the metal and epoxy from the polyimide. The epoxy-metal layer is cast in epoxy resin and transverse sections cut through the film with a microtome. After replication of the section, photographs are made at a magnification of 4000×.

The weight-by-difference method consists of weighing a 15 cm square section of coated film before and after removal of the aluminum coating with HCl. A microanalytical balance is employed for the weighing. A blank determination was made on one uncoated polyimide film specimen to determine if any weight change is due to the acid treatment. No measurable change was observed.

The light transmission method, as described by W. R. Bitler in ref. 23 , was limited to use with the gold and silver coatings as the optical constant calculations had been performed for these metals. A Beckman Model DU spectrophotometer is used for the transmission measurements.

Appendix B

TOTAL HEMISPHERICAL EMITTANCE APPARATUS

A calorimetric method was used to determine the emittance of samples in the form of small, hollow cylinders. By this method the sample is suspended inside a large evacuated test chamber with nonreflective black walls that are liquid nitrogen cooled (Figure 62). The sample is heated to a desired test temperature by means of a small heating filament which is totally enclosed within the hollow sample. At steady state, the total hemispherical emittance of the sample is calculated from the energy balance equation, knowing the sample temperature, its surface area, the electrical power expended by the sample heater, and the temperature of the surrounding test-chamber walls. For low-emittance samples at low test temperatures (i.e., $T_S < 300°K$), the energy loss by thermal conduction through the heater leads and sample thermocouple wires is also important. Since the test chamber is evacuated, heat transfer by gaseous conduction and convection is negligible.

Total hemispherical emittance values are calculated from the following equation, derived from the steady-state energy balance:

$$\epsilon_H = \frac{VI - P_L}{A\sigma\left(T_s^4 - T^4\right)} \tag{B.1}$$

The heater voltage drop is measured between two platinum emf leads which are attached to the heater power leads just above the sample cap. Heater current is measured with a 10-A, 100-mV current shunt in series with the heater circuit and the dc power supply. The surface area of the sample (A) is calculated from micrometer measurements of the sample dimensions. For each of the samples in these tests, the room temperature surface area was corrected to account for thermal expansion of the sample. Published data for the thermal expansion of aluminum was used, and the maximum correction amounted to a 1.9% increase in surface area at 650°K. Sample temperature is measured by two platinum/platinum-13% rhodium thermocouples attached to the sample. The temperature of the test chamber walls is assumed to be the atmospheric boiling point temperature of the liquid nitrogen used to cool them, 77°K. The thermal conduction loss term is calculated from published data for the thermal conductivity of the heater lead material, molybdenum, the cross section area of the leads, and the temperature gradient along the leads. The latter quantity is determined from temperature measurements at two points, approximately 1 cm apart, just above the sample cap using platinum/platinum

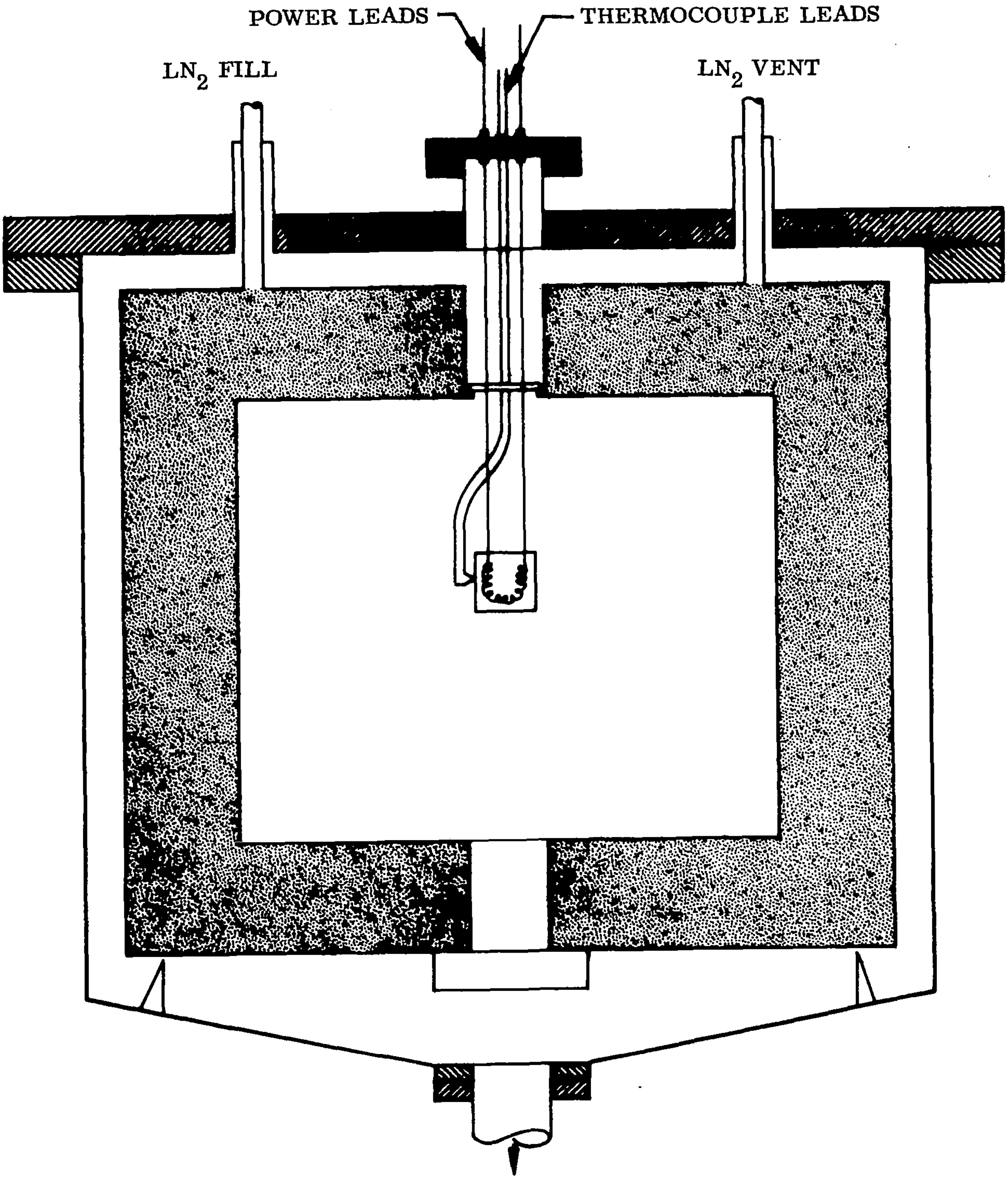

Figure 62 Total Hemispherical Emittance Test Chamber

13% rhodium thermocouples spot welded to the heater leads. The total power loss through both leads is given by:

$$P_L = \frac{2KA\Delta T}{X} \tag{B.2}$$

where K is the thermal conductivity, A is the cross section area, and ΔT is the temperature drop between the lower and upper heater lead thermcouples separated by the distance X . Additional terms can be included in Eq. (B.2) to account for the internal joule heating and the radiation from the heater leads. For these tests, however, computations of these latter terms showed them to be negligibly small relative to the conduction term. Similarly, computations of the conduction through the 3-mil diameter sample thermocouple wires indicated this loss to be small, relative to the loss through the heater leads; therefore no correction was made for the thermocouple wire losses. It will be shown later, in the discussion of results, that the power loss by conduction through the heater leads amounted to approximately 50% of the total applied heater power at low test temperatures. As a result, the uncertainty in the P_L term was the major source of uncertainty in the low temperature emittance determinations. At the high test temperatures, the relative power loss by conduction was considerably smaller, and the uncertainty in the emittance values was correspondingly lower.

The apparatus consists of three separate test chambers similar to the one shown in Figure 62, which are immersed in a common reservoir of liquid nitrogen and share a common vacuum system. The liquid nitrogen reservoir is supported inside a large evacuated cannister with a removable top plate. The vacuum system consists of a 4-in. oil diffusion pump, located beneath the apparatus, and a mechanical fore pump. The chamber pressure is indicated by a standard ionization gauge. A normal operating pressure of 10^{-8} Torr is maintained by this system, although pressure rises to 5×10^{-7} sometimes occurred at the highest test temperatures due to outgassing from the samples.

The individual test chambers are constructed of stainless steel and their inner walls are coated with a flat black paint to minimize interflections between the walls and the sample. The entire chamber is immersed in liquid nitrogen. The level of LN_2 is maintained by an automatic level sensor.

Electrical power to the sample heater is supplied by a dc power supply. Rheostats are wired in series with the sample heater and the current shunt to provide suitable control for obtaining the desired sample temperature. Voltage readings across the current shunt and the various thermocouples are made with a Leeds and Northrop type K3 potentiometer, accurate to four significant figures. The voltage drop across the sample heater is also read with the K-3 potentiometer, but at the higher temperature it is necessary to use a precision voltage divider to keep within the potentiometer voltage limitation.

The total hemispherical emittance sample consists of a hollow cylinder, 2.54 cm high by 2.54 cm in diameter with closed ends, and a wall thickness of 0.16 cm. To support the thin film materials and to maintain a uniform sample temperature, each film was bonded to the outside surface of a substrate cylinder machined from a 99.99% pure aluminum rod. Previous studies of this sample design have indicated that the overall temperature of the aluminum cylinder is uniform to within ±1°K of the average temperature between 250° and 600°K. As shown in Figure 62, the heater assembly hangs beneath the sample cap, which has two 0.16-cm-diameter holes for passage of the power leads. The power leads are 15-mil-diameter molybdenum wires and are insulated from the cylinder by small ceramic insulators which fit snugly into the holes. The heater consists of a length of a standard 500-W tungsten lamp filament which is mechanically crimped to the ends of the power loads. The cylinder body and bottom which encloses the heater also hangs from the cap assembly by means of pins through two pairs of matching holes drilled through opposite sides of the cylinder walls and through a circular lip on the underside of the cap.

For cementing the sample films to the aluminum substrate cylinders, a high-temperature strain gauge adhesive was selected (type BR-600, manufactured by W. T. Beam, Inc.). Preliminary tests indicated that a strong bond between polyimide film and aluminum was maintained at temperatures up to 650°K, although subsequent emittance tests indicated that small gas bubbles usually formed at about 600°K. Careful preparation of the surfaces was required to obtain suitable adhesion. The preparation and cementing procedure followed was as follows:

(1) Clean both the aluminum and the polyimide film surfaces with alcohol.

(2) Lightly roughen both surfaces with No. 600 emery paper dipped in alcohol.

(3) Reclean with alcohol.

(4) Treat aluminum surface with W. T. Beam, Inc., Metal Conditioner and Neutralizer.

(5) Apply thin coat of adhesive to the aluminum and polyimide film surfaces, and allow to dry for 2 min.

(6) Press polyimide film to aluminum and hold under pressure for 30 min.

(7) Cure for 1 hr in oven at 390°K. With this procedure, the films were tightly bonded to the substrate with smooth surface and no evidence of bubbles or blisters.

The maximum uncertainty in the total hemispherical emittance data for the coated films is strongly dependent upon sample temperature. This is due to the uncertainty in power loss correction and its magnitude in comparison to the sample power term. At 250°K this maximum uncertainty is 50%, whereas, at 500°K it decreases to 10%.

Appendix C

INFRARED TRANSMITTANCE APPARATUS

The experimental apparatus is shown schematically in Figure 63. Energy from the heated cavity source is chopped and passed through the specimen. For spectral measurements, the transmitted energy is collected by a front surfaced spherical mirror and focused onto the entrance slit of the monochromator. Total transmission measurements are made by collecting energy over 20% of the forward hemisphere with a front surface mirror which focused this energy onto a vacuum thermocouple detector having a cesium iodide window. Using this collection system, transmittance measurements at one source temperature were carried out as a function of angle from the normal by rotating the specimen source unit about the face of the specimen nearest to the collecting optics. The total transmission data for other source temperatures were then corrected on the basis of this one measurement of angular distribution of energy.

A diffusing screen was initially used between the source and specimen. This diffuser attenuated the energy and resulted in poor signal-to-noise ratios for thicker specimens. Several measurements were made with and without the diffuser using the highest source temperature. These data showed no measurable difference in angular distribution of energy. No further measurements were made using the diffuser plate.

Absorption and scattering coefficients are calculated using the method described by Folweiler (ref. 14). The material constants are determined from:

$$\cosh \sigma_o = \frac{\tau_2 \left[\tau_1 (1 + \rho_i) + (1 - \rho_o) \right]}{2\tau_1 (1 - \rho_o)} \tag{C.1}$$

$$\tau = \frac{2\beta_o (1 - \rho_o)(1 - \rho_i)}{\left[\beta_o^2 (1 + \rho_i)^2 + (1 - \rho_1)^2 \right] \sinh \sigma_o D + 2\beta_o (1 - \rho_i)^2 \cosh \sigma_o D} \tag{C.2}$$

The term D is the sample thickness corresponding to τ_2 and is one-half of the thickness of τ_1. The reflection corrections ρ_i and ρ_o are for the energy reflected at the interfaces (thickness = 0 and thickness = D, respectively). The values of ρ_i and ρ_o were estimated as described in ref. 14 from the index of refraction of the particular material. Values of index of refraction were taken from the literature.

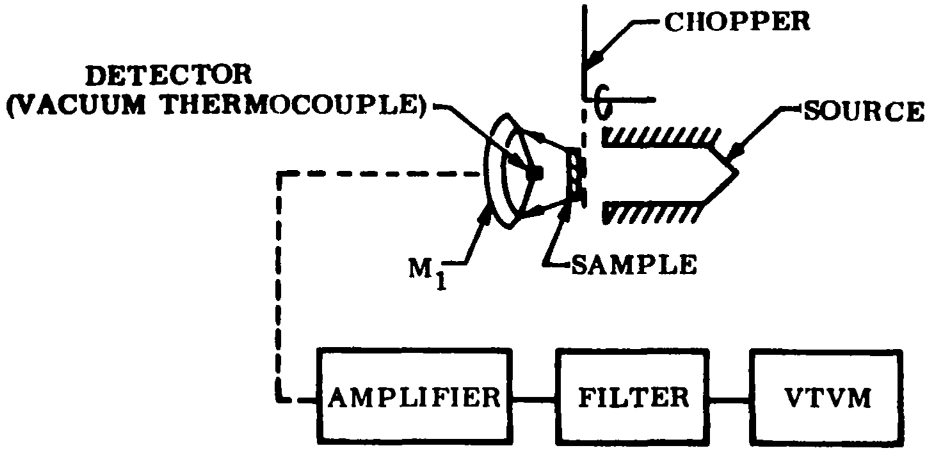

TOTAL TRANSMISSION MEASUREMENTS

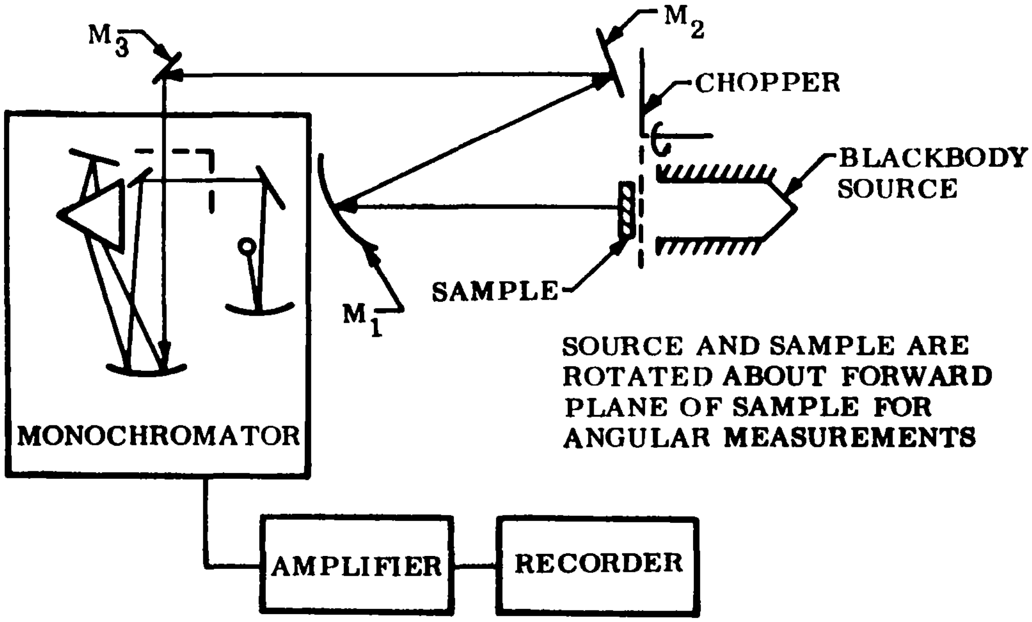

SOURCE AND SAMPLE ARE ROTATED ABOUT FORWARD PLANE OF SAMPLE FOR ANGULAR MEASUREMENTS

SPECTRAL AND ANGULAR DISTRIBUTION MEASUREMENTS

Figure 63 Apparatus for Measuring the Spectral, Angular, and Total Transmission of Spacer Materials

Calculations of absorption and scattering coefficients are performed using the following relations:

$$\sigma_o = [a(a + s)]^{1/2} \qquad (C.3)$$

$$\beta_o = \left(\frac{a}{a + s}\right)^{1/2} \qquad (C.4)$$

Appendix D

FLAT PLATE THERMAL CONDUCTIVITY APPARATUS

The flat plate calorimeter contains a 15.2 cm diameter main heater and a 15.5 cm i.d. by 41 cm o.d. guard heater constructed of 0.63 cm thick copper plates. The heaters are formed from stainless steel and are insulated from the copper surface plates with sheet mica. The edge guard is 47 cm in diameter by 5 cm high with water coils and an electric heater for temperature control. The copper ring has 2.54 cm wide, inward facing, circumferential copper fins. The fins are painted black to reduce energy reflections from the insulation edge. The calorimeter section consists of a 15.2 cm diameter measuring reservoir and a 41 cm o.d. guard reservoir. Copper plates 0.63 cm thick form the bottom of the reservoirs and contact the insulation. (See Figure 64.)

Temperatures of the heaters are measured with 5 mil chromel-alumel thermocouples peened into the copper surface. Control of heater temperatures are maintained using Leeds & Northrop CAT control and set point units with null detectors to sense control thermocouple output. Calorimeter fluid is 99% butane (B. P. = 273°K). The boiloff from the measuring section is continuously recorded using a Schuco recording flowmeter which is calibrated against a precision wet test meter over the range of 0.2 to 4.5 liters/hr. A wet test meter is also provided in the flow circuit for periodically checking the recording flowmeter calibration stability.

The latent heat of vaporization of the butane was determined by putting a known amount of electrical power into a resistor placed in the measuring section and measuring boiloff. Current and voltage drop across the resistor were measured using a precision shunt and voltage divider and a Leeds & Northrop Model K3 potentiometer. Total heat leak into the calorimeter measuring section has been verified by measuring the boiloff with the guard filled with butane and the sample replaced with a dished copper plate which is thermally grounded to the guard and spaced approximately 0.32 cm from the measuring section base. The heat sink results in a boiloff of 10^{-2} liters/hr which corresponds to a 2-1/2% correction for the minimum heat flux measured during this study.

Effective thermal conductivity is calculated from:

$$k_e = \frac{Q_c \times t}{A_c \times \overline{\Delta T}} \qquad \text{(D.1)}$$

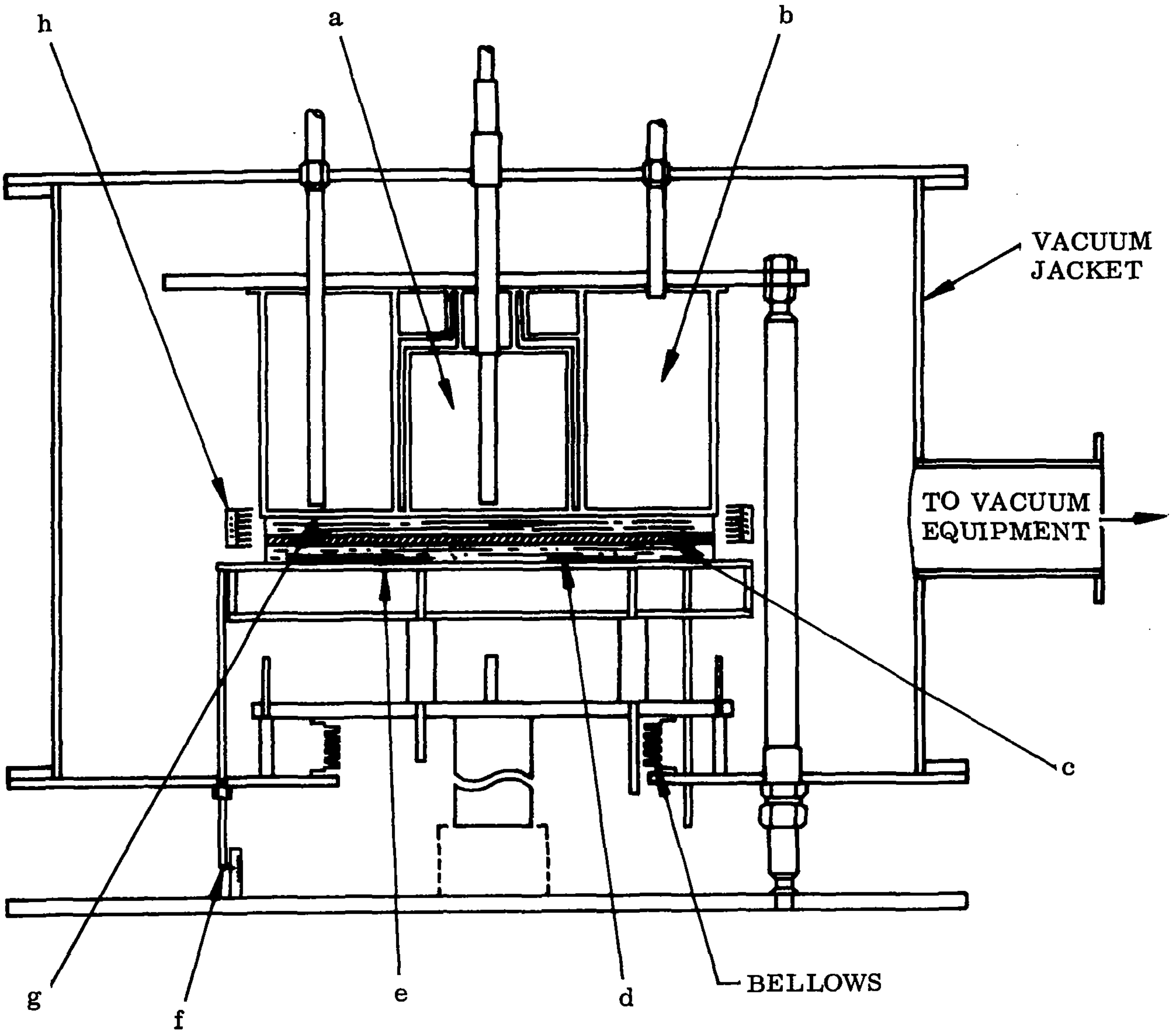

a	Calorimeter Reservoir
b	Guard Reservoir
c	Main and Guard Heaters
d	Heater Insulation
e	Water-Cooled Support Plate
f	Micrometer for Measuring Insulation Thickness
g	Test Specimen
h	Edge Boundary Heater Exchanger

Figure 64 Flat Plate Calorimeter Schematic Diagram

and

$$Q_c = 0.838 \overset{\circ}{V} \times \Delta H \times \rho_g \times (293 - T_g) \qquad (D.2)$$

The term ΔT is the difference between hot and cold boundary temperatures, i.e., surface plates. Cold boundary temperature is 273°K for all tests. For each test, one-dimensional heat transfer is checked at the highest hot boundary temperature by measuring the boiloff with constant boundary temperatures and the edge guard at 290°K and at the average temperature of the hot and cold boundaries. Vacuum is maintained with a 10 cm diameter oil diffusion pump backed with a 13.5 cfm mechanical pump.

The maximum uncertainty in the experimental values of effective thermal conductivity is calculated to be 22%. The largest single source of error is the influence of mismatch in guarding and lateral conduction effects. For the spacer materials and multilayer insulation this is estimated to be a maximum 10% for all materials tested.

The other significant source of error are as follows:

(1) Thickness measurement, 4% maximum uncertainty

(2) Boiloff flow measurement, 3% maximum uncertainty

(3) Gas density, 2% maximum uncertainty

(4) Temperature difference across boundaries, 2% maximum uncertainty

(5) Latent heat of vaporization of the calorimetric fluid, 1% maximum uncertainty (experimentally determined value of ΔH 387 joules/g as compared with 385 joule/g from the literature)

Appendix E

MULTIDIMENSIONAL TEST APPARATUS

A three-chamber calorimetric type of apparatus was fabricated for the multidimensional heat-transfer tests. It consisted of a central cylindrical measuring vessel with guard vessels at each end (Figure 65). The dimensions of the measuring and guard sections are 30.5 cm diameter by 30.5 cm long. Copper, OFHC, was used for the construction of each section. The measuring section is supported by three stainless steel wires arranged between a collar on the main support tube and a fiberglas phenolic ring on which the lower edge of the chamber rests. Each guard section is supported by a thin walled stainless-steel tube which is secured to the main support tube. A 0.15-cm spacing is maintained between the measuring sections and guards. All interior surfaces are insulated with 30 layers of aluminized Mylar-Dexiglas multilayer insulation.

The model was suspended vertically by the main support tube in an 8- by 10-ft vacuum chamber. An exterior heater assembly composed of three independently controlled sections, 30.5 cm high by 33 cm i.d., was placed around the test model. These were supported independently of the model structure. The heater was fabricated of 0.15 cm thick copper to which were attached heater windings of stainless sheathed wire. Heater temperatures were controlled with three dc power supplies through automatic temperature controllers using a feedback circuit. A multilayer insulation composed of aluminum foil radiation shields and Refrasil spacers was placed around the exterior of the heater units to limit the heat load onto the vacuum chamber cold walls.

Test model and insulation instrumentation consisted of 3-mil-diameter copper-constantan thermocouples. Chromel-alumel thermocouples, 5-mil diameter, were used for heater control and temperature readout. All thermocouple voltages were read with a Leeds and Northrup Model 8686 potentiometer. Measuring section boiloff was measured in the same manner and with the same apparatus as that used for the flat plate calorimeter (Appendix D). Boiloff rates for the guard sections were monitored with a precision wet test gas flow meter. A pressure control system was incorporated into the flow circuits to permit adjustment and control of the guard and measuring section pressures. Guard section pressure was maintained at 770 ± 2 mm Hg and measuring section pressure at 765 ± 2 mm Hg.

Liquid nitrogen was used for the calorimetric fluid rather than butane due to the safety requirements for the handling of large quantities of this hazardous fluid in the laboratory. As the intent of this phase of the study was to verify the analytical model, the choice of a lower temperature boundary condition was not critical. Effective thermal conductivity measurements were made on the test system using the model to provide the one-dimensional heat-transfer value to which the multidimensional data are to be compared.

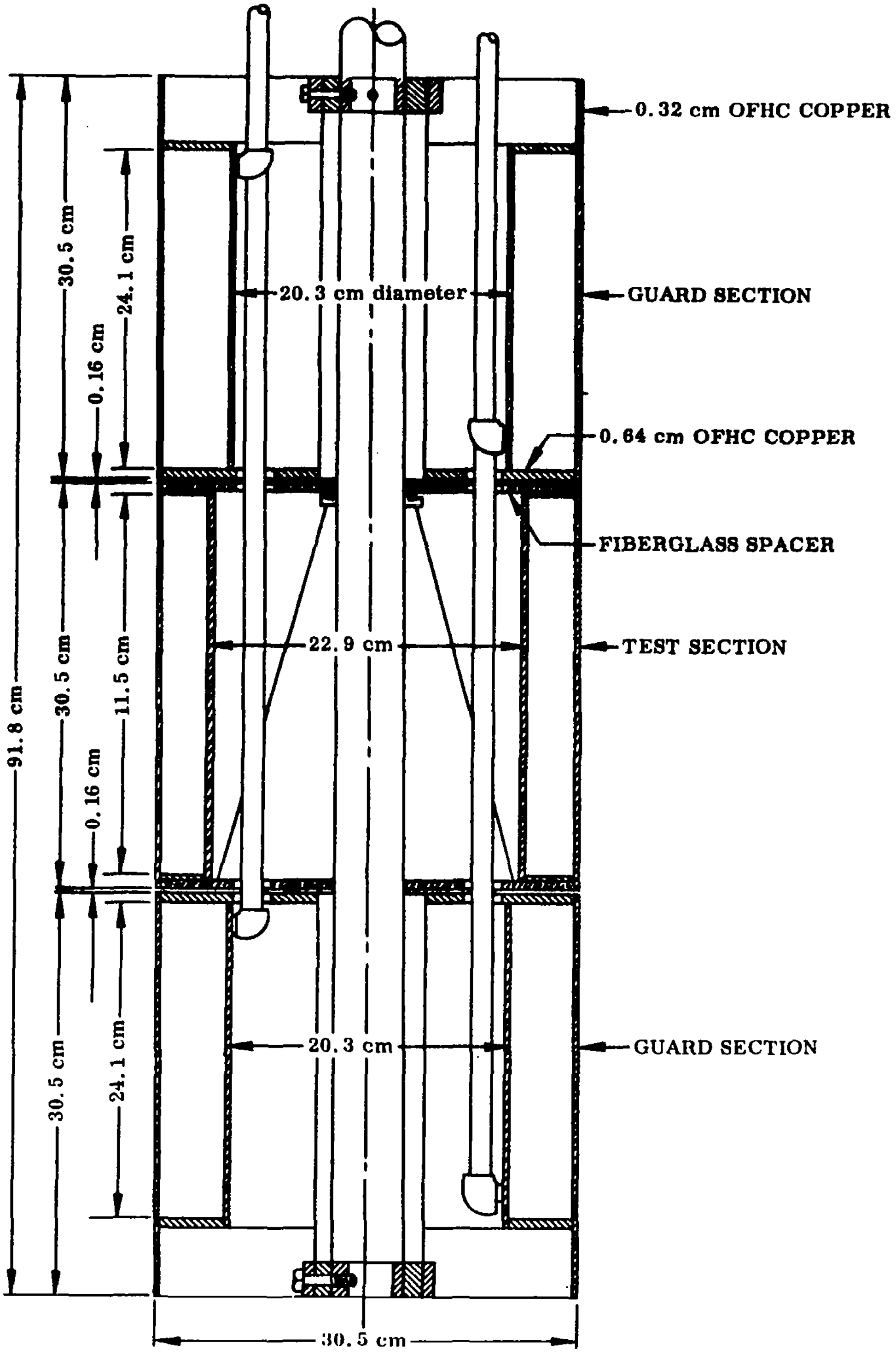

Figure 65 Insulation Test Calorimeter

After installation of the insulated model, the vacuum chamber pressure was reduced to 5×10^{-7} Torr. The measuring and guards sections were filled with LN_2 and heaters adjusted for the desired hot boundary temperatures. Boiloff and temperatures were monitored continually during the test period. After equilibrium conditions were achieved and all necessary data recorded, heater powers were increased for the next set of test conditions.

At the completion of the one-dimensional test, the model was removed from the chamber and the constant penetrations added at the center of the measuring section. This was fabricated from 0.254 mm thick copper in the form of a hollow cylinder 5.0 cm o.d. by 0.89 cm high. It was secured to the measuring section with a conductive epoxy cement. The cylinder i.d. was filled with Dexiglas paper at a density of 0.22 g/cm^3. The heat transfer for the areas was computed using the one-dimensional data obtained for this intermediary type of material. The test procedure was then repeated.

At the completion of these tests a strut-type penetration was added. This strut was formed as an angle 30.0 cm long with 0.89 cm and 0.45-cm legs of 0.38 mm thick copper. It was attached with a silver filled epoxy cement. The final configuration consisted of exposing the edges of the insulation, at each end of the measuring section, to a LN_2 surface. This was accomplished by cutting a 1 cm high segment from the blanket at each end of the measuring section. A LN_2 cooled fin was spaced approximately 0.3 cm from the edges.

NASA-Langley, 1967 —— 33 CR-907